Journal of New Technology and Materials
JNTM
Vol. 01, N°00 (2011)8-23

OEB Univ. Publish. Co.

Nanopowders prepared by Solar Physical Vapor Deposition (SPVD)

Claude J. A. Monty
CNRS, PROMES laboratory, Odeillo, Font-Romeu, 66120 France
claude.monty@promes.cnrs.fr
Received: 23 May 2011, accepted as plenary talk

Abstract
The Solar Physical Vapor Deposition (SPVD) is an original process to prepare nanopowders. This method has been developed in Odeillo-Font Romeu in France using solar reactors working under concentrated sunlight in 2kW solar furnaces. Various oxides, pure or containing other elements in addition, have been obtained. This paper focus on ZnO and TiO_2. based oxides It is shown that the X-Rays Diffraction analysis allows a fine nanostructural characterisation of the nanophases present in these nanopowders. In many cases, HRTEM or SEM and XPS complement the XRD analysis. The properties such as Electrical, magnetic properties, photoreactivity, luminescence ... known on microstructured materials of the same composition are revisited on these nanopowders or on nanomaterials prepared from them and led in many cases to original behaviours.
Keywords : SPVD, nanopowders, Al doped ZnO, Co doped ZnO, Bi_2O_3, TiO_2, XRD, HRTEM, chemical reactivity, magnetic properties, electrical conductivity.

1. Introduction

An original process to prepare nanopowders : the Solar Physical Vapor Deposition (SPVD) is presented[1]. Pure ZnO, $Zn_{1-x}Al_xO$, $Zn_{1-x}Co_xO$, $Zn_{1-x}Bi_xO$ and metallic Zn nanophases as well as pure TiO_2 and Fe, Co or Mn-doped TiO_2 have been prepared by this method which we have initially used to prepare simple nanophases of good quality : $Zr_{1-x}Y_xO_2$, γ-Fe_2O_3, In_2O_3, SnO_2... [2-5].

In some experiments, nanopowders appeared to be a mixtures of nanophases, it was the case of $(Zn_{1-x}Bi_xO)$ and $(Bi_{1-y}Zn_y)_2O_3$.obtained both in unequal quantities, but also the case of metallic Zn obtained beside strongly reduced ZnO_{1-x}. and of TiO_2 nanopowders which are generally a mixture of rutile and anatase. Composite nanoparticles such as MgO coated Fe nanoparticles can be also prepared by SPVD.

To characterize the nanostructure and the composition of the nanopowders the main method used was X Ray Diffraction (XRD) analysis. The nanostructure and detailed information on the nanophases present in the nanopowders are studied too by High Resolution Transmission Electron Microscopy (HRTEM) or by Scanning Electron Microscopy (SEM). Energy Dispersive X-ray analysis (EDX) and X-ray Photoelectron Spectroscopy (XPS) bring in some cases complementary information on the chemical state of the nanopowders. Studies have been performed to know more about their chemical reactivity, their magnetic or/and their luminescence properties. In the case of nanopowders prepared by SPVD from targets made by sintering ZnO and Bi_2O_3, nanostructured ceramics could be obtained and their electrical properties studied

The properties found are clearly related to the composition and the nanostructure of the nanopowders prepared by the SPVD process. Most of studies were performed in collaboration and important papers are cited in references but in this paper, some striking results obtained on ZnO and TiO_2 based nanomaterials have been revisited.

2. Nanopowders and massive nanomaterials

Nanopowders are formed of grains (unorganised aggregates, nanocrystals or polycrystals) which have nanometric dimensions ; they belong to the general class of "nanomaterials". It is known that nanomaterials properties are strongly influenced by the interfaces present (surfaces, grain boundaries...)[3, 2].

Dimensional and microstructural criterions can be used to classify a material among the nanomaterials ones[2, 6]. These criterions have the merit to recall that well before the appearance of nanomaterials, the solid state physicists were interested in aggregates of some atoms and the effects of their size on the electronic and crystallographic structures [7]. In the same way, the chemists knew for a long time that the chemical reactivity of small particles is much higher than that of ordinary powders this property is used in catalysis.

It is not surprising when a property is studied as a function of the grain size (or the thickness of a layer deposited on a substrate), to observe an "abnormal" behavior for grains sizes or a thickness smaller than around 100 nm. The "critical size" depends on the sensitivity of the properties studied on the interfaces and their thermodynamic state. For the same material it varies with the property and with the thermo-mechanical history of the material.

Technologies are in progress from about 20 years now to prepare films or coatings and massive nanomaterials directly or from the nanopowders obtained by various methods. In the following an original process to prepare nanopowders is described: the Solar Physical Vapor Deposition (SPVD) and some typical results obtained on selected oxides are gathered and compared [4-5, 8-10, 6, 11-12].

3. The Physical Vapor Deposition process in a Solar reactor (SPVD)

3-a The solar reactor « Heliotron »

A 1MW solar furnace was built in Odeillo/Font Romeu around 1970. In the same building and beside, ten 2kW solar furnaces and a 10 kW more easy to handle can be used for laboratory experiments at a smaller scale. They are constituted by mobile plane mirrors ("heliostats") tracking the sun and reflecting the radiation on a parabolic concentrator. At the focus where the concentration can be as high as 18000 on a surface of around 10 mm^2, are placed more or less sophisticated reactors or experimental set ups.

For the SPVD experiments, the reactors are constituted by glass balloons (see figure 1). Inside, a target, made with the material to be melted and vaporized or sublimated (depending on its nature), is placed on a cooled support at the focus of the concentrator. The vapor pressure around the target depends on the material and on the atmosphere inside the balloon, it is more or less large. In the last case, a smoke is generally visible and is depositing by condensation on a cold finger (water cooled copper tube)[4]. In a similar reactor, the smoke is collected on a metallic or a nanoporous ceramic filter through which the gas atmosphere is flowing.

The "heliotron", associates the two processes (see figure 1) : collection by trapping on a cold finger and pumping through a filter, which decreases the phenomena of condensation on the walls of the balloon and increases the effectiveness of the collection. The production rate of the nanopowders depends on the vapor pressure of the material. In the best cases (for example pure or doped zinc oxide), it can reach several hundred milligrams per hour.

When the vapor pressure on the top of the melted material is low, which is the case of alumina or doped zirconia for examples, it is less than 1 mg/hour in a sunny period (flux higher than $1kW/m^2$). It is one of the reasons why in that case, when large quantities are needed, a different process has been developed, associating melting in a solar furnace, quenching and ball milling[6].

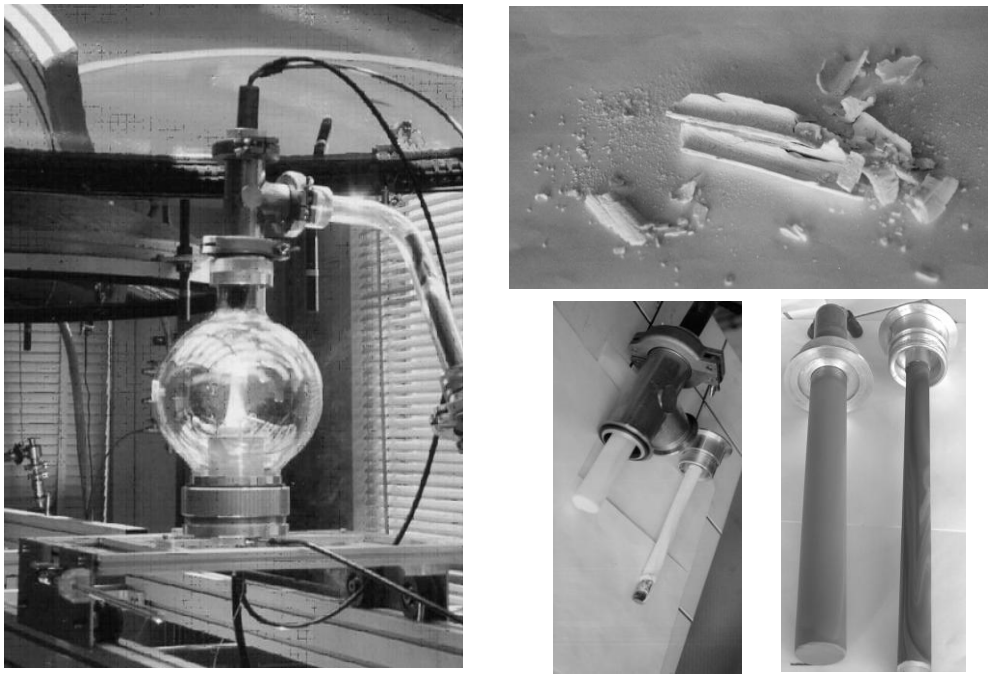

Figure 1 – SPVD process in the Heliotron solar reactor. Nanopowders are collected simultaneously on a ceramic (or metallic) filter and on a water cooled copper finger. In the case of ZnO, the nanophases are white fibers. Under Ar flow the collected grey nanopowders are a mixture of Zn and highly reduced ZnO.

3-b Nanophases prepared by SPVD or SCVD

Using "heliotron" type solar reactors in 2kW furnaces SPVD appeared to be an excellent process to prepare nanophases. Depending on the composition of the targets, the oxide nanopowders obtained were formed by one type of nanophases : ZrO_{2-x}, SnO_{2-x}, MgO, In_2O_3, CeO_2, gadolinium doped ceria $Ce_{1-x}Gd_xO_{2-\delta}$, yttrium doped zirconia $Zr_{1-x}Y_xO_{2-\delta}$, TiO_2 (Anatase or Rutile) and pure or doped zinc oxide nanophases : ZnO, $Zn_{1-x}In_xO$, $Zn_{1-x}Sb_xO$, $Zn_{1-x}Al_xO$, $Zn_{1-x}Co_xO$, $Zn_{1-x}Bi_xO$, β-$Bi_2O_{3-\delta}$. [4-5, 8-10, 6, 12]. Starting from targets made by sintering ZnO and Bi_2O_3, mixtures of $(Zn_{1-x}Bi_xO)$ and $(Bi_{1-y}Zn_y)_2O_{3-z}$. nanophases were prepared[11]. More recently composite nanoparticles such as MgO coated Fe could also be prepared, playing on the target composition and the oxydo-reduction properties of the atmosphere[13]. In reducing atmospheres (Ar or N_2) ZnO leads at high temperature to metallic Zn particles mixed with a small proportion of ZnO nanophases[12]. SPVD of AlN in hydrogenated argon lead to metallic Al nanophases (in such a case Solar Chemical Vapor Deposition or SCVD is a more adequate terminology than

SPVD. Nanophases of Si and SiO_x were produced starting from silicon targets in a reactor whose vacuum was improved[14]. Large quantities of fullerenes and nanotubes were prepared by the same method in the 1 MW solar furnace of Odeillo by using a special 50 kW reactor with a graphite chamber[15].

In many cases, chemical reactions occur during the process and Solar Chemical Vapor Deposition, or SCVD, is a more adequate terminology than SPVD.

In the following some examples taken in the previous ones are considered.

4. Characterization of the nanopowders by X-Ray Diffraction

The first method used to characterize the powders after synthesis is the X-ray diffraction analysis (XRD). In the case of nanopowders, the diffraction peaks are widened compared to diffraction peaks obtained on micrometric powders. The Scherrer relation[16-17] can be used to determine the average size of the "fields of coherence" of diffracting domains of the analyzed powder and to compare it to the average grain size determined by other methods (HRTEM for example). Observations by scanning electron microscopy (SEM) or by transmission electron microscopy (TEM and HRTEM) are useful methods to achieve the nanostructural studies made by XRD. XPS analysis gives access to the nanochemistry of the nanophases, constituting the nanopowders.

4-a X-rays diffraction diagram

The X-ray diffraction peaks obtained from a crystallized powder are characterized by diffraction angles θ_{hkl} and I_{hkl} intensities depending on the lattice cell and on the λ wavelength radiation, used. The hkl Miller indexes correspond to the diffracting crystallographic planes (d_{hkl} is the distance between them). These three parameters are connected through the Bragg relation :

$$2d_{hkl} \sin \theta_{hkl} = n\lambda \qquad (1)$$

The position of the diffraction peaks gives access to the distances d_{hkl} between crystallographic planes, the structure and the lattice parameters.

If a monochromator is used, λ is perfectly defined. In order not to loose intensity, two close wavelengths are used simultaneously; it is the case with a copper anti-cathode whose the emission spectra contains the two close wavelengths $\lambda_{K\alpha1}$= 1.540562 Å and $\lambda_{K\alpha2}$= 1.54390 Å.

A fit of each diffraction peak by two Lorentz functions, corresponding to $\lambda_{K\alpha1}$ and $\lambda_{K\alpha2}$ wavelength, can be carried out by using for example the ORIGIN software. These functions have the following form :

$$y = y_0 + \frac{2A}{\pi} \frac{w}{4(x-x_0)^2 + w^2} \qquad (2)$$

in which :

y_0 is the value of the continuous background taken at the origin ;

A is the total area under the curve after subtraction of the background ;

x_0 is the x-coordinate to the maximum of the y-coordinate ;

w is called the Full Width of the peak at Half Maximum y value (FWHM).

These functions fit to the profiles of diffraction peak and specially allow a very good evaluation of FWHM. The peak area (parameter A) obtained using these functions is however known with some error. To calculate "the integral width", $A/y(x_0)$, it is for example, more accurate to fit the peak profiles with pseudo-Voigt functions. The diffraction peak width has to be corrected by an "instrumental width" w_{st}. The shape and the intrinsic width w_{in} of the diffraction peaks are dependent on the dimensions of the coherence diffraction domains called the "grain size" and on their mechanical state (strains). In classical materials without stresses and well crystallised over a micron scale, the peak width w and the instrumental width w_{st} are equal (w_{in} is nul or very small), but in nanomaterials they differ significantly. Langford et al. (1986)[17] have proposed a method to separate both effects plotting $w_{in} \cos\theta$ as a function of $\sin\theta$ leads for the same crystallographic plane family to a line with a positive slope or to a constant line, depending on the fact there are strains or not in the material. This method provides too a good determination of the peak's position x_0, associated to a given wavelength, which can be used to determine accurate values of the lattice parameters.

The intensity of the diffraction peaks (maximum of y in the relation 2) is connected to the crystallographic structure by the "structure factor" which takes into account the arrangement of the atoms and the distribution of grain orientations (texture). If the peak width are different from the instrumental peak width, the texture effects can be determined considering the integrated intensities (parameter A of the fitting function).

4-b Determination of the grain size

From the fits obtained on the experimental peaks, it is possible to determine the "intrinsic width" w_{in} of the diffraction peaks and to compute an "average grain size" d_m, using the relation (3) proposed by Scherrer :

$$d_m = K\lambda / w_{in} \cos\theta \qquad (3)$$

where

- d_m is the average size of crystallites
- K is a constant which depends on the form of the crystallites and on the Miller indexes [16] showed that in main cases the value of K is close to 0.9) ;
- θ is the Bragg diffraction angle ;
- λ is the wavelength of the incidental radiation ;
- w_{in} is the intrinsic width of the diffraction peak (measured in radians) which can be determined from the relation : $w^2_{in} = w^2 - w^2_{st}$ (strictly valid for Gaussian peak profiles).
- w corresponds to FWHM (see earlier).
- w_{st} is the instrumental width, i.e. the value of w obtained on reference crystals.

The use of this formula imposes to know the "instrumental function". That has been done using pure ZnO or LaB_6 polycrystals as reference materials.

4-c Instrumental function

To determine the "instrumental function", it is necessary to perform XRD on a reference material with large grain sizes and without strains. A pure ZnO powder has been annealed in air at 1400°C during 48h in such a way to obtain a large grain size. The X-Ray Diffraction diagram obtained is shown in the figure 2.

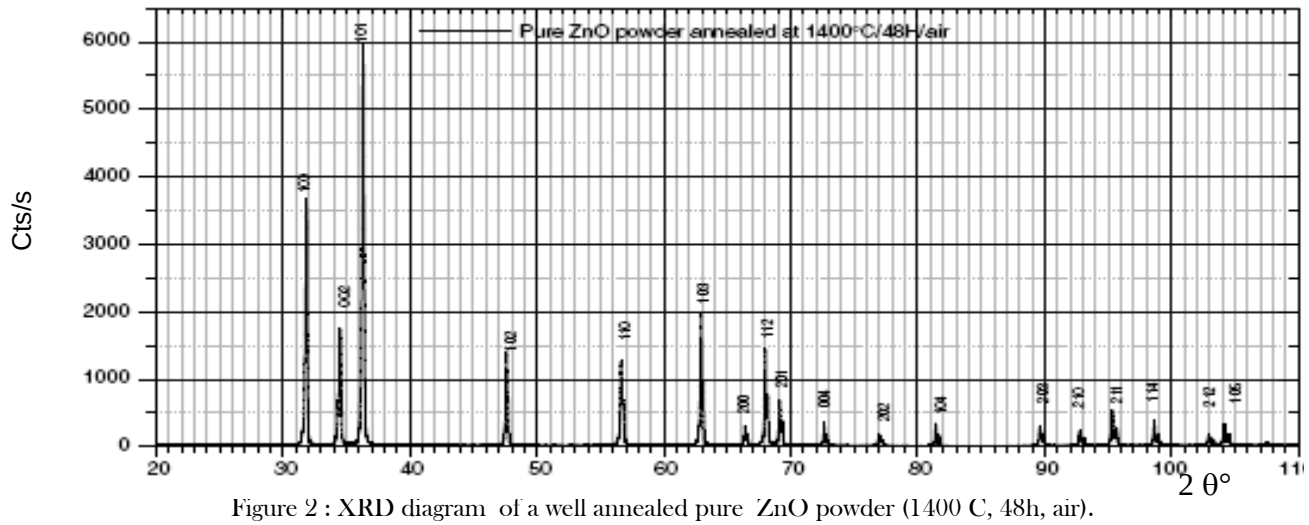

Figure 2 : XRD diagram of a well annealed pure ZnO powder (1400 C, 48h, air).

The intensities of the diffraction peaks of the diagram shown in figure 2 correspond to the XRD diagrams of the ICDD reference file (36-1451) and to the zincite hexagonal structure from the American Mineralogist Crystal Structure Database. Using these data of the atomic positions in the computer software CaRIne[18] leads to a quite similar diagram.

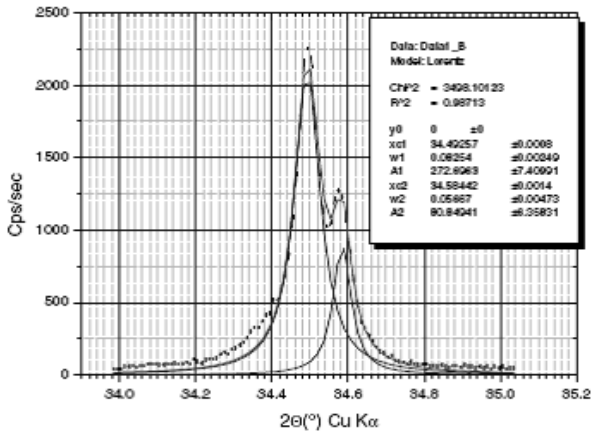

Figure 3 Decomposition in two Lorentz functions of the 002 peak of the XRD diagram seen in figure 2.

XRD spectra were analysed according to the criteria defined previously. Figure 3 shows an example of decomposition of the 002 peak in two Lorentz functions corresponding to the two components $\lambda_{K\alpha1}$ and $\lambda_{K\alpha2}$ of the wavelength $\lambda_{K\alpha}$ of copper. This procedure leads to define the "instrumental width" for each peak ; it has been applied to the whole diagram. The instrumental function can be defined as a fit to these experimental points ; the results obtained in this study are reported in the figure 4 beside similar results obtained using a LaB_6 polycrystal. Note the dispersion of the experimental points obtained on ZnO related to specific crystallographic directions, they are very close of those obtained by Langford et al. (1986)[17] : despite the fact that the instrumental function obtained correspond to the smallest FWHM values (obtained among several experiments), it is influenced by the microstructure. LaB_6 is then the best reference which can be used to characterize all the nanomaterials studied (as far as the XRD experimental set up is not modified). Nevertheless, the influence due to the difference between these two references is important only when the particles have large sizes i.e. higher than 100 nm.

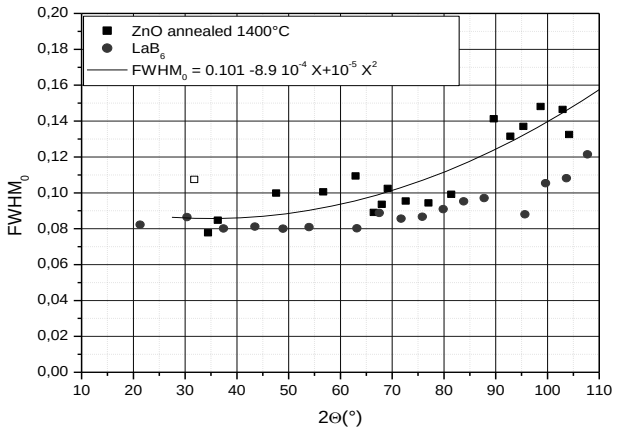

Figure 4 : Instrumental function determined using a LaB_6 polycrystal and compared to the values obtained from the diagram of figure 2.

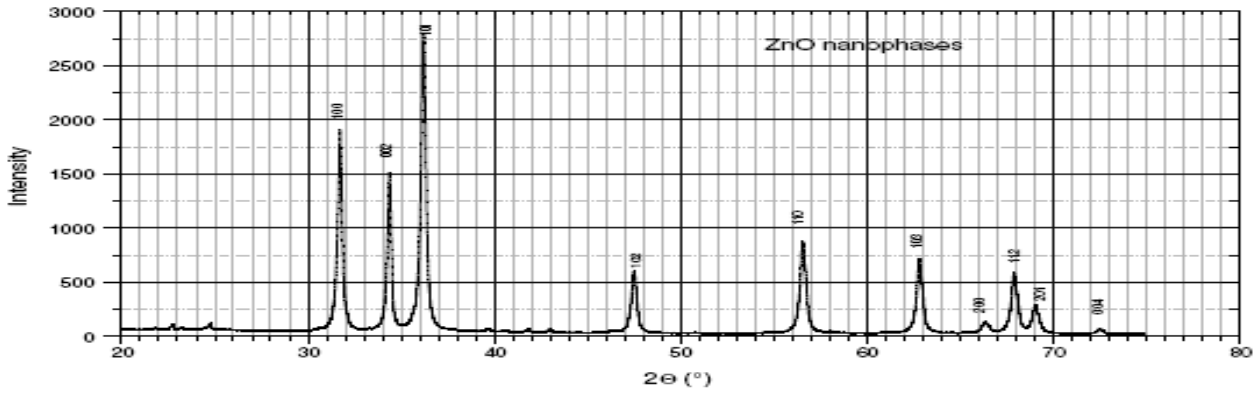

Figure 5 : XRD diagram of a ZnO nanopowder obtained by SPVD.

5. Characterisation and properties of ZnO based nanopowders prepared by SPVD

5-a SPVD nanopowders of pure ZnO

ZnO is a good example of oxide which can be prepared effectively in the form of nanophases by SPVD. The XRD diagram obtained on nanopowders (see figure 5) can be compared to the diagram obtained on annealed pure ZnO powder (fig 2).

Several observations can be made :

- The positions of the diffraction peaks of the nanopowders are, at first approximation, the same as those of a theoretical diagram computed taking an hexagonal cell with a = 3.24 Å and c = 5.20 Å.
- The diffraction peaks of the nanopowders are widened compared to those which are observed on a ZnO annealed powder, that is evident on the decomposition of 002 peak in figure 6 compared to the figure 3.

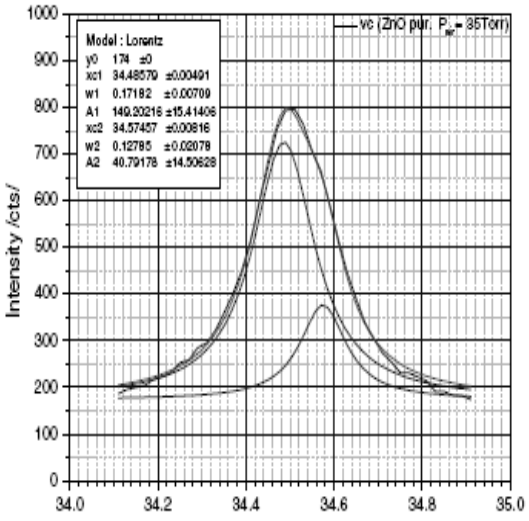

Figure 6 : Decomposition of the 002 peak of the XRD diagram of the figure 5.

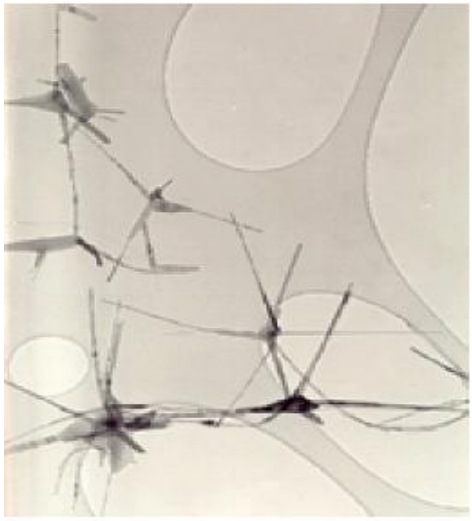

Figure 7 : TEM image of ZnO nanophases prepared by SPVD (x50000)

XRD changes indicate important size effects. The observation by TEM of SPVD powders obtained under 70-100 Torr of oxygen pressure, has shown elongated particles like rods, tetraedraly arranged 4 by 4 (see figure 7)[8].

When the morphology of the nanophases is anisotropic, it is possible by XRD to determine their average form from the "average sizes" of the particles along the principal crystallographic directions. It is however necessary to take into account that it is the average size of the coherence diffraction domains which are related to the size and morphology of the substructure. The determination of the size distributions and the morphology of the particles can be refined by observations in electron microscopy (HRTEM or SEM). This phenomenon appears too in the work performed by Langford et al. (1986)[17] and is generally observed in all the experimental XRD spectrum determined on ZnO.

5-b Grain size determination of pure ZnO nanopowders

Relation (3) has been used to calculate the coherence diffraction domain size d_m ("grain size") for the peaks obtained on ZnO SPVD nanopowders. The values obtained have been reported in figure 8 as a function of 2θ and of the origin of the starting powder: hydrothermal[19-20] or plasma synthesis[21]. The method applied to a broad field of the XRD diagrams permitted in the case of ZnO to highlight the shape anisotropy of the coherence diffraction domains. It can be seen indeed that the dimensions obtained depend on the crystallographic directions considered. The peaks corresponding to the crystallographic directions [00l] (reflecting planes parallel to the basic plane and perpendicular to the c axis) have a smaller width than that of the hk0 peaks (reflecting planes containing the c axis). The average shape of the coherence diffraction domains can thus be represented by an ellipsoid lengthened along the c axis. That is confirmed by HRTEM observations showing that under air pressures of 70-100 Torr, the nanophases are whiskers (see figure 7). Nevertheless when the starting powder has been prepared by a plasma process the [200] direction corresponds also to large sizes. That could be interpreted like due to a preferential lengthening in a direction perpendicular to the c axis for a part of the nanoparticles. However, the accuracy of these determinations to the large diffraction angles remains smaller than with the small angles (more raised intensities, less recovering between peaks...). The fact that [100] direction does not indicate the same phenomenon, do not permit to interpret these observations in spite of their systematic character.

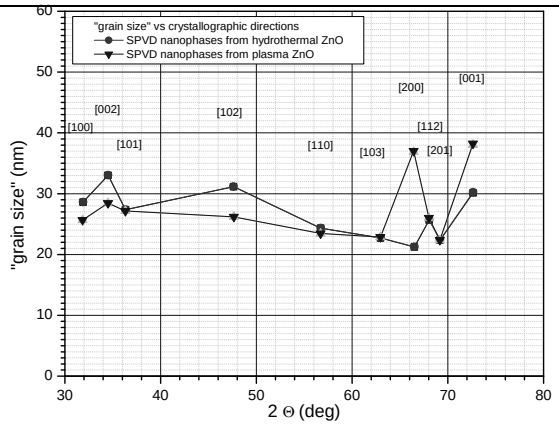

Figure 8-a : Coherency domain size ("grain size") as a function of crystallographic directions in ZnO nanopowders prepared by SPVD.

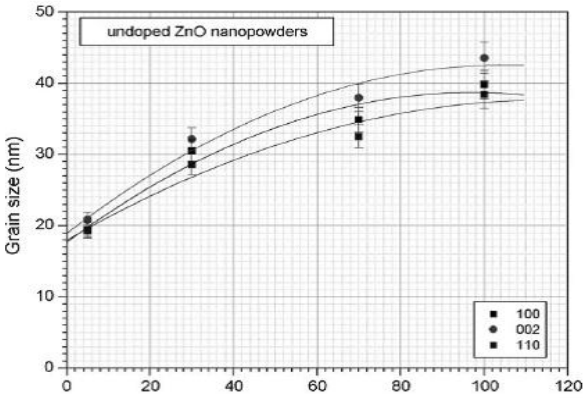

Figure 8-b : Influence of the air pressure on the grain size and shape anisotropy during the SPVD process.

A study of the influence of the air pressure inside the solar reactor on the grain size during the SPVD process has shown that increasing the pressure, increases the grain size along the c-axes and in perpendicular directions as well (see figure 8-b)[11].

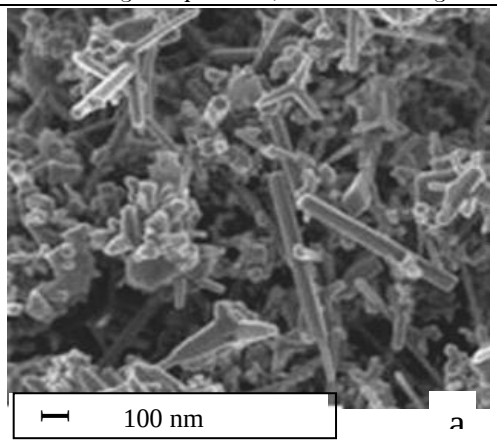

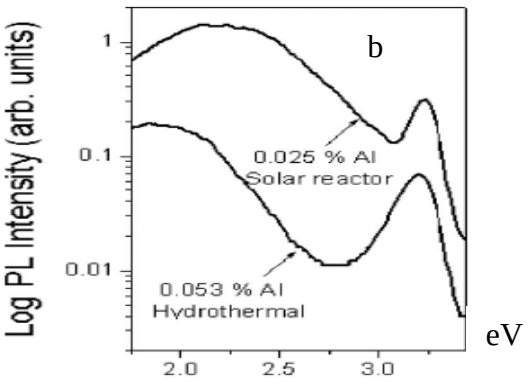

Figures 9-a -SEM image of a 0.16wt% Al doped ZnO nanopowder prepared by SPVD.
Figure 9-b –Photoluminescence of Al-doped nanopowders :
comparison of SPVD nanopowders with hydrothermal nanopowders.

5-c Al-doped ZnO nanopowders

Al doped ZnO nanopowders have been obtained by SPVD starting from powders prepared by an hydrothermal method[20] and containing 0.045wt% Al. The final content after vaporisation-condensation was 0.016wt%[23]. The image in figure 9-a shows an aspect of these nanopowders.

The nanopowders exhibit a photoluminescence in the blue range. It is clear that SPVD nanopowders have an intensity which is about an order of magnitude higher than the hydrothermal nanopowders from which they are issued, but they have lost a part of the doping element during the SPVD process.

SPVD nanopowders of Al doped ZnO obtained by a plasma process have been prepared[22]. The plasma method leads to introduce larger quantities of aluminium than the others methods. The nanopowders have been characterized by XRD in a similar way as it has been done for pure ZnO nanophases,. Figure 10-a shows the variations of average dimensions of the coherence diffraction domains determined as a function of the Al content of the powders.

These "grain sizes" vary with the direction in a similar way to those of the nanopowders of pure ZnO discussed previously. It was found nevertheless that the grain size increases when the Al content increases and, in the same time, the anisotropic shapes of the coherence diffraction domains are changing from a mixture of rods elongated along [001] and platelets perpendicular to [001], to mainly long rods.

The luminescence properties of Al doped ZnO nanopowders obtained by SPVD from targets prepared by a plasma process has been studied by Grigorjeva et al.[22]. An important result is a pure and intense blue light emission at 3.27 eV clearly related to the Al content of the doped ZnO nanopowders and to the SPVD process[22] (see figure 10-b).

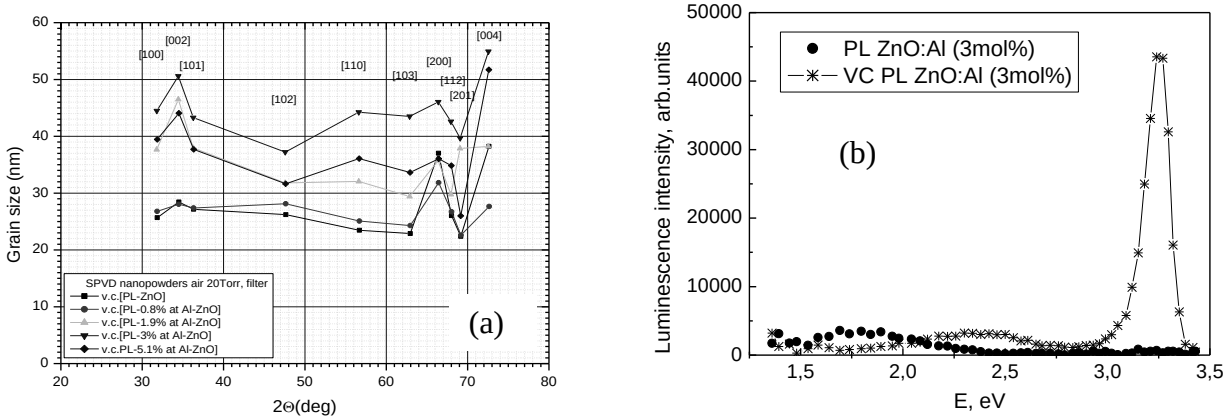

Figure 10-a: "grain size" as a function of the crystallographic direction for nanophases prepared by SPVD from Al doped ZnO obtained by a plasma process.

Figure 10-b : Blue emission of SPVD nanophases obtained by SPVD (noted VC) from Al doped ZnO (3%mol) targets prepared by a plasma process[22].

5-d Co-doped ZnO nanopowders

Co doped ZnO nanopowders were prepared by SPVD in order to study their magnetic properties. The anisotropic shape of the coherence diffraction domain observed in the case of pure ZnO is also highlighted in ZnO doped Co. The average "grain size" is around 20 nm and does not depends on the Co content. This has been also observed by transmission electron microscopy (see figures 11).The morphology of the nanopowders of Co doped ZnO is sensitive to the pressure maintained in the reactor during the SPVD process.

The magnetic properties of Co doped ZnO SPVD nanopowders were studied. For 5% at. Co doped ZnO prepared by SPVD under low air pressure, a ferromagnetic state appears with an hysteresis cycle and low coercitive field (approximately 100 Oe) at 5K and a saturation magnetisation. However these powders are superparamagnetic at the ambient temperature when they are prepared under air pressures of about 70-100 Torr [24].

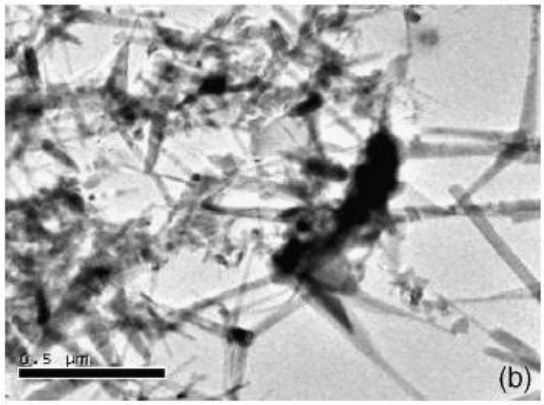

Figure 11 : Transmission Electron Microscopy of Co doped ZnO nanophases prepared by SPVD under 70-100 Torr air pressure.

5-e (ZnO)$_x$(Bi$_2$O$_3$)$_y$ nanopowders

Targets made of mixtures of ZnO and Bi_2O_3 with three compositions (5, 12 and 20 wt. %Bi_2O_3) were prepared and annealed under air at 700°C during 8 h to 17 h. The XRD analysis of these targets shows that two phases are present : $Zn_{1-x}Bi_xO$ and $Bi_{38}ZnO_{58+\delta}$ (cubic, δ=0 ref. JCPDS 41-0253, δ=2 ref. JCPDS 41-0253). The nanopowders obtained by SPVD from these targets under 30-40 Torr air pressure were characterised by XRD. The analysis indicates again that two phases are present (see figure 12) : one was identified as $Zn_{1-x}Bi_xO$, yet seen in the targets, but the peaks corresponding to the other phase are related to $(Bi_{1-y}Zn_y)_2O_{3-z}$ close to β-Bi_2O_3 (tetragonal, ref. JCPDS 78-1793). The $Bi_{38}ZnO_{58+\delta}$ phase seen in the targets has vanished during the SPVD process.

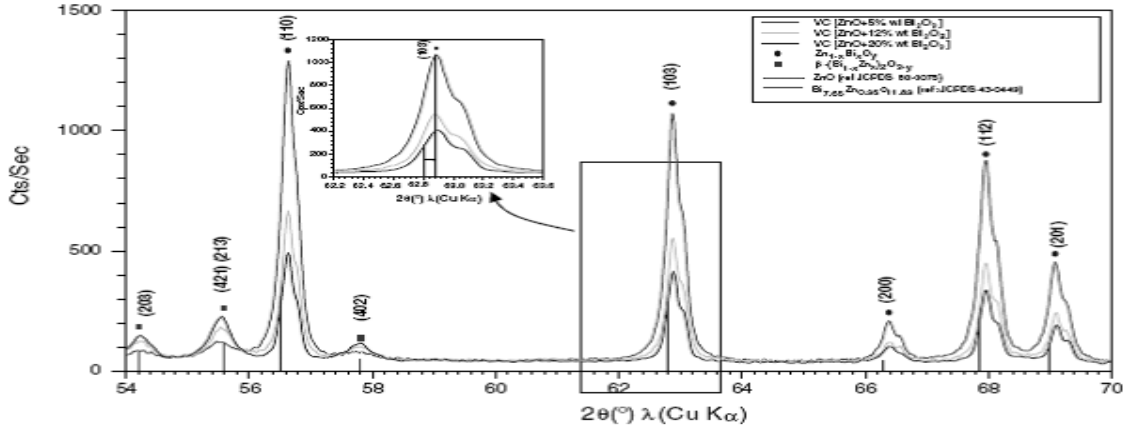

Figure 12 : XRD diagrams of nanopowders prepared by SPVD from targets made of mixtures of ZnO and Bi_2O_3

HRTEM studies have shown that for 5 wt% Bi_2O_3, the aspect is similar to pure ZnO nanopowders prepared in same conditions with a prevalence of nanowhiskers. Increasing the bismuth content, the morphology changes from whiskers to more compact shapes. Precipitates are visible, they are more and more numerous and less and less lengthened when the Bi content increases. The $(Bi_{1-y}Zn_y)_2O_{3-z}$ phase has a tetragonal character which explains the polygonal shapes of the observed precipitates (see figure 13).

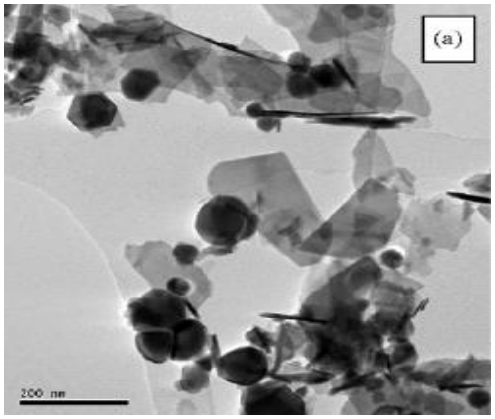

Figure 13 : TEM images from nanopowders prepared by SPVD using ZnO+20%wt Bi_2O_3 targets

Average nanophase sizes have been deduced from the diffraction peaks corresponding to $Zn_{1-x}Bi_xO$ in the XRD diagram of figure 12, the results are reported in figure 14. Increasing the Bi content of the targets, the $Zn_{1-x}Bi_xO$ nanophases are characterized by a decreasing "grain size", the smallest grain sizes (around 30nm) being obtained on nanopowders prepared by SPVD using ZnO+20%wt Bi_2O_3 targets. As the black (thick) precipitates in figure 12 have been identified as the Bi rich compound $(Bi_{1-y}Zn_y)_2O_{3-z}$, the $Zn_{1-x}Bi_xO$ solid solution correspond to the zinc rich transparent platelets. The decrease of their size could be due to their substructure or to twisted or/and tilted parts of the nanocrystals. Looking at the XRD peaks intensities, It is clear that the dominant phase in these nanopowders is $(Bi_{1-y}Zn_y)_2O_{3-z}$, which can be considered as Zn doped β-Bi_2O_3 and noted β-$(Bi_{1-y}Zn_y)_2O_{3-z}$.

From these nanopowders it is possible to prepare films or coatings or massive nanomaterials. The annealing treatment performed to sinter the nanopowders (820°C, 2 h in air) induces a new phase change : in the nanomaterial obtained two phases are present : $Zn_{1-y}Bi_yO$ and $(Bi_{1-x}Zn_x)_2O_{3-y}$ close to α-Bi_2O_3 (monoclinic, ref. JCPDS 71-2274) and accordingly noted α-$(Bi_{1-x}Zn_x)_2O_{3-y}$.

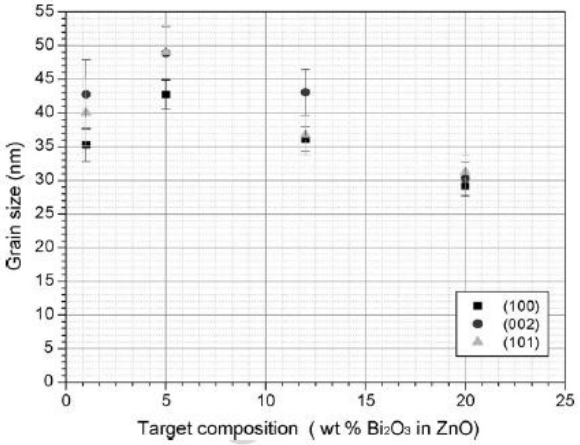

Figure 14 : $Zn_{1-x}Bi_xO$ nanophases grain size as a function of the Bi content of the SPVD target

The electrical conductivity of these nanocomposites has been measured by impedance spectroscopy, the results obtained at temperatures in between 110°C to 300°C are shown in the figure 15 and compared to the conductivity of α, β and δ-Bi_2O_3 [25], to the conductivity of the $Bi_{38}ZnO_{58+\delta}$ cubic phase (which has been synthesised separately) and to the conductivity of gadolinium doped ceria as a reference : the massive nanomaterials prepared from $(ZnO)_{95.2}(Bi_2O_3)_{4.8}$ nanopowders (obtained from ZnO+15wt%Bi_2O_3 mixtures) are the best ionics conductors in the considered temperature range, the $(ZnO)_{98.7}(Bi_2O_3)_{1.3}$ nanopowders (obtained from ZnO+5wt.%Bi_2O_3 mixtures) lead to nanomaterials less conductive. Bi rich phases $(Bi_{1-x}Zn_x)_2O_{3-\delta}$. are probably responsible for these results.

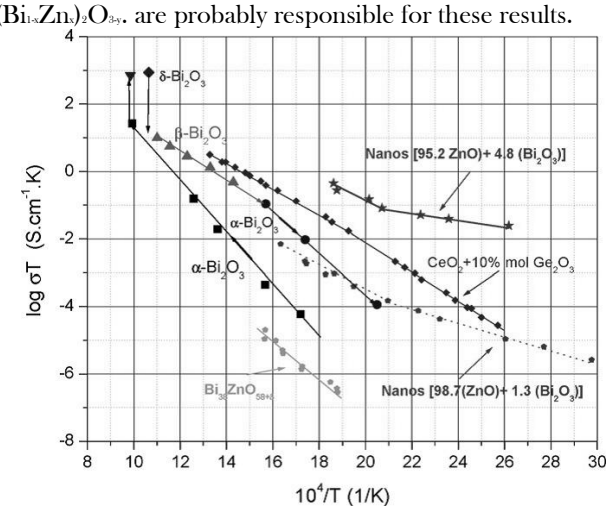

Figure 15 : ionic conductivity of several compounds compared in an Arrhenius diagram.

5-f Zn and ZnO_{1-x} nanophases[6, 12]

A preparation by SPVD of nanopowders from pure ZnO was carried out under argon flow at pressures from 2 Torr to 20 Torr (flows from 2 to 3 liters/min) in the solar reactor "heliotron". XRD diagram of the nanopowders show that the collected nanopowders were constituted by a mixture of metallic Zn (majority component) and strongly non-stoechiometric ZnO nanophases. This result shows that at high temperature under neutral gas flow, ZnO is dissociated according to the reaction :

$$ZnO \text{ ===> } Zn + \tfrac{1}{2}\, O_2(g) \qquad (4)$$

The produced Zinc is initially at the vapour state. Then, quickly, aggregates are formed. The oxygen produced is pulled out by the argon flow, that is not the case of the zinc aggregates. This distillation phenomenon leads to a zinc content in the nanopowders depending on the collecting position in the reactor.

The Zn nanoparticles produced are very reactive because of their small size. This property can be used to carry out chemical reactions at temperatures lower than those generally practised such as the decomposition of the water vapor :

$$Zn + H_2O(g) \text{ ===> } ZnO + H_2\,(g) \qquad (5)$$

Both reactions (4) and (5) constitute a cycle in which ZnO is conserved. The reaction (4) is endothermic and is a way to store solar energy in the form of heat which is restored partly by the exothermic reaction (5). At the same time hydrogen and oxygen are produced and can be separated and stored for a later use. In a recent work this SPVD process as been used to prepare mixtures of Zn and ZnO nanophases and their reactivity versus water vapour to produce hydrogen as been studied[26].

6. Characterisation and properties of TiO_2 based nanophases prepared by SPVD

6-a SPVD nanopowders of TiO_2 based nanopowders

TiO_2 based nanopowders were prepared using the Solar Physical Vapour Deposition (SPVD) process. Targets were prepared as compressed of 1cm in diameter and 5 to 8 mm height by sintering commercial powders of pure TiO_2 or of mixtures of TiO_2 with doping oxides (Fe, Co or Mn oxides). The vapor pressure around the target depends on the temperature and the atmosphere inside the balloon. At pressures larger than 10 Torr, a smoke is generally visible, it is more or less thick. The smokes are depositing by condensation on a cold finger (water cooled copper tube) located at a few centimeters above the target. The production rate of the nanopowders depends on the vapor pressure of the material. In the case of TiO_2 based targets, the material melts before vaporising, it starts to boil at temperatures in the range of 1500°C but droplets are produced which damage the balloon and it is necessary to limit the working temperature to avoid this phenomenon. In these conditions, the amounts of collected powders are of the order of 10mg/hour.

The nanopowders and targets were characterized by X-Ray Diffraction (XRD), Scanning Electron Microscopy (SEM) and Raman spectroscopy.

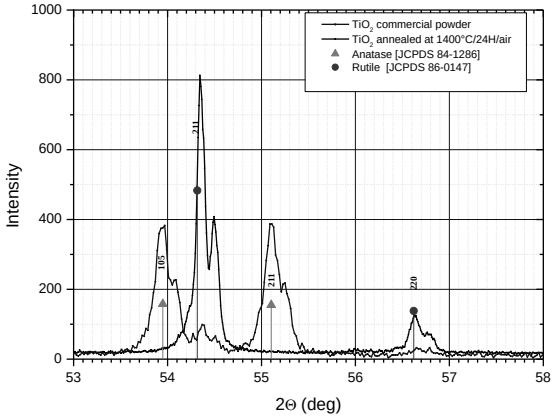

Figure 16 : XRD diagrams showing the transformation from anatase to rutile of the commercial TiO_2 by annealing at 1400°C in air during 24h.

6-b . Characterization of pure TiO_2 SPVD nanophases

6-b-1 XRD diagrams obtained on the targets

TiO_2 commercial powder used to prepare the targets was annealed at 1400°C under air, the X-rays diffraction diagrams obtained before and after annealing are shown in the figure 16. The peaks positions with their indexes referring to the Anatase and Rutile phases (JCPDS 84-

1286 and 86-0147) have been indicated. As already shown by other authors [27], these spectra indicates a dominating presence of the Rutile phase in the annealed powder while Anatase phase is much more abundant than the Rutile phase in the initial raw powder. It is noteworthy to remember that Anatase is generally considered as a metastable phase and Rutile as stable.

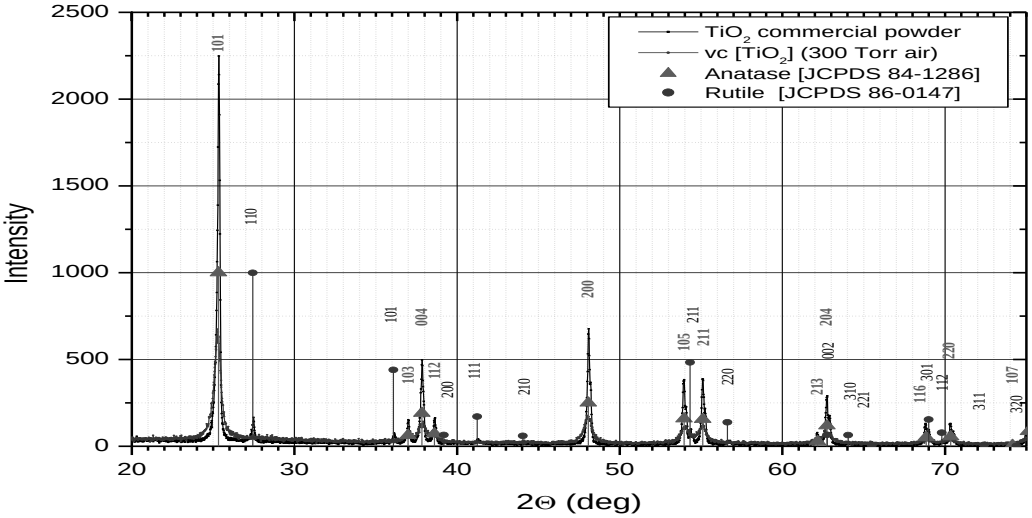

Figure 17 :. comparison between XRD diagrams obtained for a TiO_2 commercial powder and for the nanopowders obtained by SPVD under 300 Torr air pressure.

6-b-2 XRD diagrams obtained on pure TiO_2 nanopowders

Nanopowders were prepared by SPVD under air pressure in the heliotron solar reactor, starting from commercial TiO_2. At low air pressure, TiO_2 is melted before vaporization, and this caused sparkles damaging the reactor. Because of that, the air pressure was maintained up to 90 Torr. The figure 17 shows a diagram obtained on SPVD nanopowders prepared at 300Torr air pressure.

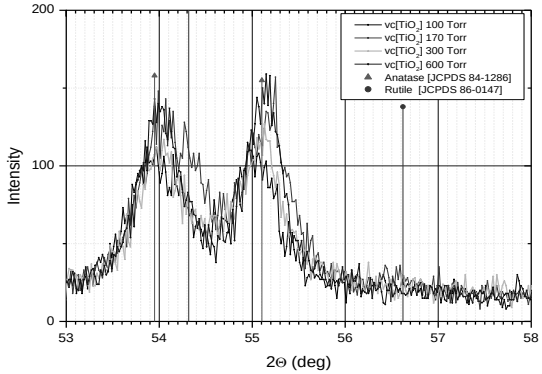

Figure 18-a : Influence of the air pressure inside the solar reactor on the appearance of the anatase (105 and 211 peaks) or rutile phase (211 and 220 peaks) in SPVD nanopowders.

The figure 18 shows a detail of the XRD diagram obtained on the collected nanopowders as a function of the air pressure flowing in the reactor. The variation of the gas pressure in the reactor has an impact not only on the size of the nanophases but also on their crystallographic structure.

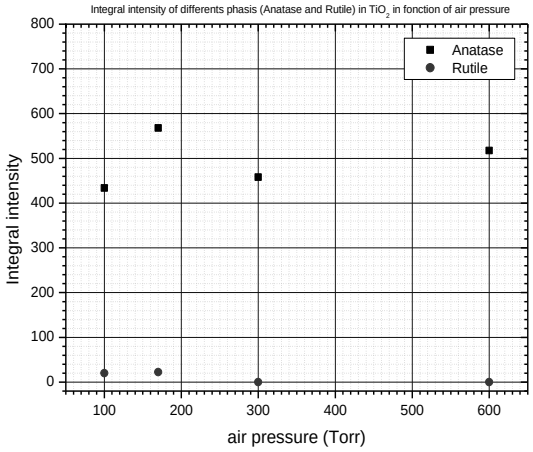

Figure 18-b : Influence of the air pressure inside the solar reactor on the integrated intensities of XRD peaks 101 and 110, corresponding respectively to anatase or rutile.

The figure 18-b shows the evolution of the 110 and 101 peak intensity corresponding respectively to the Rutile phase and to the Anatase phase in function of the air pressure in the reactor. It can be observed on the XRD diagram obtained from nanopowders prepared under 100 and 170 Torr air pressure that the Anatase phase is the majority one and that the intensity of the Rutile peaks decreases gradually. At 300 Torr and at 600 Torr air pressure the Rutile peaks have disappeared.

6-b-3- Raman spectroscopy of pure TiO_2 nanopowders

Nanopowders prepared by SPVD have been studied by Raman scattering and the results compared to those obtained on the commercial powder used to prepare targets. The figure 19 shows that the starting raw material is an heterogeneous mixture of Anatase and Rutile in which Anatase is dominant.

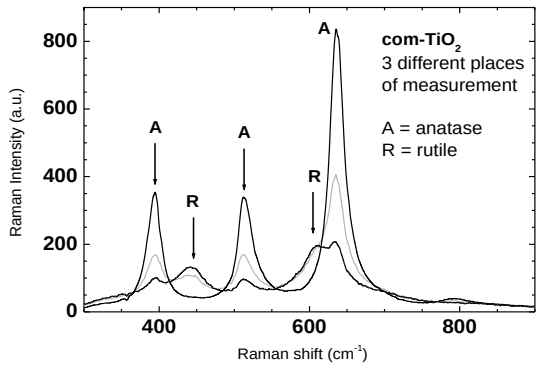

Figure 19 : Raman spectroscopy performed on three samples of the commercial TiO_2 powder

The obtained SPVD nanopowders (see figure 20) are in the Anatase phase when the air pressure in the reactor is higher than 100 Torr and in the Rutile phase below 150 Torr. This is in good agreement with the XRD analysis results (see figures 17, 18-a and b).

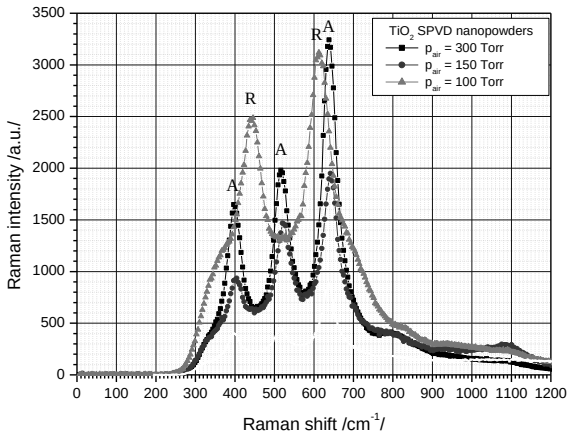

Figure 20 : Raman spectroscopy performed on TiO_2 SPVD nanopowders.

6-b-4 Average grain sizes of pure TiO_2 nanopowders

The procedure presented in §4-b has been used to calculate the grain sizes of the differents phases appearing in the XRD diagram of the nanopowders. The dependence of the average "grain size" of the appearing nanophases as a function of the air pressure during the SPVD process is reported in the figure 21.

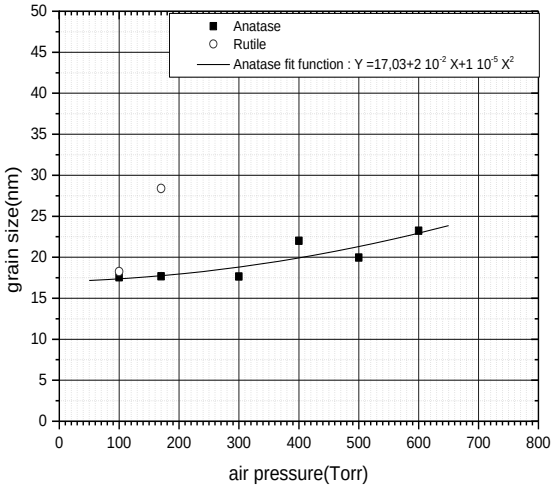

Figure 21 : Average size of the SPVD anatase and rutile nanophases versus air pressure inside the solar reactor.

From figure 21 it appears that these nanopowders are characterized by very small grain sizes. The average grain size of anatase (which is the majority phase) remains practically constant (<18 nm) until 300Torr ; it increases at higher pressure (23nm at 600Torr). The Rutile phase increases in size from 18nm at 100Torr to more than 24nm at 170Torr and vanishes. A fit to the experimental values by a second order polynomial leads to the expression :

$$y = 1\,10^{-5}\,p^2 + 2\,10^{-2}\,p + 17.03 \qquad (6)$$

where the air pressure p is given in Torr and the average grain size y is in nanometers.

Calculations of grain sizes have been carried out from BET measurements using the relation (7).

$$d_m = \frac{6}{S\rho} \times 1000 \qquad (7)$$

Where d_m is in nm when S, the specific BET surface area, is in m^2/g and ρ the picnometric density of the nanopowders is in g/cm^3 (to have a circular form the powder grains are assumed). The results are gathered in table 1.

As BET is sensitive to the surface of the particles and the fact that the particles have similar shapes (see figures 22-a and 22-b), the agreement between the BET and the SEM images is not surprising. Nevertheless there is a large discrepancy between BET and XRD, specially for the nanopowders. The fact that BET measurements lead to a larger grain size than XRD indicates that the grains are nanostructured. SEM images of these nanopowders (see figure 22-b) suggest that the grains of the nanopowders are in fact aggregates (the surface roughness of the grains of the nanopowders is larger than for the commercial powder, many small grains are connected to the large ones).

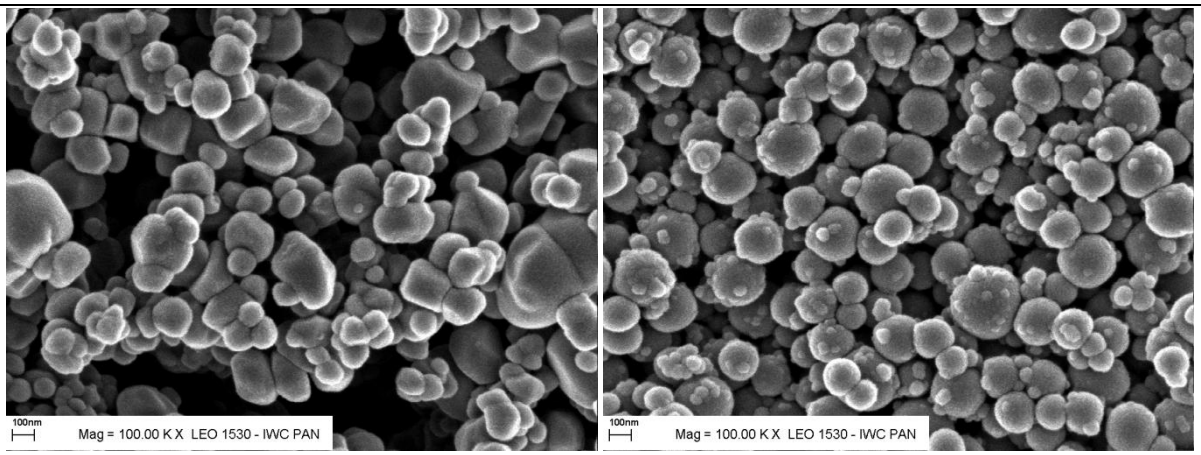

Figures 22-a and 22-b : SEM images of pure TiO_2 commercial powder (a) and SPVD nanopowder (b).

Table1

TiO_2	BET [m^2/g]	Density [g/cm^3]	Average grain size from BET (nm)	Average Grain size from XRD (nm)
Commercial Raw	8.871	3.885	174	57
SPVD nanopowder (300 Torr air)	9.112	3.867	170	18

7. Characterization of Fe, Co or Mn doped TiO_2 SPVD nanopowders

7-a XRD analysis of the Fe, Co or Mn doped TiO_2 nanopowders

The figure 23 shows an example of XRD diagram obtained on a Fe-doped TiO_2 as-prepared target ($Ti_{0.98}Fe_{0.02}O_2$) : as the anatase phase does not appear in XRD diagram, one can consider the majority phase is rutile.

Nanopowders were prepared by SPVD using Fe, Co or Mn doped TiO_2 targets ($Ti_{1-x}M_xO_2$ x is the atomic fraction of M taking the values : 0.01, 0.02, 0.05). The figure 24 shows the XRD diagram obtained on $Ti_{0.95}M_{0.05}O_2$ (M=Co,Fe or Mn) nanopowders prepared under flowing air, the pressure inside the solar reactor being maintained at 10 Torr and the figure 25 corresponds to $Ti_{0.99}M_{0.01}O_2$ (M= Fe, Co or Mn) nanopowders prepared under 90 Torr.

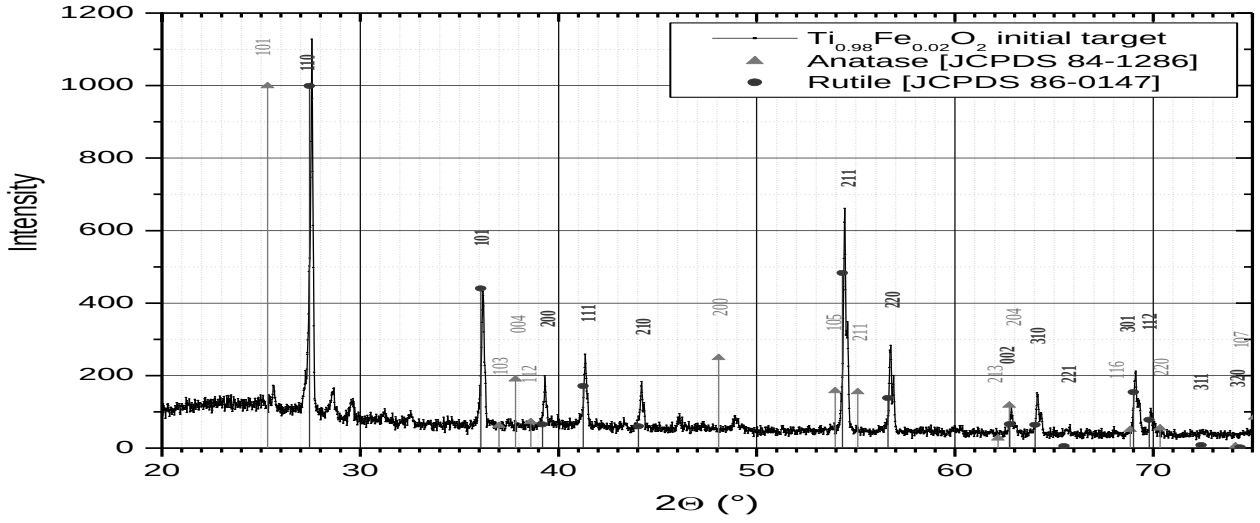

Figure 23 : XRD diagram of a $Ti_{0.98}Fe_{0.02}O_2$target. The majority phase is rutile.

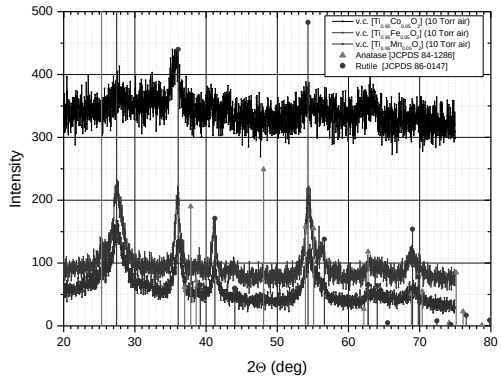

Figure 24 : XRD diagram obtained on $Ti_{0.95}M_{0.05}O_2$ (M=Co,Fe or Mn) SPVD nanopowders prepared under 10Torr air

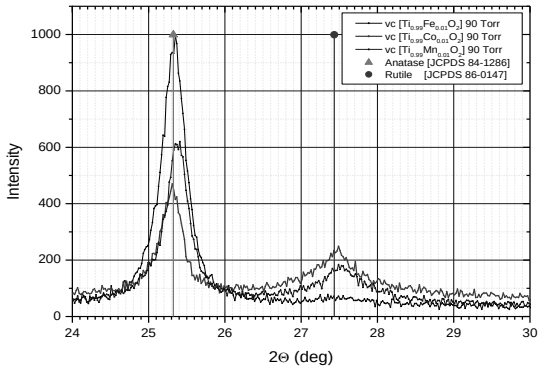

Figure 25 : $Ti_{0.99}M_{0.01}O_2$ (M= Fe, Co or Mn) nanopowders prepared under 90 Torr

The $Ti_{0.95}M_{0.05}O_2$ nanopowders produced under 10 Torr air are essentially in the Rutile phase, the contribution of Anatase is below 5%. For the $Ti_{0.99}M_{0.01}O_2$ nanopowders prepared under 90 Torr the majority phase is Anatase but the Rutile phase appears significantly for the Co or Mn doped samples. In the case of $Ti_{0.99}Fe_{0.01}O_2$, experiments performed at higher air pressure (100Torr and 300Torr) led to similar results as the experiments performed at 90 Torr for $Ti_{0.99}Co_{0.01}O_2$ and for $Ti_{0.99}Mn_{0.01}O_2$. Remembering that the metastable rutile phase has been clearly observed only around 170 Torr for pure TiO_2 during the SPVD process, the observations show that doping at low levels tends to stabilize the rutile phase.

7-b Dependence on air pressure of the nanostructure of the Fe doped TiO_2 nanopowders

The evolution of the diagrams obtained on Fe-doped TiO_2 nanopowders ($Ti_{0.99}Fe_{0.01}O_2$) for two different values of the air pressure inside the reactor is shown in the figure 26.

It can be observed that the ratio of the intensities of two peaks, one belonging to the Anatase phase and the other to the Rutile phase, increases with the pressure.
The shape of the peaks already confirms the observations done under this vaporization air pressure. The peaks intensity of the Anatase phase is even more intense in the case of 300 Torr compared to 100 Torr air. The grain size calculations led to 36 nm for the Anatase phase and 12 nm for the Rutile phase (see table 2).

Table 2

$Ti_{0.99}Fe_{0.01}O$ sample	Grain size (nm)	
Air pressure (Torr)	Anatase(101)	Rutile(110)
initial target	-	52.2
100Torr vc(initial target)	31.2	11.1
300Torr vc(initial target)	35.95	12.5

Table 3

$Ti_{0.98}Fe_{0.02}O$ sample	Grain size (nm)	
Air pressure (Torr)	Anatase(101)	Rutile(110)
initial target	-	69
100 Torr vc(initial target)	10.6	5.0
200 Torr vc(initial target)	40.0	12.4
300 Torr vc(initial target)	43.9	6.0

Similar measurements have been carried out on $Ti_{0.98}Fe_{0.02}O_2$ (see table 3). HRTEM observations show that the particles size is in between 10nm and 30nm (see figure 27 a) with a large mosaicity (see figure 27 b). The small "grain sizes" determined by XRD on the nanopowders ($\cong$ 5 nm for this $Ti_{0.95}Fe_{0.05}O_2$ nanopowders) are hence linked in fact to the substructure size. EELS (Energy Electron Loss Spectroscopy) measurements indicate that the distribution of Fe in the Rutile phase is homogeneous[28].

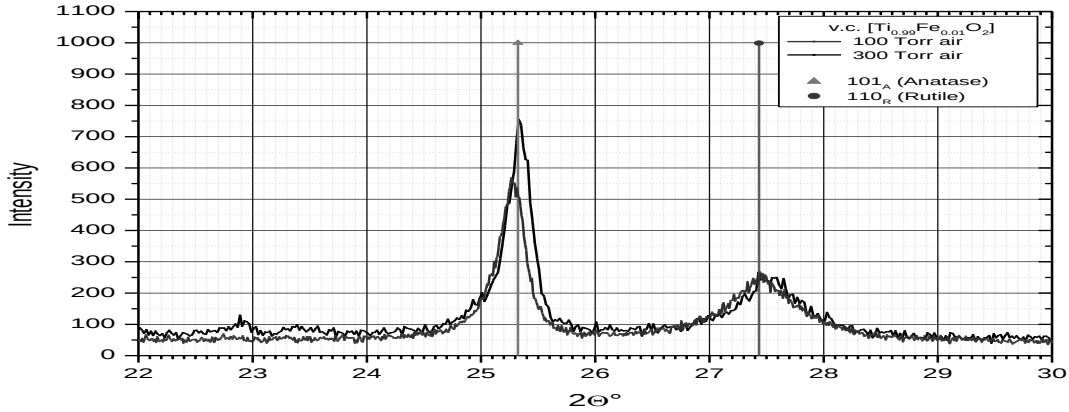

Figure 26 : XRD of SPVD nanopowders ($Ti_{0.99}Fe_{0.01}O_2$) prepared at two different air pressures : 100Torr and 300Torr (detail of the whole diagram).

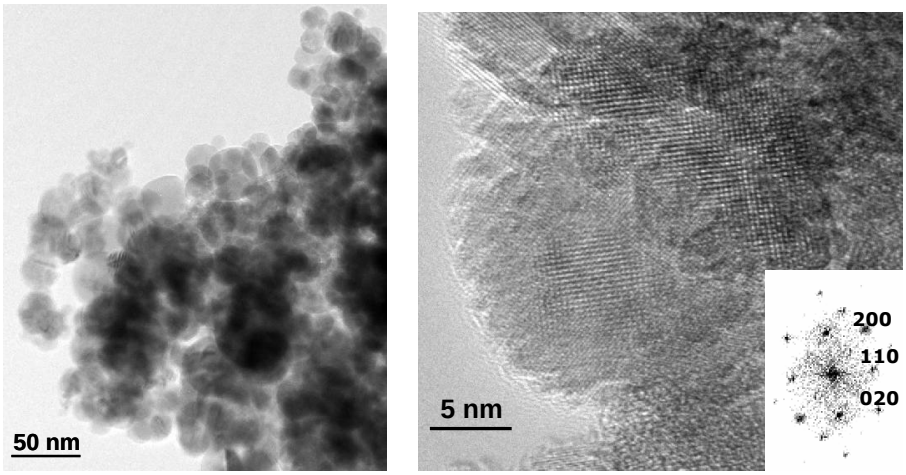

Figures 27-a and 27-b : HREM of Fe doped TiO_2 nanopowders prepared by SPVD.
Magnetic measurement and Mössbauer Spectroscopy of Fe doped TiO_2 nanopowders ($Ti_{0.95}Fe_{0.05}O_2$) performed at T=5K, showed that these nanophases are not ferromagnetic but in a paramagnetic state [28].

8. Discussion about the TiO_2 phase stability

Well annealed pure TiO_2 commercial powders are in the Rutile phase. It has been shown in this work that pure TiO_2 nanopowders prepared by SPVD are in the Anatase phase. For air pressure up to 100Torr, the Rutile phase does not appear. At the lowest pressures studied (100 and 170 Torr air), the Rutile phase appears as a minority phase beside the Anatase. Raman spectra is in agreement with the XRD analysis.

These result can be interpreted by capillarity effects : due to their small size and to the surface tension, the pure TiO_2 nanoparticles are stabilised in the Anatase phase. In addition, a thermokinetic effect can also be considered. At high pressures indeed, the air flow in the reactor is smaller than at low pressures and the cooling rate of the smokes produced during the SPVD process, is slower. At low pressures the phase transformation from Rutile to Anatase is not fully achieved. This is well supported by the observed increase of the average grain size while the pressure increases.

In doped TiO_2 targets made with annealed mixtures of powders, the Rutile phase is the majority phase. After vaporisation-condensation under low pressure and with a high dope content of the target, the majority phase is the Rutile but at low dope content and with high pressure during the SPVD process, leads to the decrease of the Rutile amount compared to the Anatase one.

The addition of dopes leads to stabilise the Rutile phase but the increase of the pressure has again the same effect as for pure TiO_2 : the Rutile phase amount is less and less important while the pressure increases at constant composition of the target. Using the same arguments as for pure TiO_2 it seems that the surface tension of doped particles decreases when a dope is present, the effect of the air pressure being similar to what has been explained for pure TiO_2. An investigation of surface segregation phenomena in this system could enlighten on this problem.

9. Preparation, characterisation and properties of magnetic composite nanophases

In the previous examples presented earlier nanopowders were obtained from targets prepared in conditions where the nanophases, component of the nanopowders, were expected to be simple and unique. In fact it has been seen,

it was not the case, the stability of the nanophases appearing being not ascertained in all cases including simple cases such as the classical unstable γ–Fe_2O_3 [29] or the case of TiO_2, where two phases, one being unstable, appear in proportions varying with the SPVD conditions. In the more complex case of targets made of ZnO+Bi_2O_3, two kinds of nanophases or more appear but that's less surprising.
To offer an alternative to chemical processes biologically not fully satisfying, a program of preparation by SPVD of nanoparticles used in medicine as markers for magnetic resonance imaging and heating mediators and preserving their biological environment was proposed. The idea was to prepare composite nanophases made by a magnetic core surrounded by a bio-compatible shell. The challenge being to do that by SPVD.
Good results have been obtained with Fe nanoparticles coated with MgO [13].

Targets were obtained by mixing and pressing pure Fe and MgO powders with an excess of Mg in such a way to keep reducing conditions. The SPVD process was performed in an argon flow.
XRD diagram performed on the nanopowders is shown in the figure 28. The MgO peaks and Fe peaks are clearly distinct. HREM images show the core-shell nanostructure of the composite nanophases obtained (see figure 29). Figure 30 shows their magnetic behaviour[13].

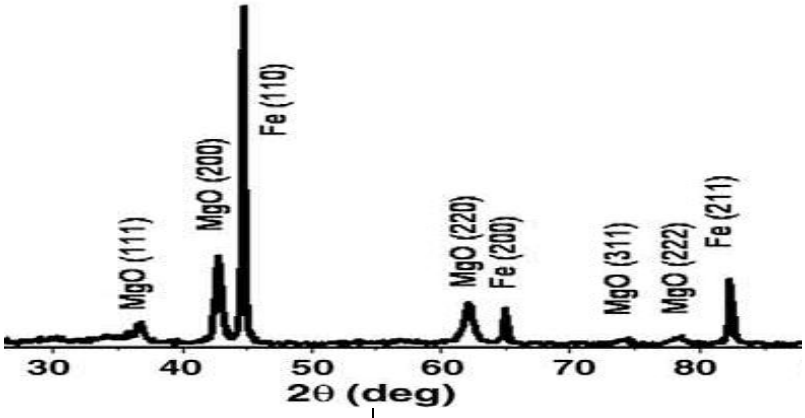

Figure 28 : XRD diagram of SPVD MgO coated Fe composite nanophases

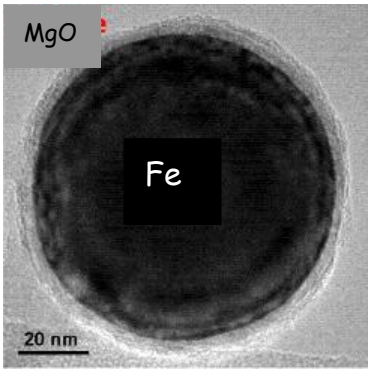

Figure 29 : MgO coated Fe nanophases prepared by SPVD. The magnetic properties of such composite nanophases have been determined. They behave as ferromagnetic .

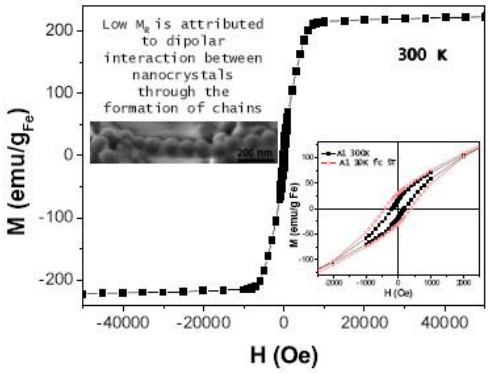

Figure 30 Magnetic behaviour of MgO coated Fe nanophases.
The low field region (inset) show a weak hysteresis effect.

Biological tests have demonstrated the stability of such nanoparticles. Their biocompatibility and their affinity for particular cells of the liver, spleen or kidneys lead to use them for magnetic imaging and targeted treatment of human diseases by hypothermia.

10.Conclusion

Several types of nanopowders were prepared in order to know the influence of the grain size on the known properties of materials. If new properties appear, specially at small grain size (nanomaterials), they open new fields of research. In many cases, it is on massive nanomaterials or in layers, that appear the new properties and the preparation of these nanomaterials is an important stage to cross. Among the compounds prepared by SPVD, we were focused in this study on ZnO based nanophases. $Zn_{1-x}Al_xO$, when it is prepared by SPVD, appears to be a remarkable blue emitter by luminescence and can be used to build luminescent screens or sensors. $Zn_{1-x}Co_xO$ is generally paramagnetic but can exhibit a ferromagnetic behaviour in

the form of nanopowders and could be used in optoelectronics.

The bi-phased compounds $Zn_{1-x}Bi_xO$-$(Bi_{1-y}Zn_y)_2O_{3-z}$, have very interesting electrical properties and they could be used as electrolytes in SOFC working at temperatures as low as 400°C. Production of metallic Zn nanophases could be a powerful solution to the solar energy storage and/or hydrogen production. Composite nanophases, such as the MgO coated Fe nanoparticles core-shell nanostructured, open new possibilities for medicine because of their biocompatibility and magnetic properties.

The few examples presented here highlight the interest of SPVD methods to work on nanopowders with remarkable properties it still remains to discover the best way of implementing them in the applications.

Acknowledgements

Many results presented here wer obtained in the frame of collaborative works supported by the European programs SOLFACE and SFERA. The managers of this helpful sponsoring are greatly acknowledged.

References

[1] C.J.A. Monty, The Arabian Journal for Science and Engineering, 35, 1C, (2010)93-116.

[2] C.J.A. Monty, High Temperatures and Chemical Process. 3, (1994)467-480.

[3] G.C. Hadjipanayis, R.W. Siegle,. *Nanophase Materials : Synthesis – Properties – Applications.* Series E : Applied Sciences, vol. 260, Kluwer Academic Publishers, Dordrecht, (1994)

[4] A. Rouanet, G. Pichelin, C. Roucau, E. Snoeck, C. Monty, Nanophase Materials; Kluwer Academic Publishers: Dordrecht, the Netherlands, (1994)85-88.

[5] A. Rouanet, H. Solmon, G. Pichelin, C. Roucau, F. Sibieude, C. Monty, Nanostructured Materials. 6(1-4), (1995)283-286.

[6] C. Monty, Ecole d'Eté CNRS, St. Pierre d'Oleron. (2005)231-259.

[7] J. Friedel, Phase transitions, 24-26 (1990) 215-227.

[8] C.J.A. Monty, A. Rouanet, F. Sibieude, Materials Science Forum. (1998)269-272, 297-302.

[9] N. Boulares, K. Guergouri, R. Zouaghi, N. Tabet, A. Lusson, F. Sibieude, and C. Monty, Physica Status Solidi (a), **201**, 10, (2004)2319-2328.

[10] C. Monty, Ionics, 8(5-6), (2002)461-469.

[11] T. Ait Ahcene, C. Monty, J. Kouam, A. Thorel, G. Petot-Ervas, A. Djemel, J. European Ceramic Society. 27, (2007)3413-3424.

[12] J. Kouam, T. Ait Ahcene, A.G. Plaiasu, M. Abrudeanu, A. Motoc, E. Beche, C. Monty, Solar Energy, 82, (2008)226-238.

[13] C. Martinez-Boubeta, Ll Balcells, R. Cristòfol, C. Sanfeliu, E. Rodriguez, E. Weissleder, S. Lope-Piedrafita, K. Simeonidis, M. Angelakeris, F. Sandiumenge, A. Calleja, L. Casas, C. Monty, and B. Martínez., Nanomedicine : Nanotechnology, Biology, and Medicine, NANO-00307 (2009).

[14] F. Teixera, R. Berjoan, G. Peraudeau, D. Perarnau, Solar Energy. 78(6), (2005)763-771.

[15] G. Flamant, , D. Luxembourg, , J-F. Robert, , D. Laplaze, , *solar reactor*. Solar Energy. 77, (2004)73-80.

[16] L. Bragg, *The crystalline state*. G. Bell Londres, **1**, 1949.

[17] J.I. Langford, D. Louër, E.J. Sonneveld, J.W. Visser, Powder Diffraction. 1(3), (1986)211-221.

[18] C. Boudias, D. Monceau, 1989-2005, http://pros.orange.fr/carine.crystallography/

[19] R.R. Piticescu, B. Malic, M. Kosec, A. Motoc, C. Monty, I. Soare, T. Kosmac, A. Daskobler, J. European Ceram. Soc. 24(6), (2004)1941-1944.

[20] R.R. Piticescu, R.M. Piticescu, C. Monty, J. European Ceram. Soc. 26, (2006)2979-2983.

[21] J. Grabis, Dz.Jankovica, M. Berzins, L. Chera, I. Zalite, J. European Ceram. Soc. 24(2), (2004)179-184.

[22] L. Grigorjeva, D. Millers, K. Smits, C. Monty, J. Kouam, , L. El Mir, Solid State Phenomena 128, (2007)135-140.

[23] T. Strachowski, E. Grzanka, W. Lojkowski, A. Presz, M. Godlewski, S. Yatsunenko, H. Matysiak, R.R. Piticescu, C.J. Monty, Journal of Applied Physics 102, (2007)073513.

[24]B. Martínez, F. Sandiumenge, L. Balcells, J. Arbiol, F. Sibieude, C. Monty, Appl. Phys. Lett. 86, (2005)103-113.

[24] B. Martínez, F. Sandiumenge, L. Balcells, J. Fontcuberta, F. Sibieude, C. Monty, J. Appl. Phys. 97, (2005)10D311.

[24] B. Martínez, F. Sandiumenge, L. Balcells, L. Arbiol, F. Sibieude, C. Monty, J. Phys. Rev. B. 72, (2005)165202 .

[25] O. Monnereau, L. Tortet, P. Llewellyn, F. Rouquerol, G. Vacquier, Solid State Ionics. 157, (2003)163-169.

[26] M. Chambon, S. Abanades, G. Flamant, International Journal of Hydrogen Energy 34, (2009)5326-5336.

[27] C.N. Rao, and K.J. Rao, *Phase transitions in solids*. chap 2, McGraw-Hill, New York (1978)

[28] Ll. Balcells, C. Frontera, F. Sandiumenge, A. Roig, B. Martinez, J. Kouam, and C. Monty, Appl. Phys. Lett., **89**, (2006)122501-3.

[29] B. Martinez, X. Obradors, L. Balcells, A. Rouanet, C. Monty, Phys. Rev. Lett. 80, (1998)181-184.

Journal of New Technology and Materials
JNTM
Vol. 01, N°00 (2011) 24-28

OEB Univ. Publish. Co.

Low Copper Doped CdO Nanowires Grown by Sol-Gel Route

M. Benhaliliba[a*], C.E. Benouis[a*], A. Tiburcio Silver[b]
[a] *Physics Department, Sciences Faulty, Oran University of Sciences and Technology USTOMB, BP1505 Oran, Algeria.*
[b]*ITT-DIEE, Apdo, Postal 20, Metepec 3, 52176, Estado de Mexico, Mexico.*
*Corresponding author bmost_31@yahoo.fr, Tel. +213772211491
Received: 23 May 2011, accepted: 30 September 2011

Abstract
In the current work, pure and copper doped cadmium oxide ($Cd_{1-x}Cu_xO$, x=0, 0.02, 0.03) thin films are grown by sol-gel spin coating route. Optical transmittance is measured in UV, VIS and IR spectra; it is revealed that the copper improves the transmittance. The optical band gap increased with the doping. The room temperature electrical resistance was affected by copper doping. The AFM morphology reveals that pure CdO and Cu doped thin films are nanostructured.
Keywords: *Sol-gel spin coating, Grain size, CdO, Cu level doping, Nanowires, Optical properties, AFM investigation.*

1. Introduction

Currently, Cadmium oxide (CdO) is among of interesting conducting oxide (TCO) group such as tin oxide (SnO_2) [1], indium oxide (In_2O_3) [2], indium tin oxide (ITO) [3] and zinc oxide ZnO [4-5] due to its high electrical and optical properties. Cadmium oxide (CdO) is n type semiconductor with direct band gap found to be 2.3 eV and it exhibits a cubic system and the lattice parameter is 4.695 Å [6]. Thin-film deposition techniques are either purely physical, such as evaporative methods, or simply chemical, such as gas and liquid phase chemical processes like sol-gel [7]. Furthermore, CdO has been deposited also by chemical bath (CBD) [8], spray pyrolysis [9], sputtering [10] and thermal evaporation [11]. Cadmium oxide is one of the promising II-VI family of semiconductors which has a great potential for optoelectronic devices [12]. CdO was doped with many elements such as Li [13], Al [14], Fe [15], Ga [16], Sm [17] and Eu [18, 19]. Up to our knowledge, there is no works published on the preparation and structural, UV-VIS-IR optical, AFM morphological and electrical properties investigation of Cu doped CdO. Our work consists on the preparation and characterization of CdO doped with transition metal (Cu), in the proportion 2 % and 3 %, to stand up their characterization for the advanced technological applications. The influence of Cu doping level on structural, optical, morphological, electrical properties of CdO synthesized by facile sol-gel spin coating route is investigated.

2. Experimental procedure

2.1. Films preparation

route onto microscope glass slides (76 x 26) mm^2 supplied by object trager Isolab. 0.5 Molar of cadmium acetate dihydrate ($Cd(CH_3COO)_2.2(H_2O)$) (purity of 99 %) supplied by Himedia, was dissolved in 10 ml of 2-Methoxyethanol ($C_3H_8O_2$) stirred at 60°C for 10 mn. The doping precursor was copper (II) acetate anhydrous $Cu(CH_3COO)_2$, (purity of 98 %) supplied by Carlo Erba reagents and then 0.3 ml of the Mono-Ethanolamine (MEA) C_2H_7NO (of molar mass 61.08 g/mol and density = 1.015) as stabilizer, was added drop by drop until the homogeneous and clear solution was obtained, then the stirring continued for 1hour. Consequently, the solution was aged for 24 hours until the gel formation at ambient (see scheme 1 and 2 [20]).

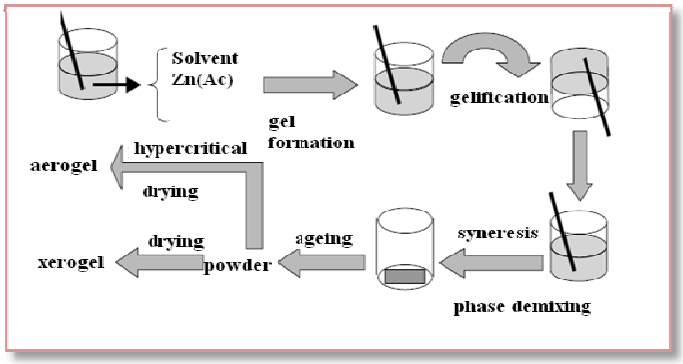

Scheme 1. Different steps of sol-gel process. (Aerogel is a manufactured material with the lowest bulk density of any known porous solid. It is derived from a gel in which the liquid component of the gel has been replaced with a gas), (Xerogel is a solid formed from a gel by drying with unhindered shrinkage. Xerogel is usually retain high porosity (25%) and enormous surface area (150–900 m^2/g), along with very small pore size 1-10 nm)[20].

Scheme 2. Sol-gel processing and ageing steps, resin formation

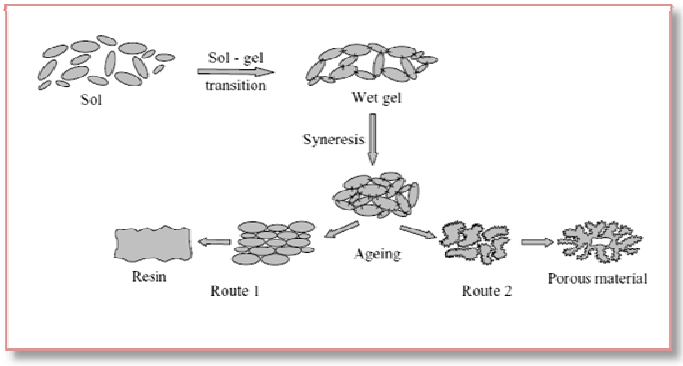

(route1) and porous solid material formation (route 2) [20].

The viscous solution was homogenously poured using micropipette on the substrate sticked on stainless steel spin plates of MTI, EQ-TC-100 Desk-top Spin Coater. The sample

rotates for one minute at speed of 1200 rotates per minute (RPM), the sample was heated at 150 °C for 10 mn and then the process was repeated 5 times, finally the film was annealed at 400 °C for 1hour under air in furnace MF 120 Nuve.

2.2. Films characterization

X-rays pattern of samples were carried out in Bruker AXS D8 Discover diffractometer, $CuK_{\alpha 1}$ (λ = 1.5418 A°) is used. The films coated transmittance and reflectance were recorded by Shimadzu 3600 PC double beam UV-VIS-NIR spectrometer, the electrical resistance at room temperature was then determined by four probes method. AFM observations of the coated films were made by using a Quesant Model 250 system having an 80x80 micrometer head, in the wave mode in air. For the (10 x10) micrometer square images the resolution was (300 x 300) pixels, the scan rate was 2 Hz for all cases. All analyses were performed with the software from the WSXM system

3. Results and discussion

3.1. Structural analysis

The figure 1A shows the X- rays diffraction pattern of pure and copper doped cadmium oxide where the angle ranges within 20°-80°. The grain size G is given by the well-known Scherrer's formula (1)[4],

$$G = \frac{0.94\ \lambda}{\beta\ \cos\ \theta} \quad (1)$$

Where β is the full width at half medium of the peak, 2θ is the Bragg angle and λ is X- rays wavelength. The calculated values of G are listed in table1.

Table1: Some parameters are calculated for pure and copper doped CdO

Sample	Grain size (nm)			TC (111)	E_g (eV)			T (550 nm) (%)
	(111)	(200)	(220)		$(\alpha h\nu)^2$	dT/dλ	dR/dλ	
CdO	8.235	8.245	6.199	1.80	2.49	2.59	2.52	56
CdO: Cu 2%	11.246	9.662	7.471	1.72	2.50	2.59	2.59	68
CdO: Cu 3%	8.801	7.853	7.122	1.73	2.56	2.62	2.59	79

The comparison of the observed XRD patterns with the standard JCPDS data (05-0640) confirms the structure of CdO phase with face centered cubic crystal structure [21]. The X rays pattern reveals that all investigated coated films are polycrystalline of cubic CdO structure and Bragg position for strong reflections like (111) direction was 32.92°, 33.08° and 33.09° respectively for pure and doped (2 % and 3 %) CdO coated films, and then a slight angle shift, estimated at 0.03°-0.16°, was carefully detected as sketched in fig. 1B. Others reflection positions (2θ) and their angle shifts are listed in table2.

Table1: X-rays results of pure and copper doped CdO

(hkl)		Bragg angle 2θ (°)	Angle shift Δ(2θ) (°)
(111)	CdO	32.92	-
	2%Cu	32.95	0.03
	3%Cu	33.08	0.16
(200)	CdO	38.12	-
	2%Cu	38.26	0.14
	3%Cu	38.43	0.31
(220)	CdO	55.06	-
	2%Cu	55.13	0.07
	3%Cu	55.30	0.24
(311)	CdO	65.70	-
	2%Cu	66.25	0.55
	3%Cu	66.42	0.72

These results are in well agreement with those of literature [22]. It seems that the CdO coated films have a preferential growth along the (111) direction. Most important peaks of CdO phase (111), (200), (220), (311) and (222) are shown in figure 1A. Textural coefficient is given by TC = I_{111}/ (1/4) (I_{111}+I_{200}+ I_{220}+I_{311}) [4] and data are tabulated according to (111) direction. The discrepancy in TC parameter is very low which confirms the crystalline structure is maintained at low doping level. Consequently, according to both (111), (220) orientations, copper doping increases the grain size, while 3 % copper level doping reduces it. As shown in figure 1B, CdO is present in coated film as confirmed by JCPDS card No. 05-0640, while a slight (2θ) shift to higher angle is caused by Cu doping. The ionic radii of Cu (II) and Cd (II) are respectively 0.73 Å and 0.95 Å and ionic radius ratio is $r_{Cu\ (II)}$/ $r_{Cd\ (II)}$=0.77, then cooper has minor radius than cadmium, it may diffuse in host lattice without causing mismatch or distortion, this fact corroborates with the slight angle shift. Figure 2 illustrates grain size of samples grown by spin coating route according to (111), (200) and (220) orientations. The grain size sweeps in average of 6 nm, these values due to X rays peaks broadening are minor; this confirms the nanostructures aspect of our coated films. Furthermore grain size is increased by the Cu doping level (2 %).

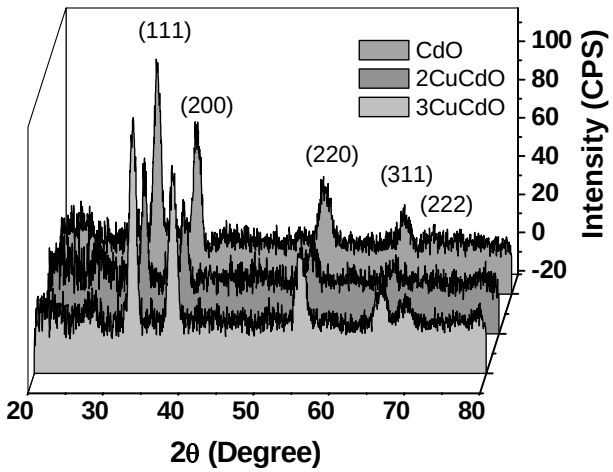

Figure 1A. X-rays pattern of pure and copper doped CdO grown by spin coating process at 1200 RPM, Bragg angle ranges within 20°-80°.

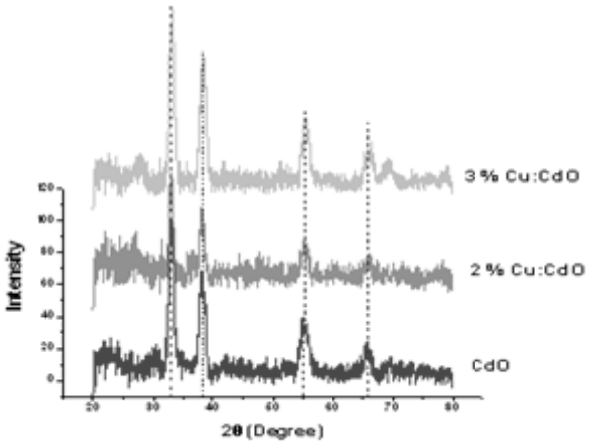

Figure 1B. JCPDS card No 05-0640 of pure and copper doped CdO are sketched (red dash lines). Slight angle shift (2θ) to higher angle is observed.

1.1. Optical characterization

The transmittance of pure and copper doped (2 % and 3 %) cadmium oxide grown by sol-gel is depicted in figure 3 within the wavelength range 200-2500 nm. The transmittance plot in visible spectrum, of studied samples and pure glass, is observed inset of fig.3. As can be seen the transmittance grew up rapidly in UV-VIS range until 85% for 3 % Cu doped CdO sample and continues to increase monotonically in the VIS and NIR spectra. It reaches a maximum found to be 91 %, 90 % and 89 % in IR for the 3 %, 2% Cu doped CdO and pure CdO respectively and then transmittance decreases slightly with copper doping level. Similar evolution is observed in Kumaravel paper [9, 23]. Subramanyam has found the same trend profile of transmittance in VIS and IR spectrum for the CdO films grown by DC magnetron sputtering for one particular oxygen pressure [24]. We remark that Cu ions improve considerably the optical transmittance particularly in visible range (see inset of fig.3). The average transmittance at 550 nm increases with doping level, as listed in table 1, and confirms the previous statement. We mention that low copper level doping improves the transmittance around visible edge (750-800 nm) where transmittance of 3 % Cu doped CdO approaches the pure glass transparency as can be easily seen inset of fig.3. The direct optical band gap is expressed as [4],

$$\alpha h\nu = (h\nu - E_g)^{0.5} \qquad (2)$$

Where E_g (eV) is the optical band gap, α (m^{-1}) is the absorption coefficient and ν (Hz) is the photon frequency. Band gap E_g estimates were derived from the optical transmission spectra by extrapolating the linear portion of the plot of $(\alpha h\nu)^2$ against hν to α=0 as plotted in figure 4. It varied with doping level, the pure sample exhibits E_g equals to 2.49 eV , the samples 2 % and 3 % Cu doped have respectively 2.50 and 2.56 eV as sketched in figure 4 and listed in table 1. While the optical band gap was found by T.P. Gujar is 3.18 eV [25] and Kumaravel has reported a value of E_g ~2.53 eV [23]. Others works exhibit an average of E_g around 2.46 eV [24]. Our results are in accordance with those obtained in literature [23, 24]. The estimated energy gap from $(\alpha h\nu)^2$, dT/dλ and dR/dλ (reflectance is not shown here) of pure and Cu-doped CdO films are given in Table 1. There is an effect of the Cu dopant concentrations but not regular in the studied range on the optical band gap estimated from dR/dλ versus λ (not shown here) suggesting that the optical band gap shifts from 2.49 to 2.62 eV. These gap values lead to a blue shift which may be explained by Burnstein-Moss effect. Our results are in well agreement with those of literature [6]. Fluorine has increased the band gap as reported by Akyuz [26].

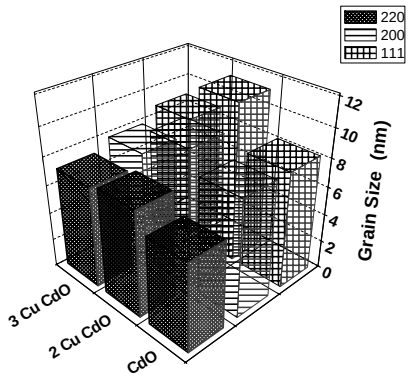

Figure 2. Grain size plot against Cu content according to (111), (200) and (220) directions

1.2. Surface morphology investigation

The 2D and 3D AFM investigation is shown in figure 5, picture have dimensions 10 x 10 micrometers. Overall, the surface of CdO coated film is homogeneous with few voids which are signed by circles as depicted in 2 D views (see fig. 5 left). Pure CdO nanograins look like mounts with no well defined boundaries; the average of grain size is 0.075 µm and height equals to 742 nm. Pure CdO coated film reveals agglomerated regions with different asperity, the bright ones (signed by arrows in fig. 5A) attract more atoms during the growth process than the dark ones which might demonstrate cavities. Similar morphology shape was reported in literature [23, 27]. 2 % Cu doped CdO sample reveals columns like wires which are separated and grown in the same direction having an average height equals to 275 nm , the 3 % Cu doped CdO shows the same shape of wires with big nanowires density (number of nanowires per μm^2) and major height (~382nm). Clusters of nanowires exhibit different sizes 0.186 µm (2 Cu % doped CdO), 0.208 µm (3 Cu % doped CdO). We conclude that low copper doping level influences the surface morphology of cadmium oxide coated film and tends to make longer the nano-grains into nanowires.

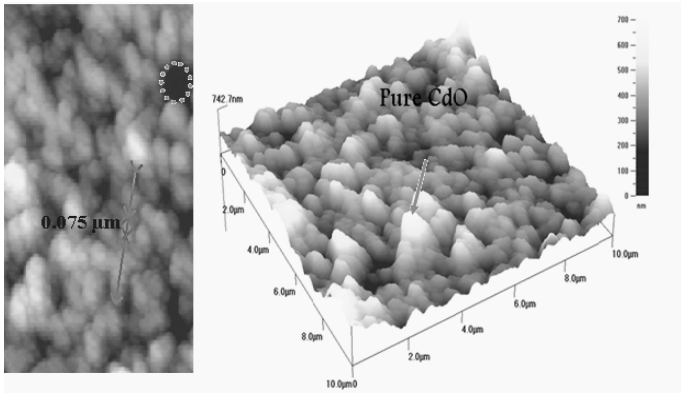

Figure 5A. AFM topography image of pure CdO coated films. AFM Pictures are 10x10 μm^2, grain size and voids are shown in (left) 2D view and (right) 3D view, (height is shown at left corner of 3D image, arrow shows nano-mounts.

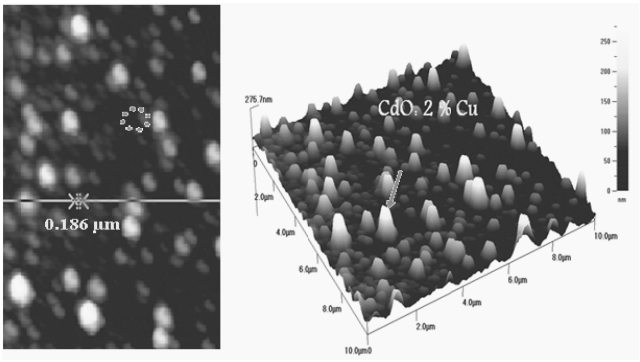

Figure 5B. AFM topography image of 2 % Cu doped CdO coated films. AFM Pictures are 10x10 µm², grain size and voids are shown in (left) 2D view and (right) 3D view, (height is shown at left corner of 3D image, arrow shows nanowires.

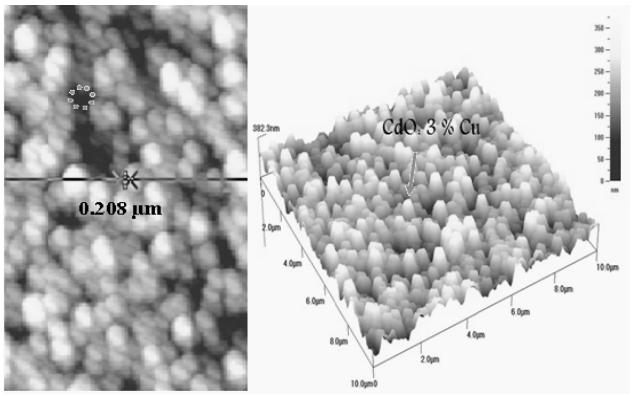

Figure 5C. AFM topography image of 3 % Cu doped CdO coated films. AFM Pictures are 10x10 µm², grain size and voids are shown in (left) 2D view and (right) 3D view, (height is shown at left corner of 3D image, arrow shows nanowires.

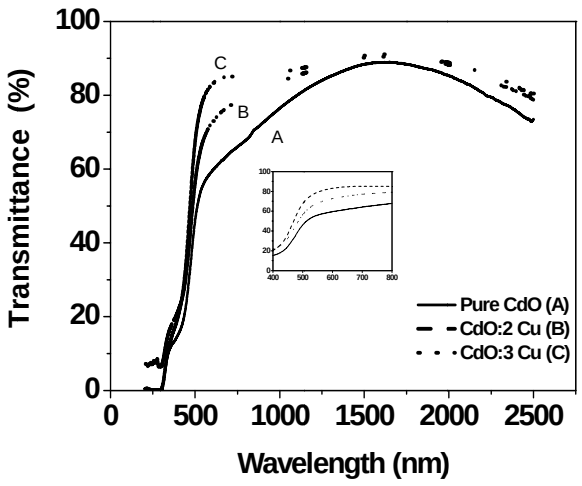

Figure 3. Transmittance dependence on photon wavelength of pure, 2 and 3% Cu doped CdO grown by spin coating at 1200 RPM, inset shows VIS transmittance profile of pure, 2 % Cu and 3% Cu doped CdO and pure glass of substrate.

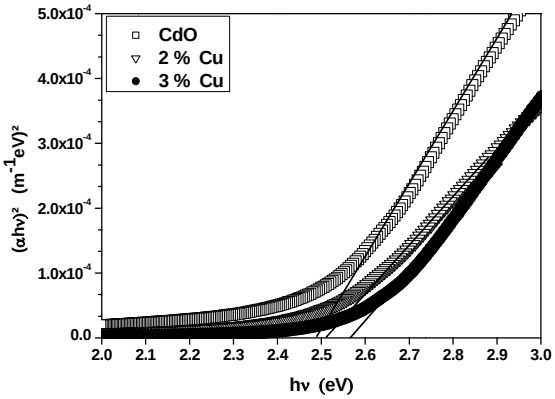

Figure 4. Dependence of $(\alpha h\nu)^2$ on incident photon energy (hν) of undoped CdO , % 2 and 3 % Cu doped CdO, (extrapolation straight lines are depicted).

1.3. Electrical measurement

The electrical measurement was carried out in four probes set up as can be seen inset of figure 6 and the electrical resistance at room temperature is depicted in figure 6. The electrical resistance R was calculated by using [28],

$$R = k\frac{V}{I} \qquad (3)$$

Where k is a constant found to be 4.53, V is the applied voltage and I is the intensity of DC current. It is observed that copper level doping diminishes greatly the resistance by about 5 and 400 times for 2 % and 3 % Cu doped CdO respectively. This fact is due to copper, which has two level of oxidation I and II, can substitute to cadmium sites and offers free electrons which can improve the conductivity.

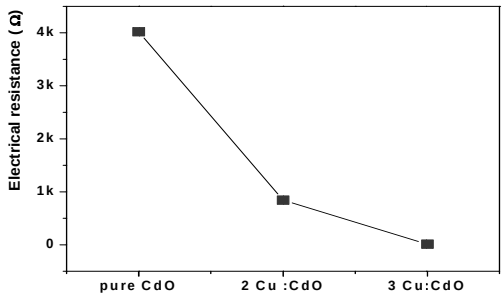

Figure 6. DC resistance at ambient is plotted versus Cu amount. Inset shows the four probes set up scheme

Conclusion

The pure and Cu doped CdO films structural, 2D and 3D AFM views, optical properties were investigated. It is revealed that CdO phase is obtained and the grain size reaches up to 11 nm according to (111) direction and TC decreases a little with copper doping level. A peak broadening reveals nanostructures formation of our coated films. High transparent coated films in VIS-IR range are obtained and low copper level doping improves the transmittance mainly in visible band edge from 56 % to 79%, and exceeds the point of 90 % in IR spectrum. Band

gap increases with copper level doping and demonstrates a blue shift. Low copper doping level maintains the crystalline structure, extends the grains and transforms them to high transparent nanowires and reduces the ambient resistance. These characteristics of high VIS-IR transparency and low resistive nanowires can provide to our coated films, produced by facile sol-gel route, various applications in material sciences and optoelectronics devices which can be investigated in next work.

Acknowledgements

This work, under contract number D 01920080054, is included in project "*CNEPRU2009-2012"* supported by the Algerian High Level Teaching and Scientific Research Ministry MESRS and Oran Sciences and Technology University USTOMB. The author would like to acknowledge the generous assistance of Pr F. Yakuphanoglu, Physics Dpt., Firat University Turkey, for his help in optical measurements, Mr. A. Avila-García, A. Tavira, Cinvestav-IPN, "Dept. Ingeniería Eléctrica", and R. R. Trujillo, "Centro de investigación en dispositivos semiconductors", Mexico for their fruitful help in performing AFM and X-rays pattern observations.

References

[1] C.E. Benouis, M. Benhaliliba, F. Yakuphanoglu, A. Tiburcio Silver , M.S. Aida, A. Sanchez Juarez, Synthetic Metals (2011). D.O.I. 10.1016/j.synthmet.2011.04.017.
[2]G. Korotcenkov , A. Cerneavschi , V. Brinzari ,A. Vasiliev , M. Ivanov, A. Cornet , J. Morante , A. Cabot , J. Arbiol, Sensors and Actuators B 99 (2004) 297-303.
[3] M.K. Fung, Y.C. Sun, A.M.C. Ng, A.B. Djurisic, W.K. Chan, Current Applied Physics 11 (2011) 594-597.
[4]M. Benhaliliba, C. E. Benouis, M. S. Aida, F. Yakuphanoglu, A. Sanchez Juarez, J. Sol-Gel Sci. Technol. 55, 3, (2010)335-342, doi 10.1007/s10971-010-2258- x.
[5]M. Benhaliliba, C.E. Benouis, M.S. Aida, A. Sanchez Juarez F. Yakuphanoglu , A. Tiburcio Silver, J. Alloys Compd. 506 (2010) 548-553.
[6] Xiaofei Han, Run Liu, Zhude Xu, Weixiang Chen, Yifan Zheng, Electrochemistry Communications 7 (2005) 1195-1198.
[7]Seval Aksoy, Yasemin Caglar, Saliha Ilican, Mujdat Caglar, International journal of hydrogen energy 34 (2009) 5191-5195.
[8] A.S. Kamble, R.C. Pawar, N.L. Tarwal, L.D. More, P.S. Patil, Materials Letters 65 (2011) 1488-1491.
[9]R. Kumaravel, K.Ramamurthi, Indra Sulania, K.Asokan, D.Kanjilal, D.K.Avasti, P.K.Kulria, Radiation Physics and Chemistry 80 (2011) 435-439.
[10]Qiang Zhou, Zhenguo Ji, BinBin Hu, Chen Chen, Lina Zhao, Chao Wang, Materials Letters 61 (2007) 531-534.
[11] H.B. Lu, L. Liao, H. Li, Y. Tian, D.F. Wang, J.C. Li, Q. Fu, B.P. Zhu , Y. Wu, Materials Letters 62 (2008) 3928-3930.
[12]A. Gulino, G. Tabbi, Appl. Surf. Sci. 245 (2005), 322-327.
[13]A.A. Dakhel, Effect of thermal annealing in different gas atmospheres on the structural, optical, and electrical properties of Li-doped CdO nanocrystalline films, Solid State Sciences (2011), doi:10.1016/j.solidstatesciences.2011.02.002.
[14]K.R. Murali, A. Kalaivanan, S. Perumal, N. Neelakanda Pillai, Journal of Alloys and Compounds 503 (2010) 350-353.
[15] A.A. Dakhel, Thin Solid Films 518 (2010) 1712-1715.
[16] A.A. Dakhel, Solar Energy 82 (2008) 513-519.
[17]A.A. Dakhel, Journal of Alloys and Compounds 475 (2009) 51-54.
[18]A.A. Dakhel, Current Applied Physics 11 (2011) 11-15.
[19]A.A. Dakhel, Optical Materials 31 (2009) 691-695.
[20]Robert Corriu, Nguyen Trong Anh, molecular chemistry of Sol-gel derived nanomaterials, Wiley Ed. ISBN 978-0-470-72117-9 (2009).
[21]Salih Kose, Ferhunde Atay, Vildan Bilgin, Idris Akyuz, International Journal of Hydrogen Energy 34 (2009) 5260-5266.
[22]A.A. Dakhel, Materials Chemistry and Physics117 (2009)284-287.
[23]R. Kumaravel, S. Menaka, S. Regina Mary Snega, K. Ramamurthi, K. Jeganathan, Materials Chemistry and Physics 122 (2010) 444-448.
[24] T.K. Subramanyam, S. Uthanna, B. Srinivasulu Naidu, Materials Letters 35, (1998), 214-220.
[25]T.P. Gujar, V.R. Shinde, Woo-Young Kim, Kwang-Deog Jung, C.D. Lokhande, Oh-Shim Joo, Applied Surface Science 254 (2008) 3813-3818.
[26]I. Akyuz, S. Kose, E. Ketenci, V. Bilgin, F. Atay, Journal of Alloys and Compounds 509 (2011) 1947-1952.
[27]D.M. Carballeda-Galicia, R. Castanedo-Pérez, O. Jiménez-Sandoval, S. Jiménez-Sandoval, G. Torres-Delgado, C.I. Zuniga-Romero, Thin Solid Films 371, (2000) 105-108.
[28]R. Legros, les semiconducteurs, Vol.1, Eyrolles Ed. (1974).

Journal of New Technology and Materials
JNTM
Vol. 01, N°00 (2011)29-32

OEB Univ. Publish. Co.

Photovoltaic applications of Light Beam Induced Current technique

Y. Sayad[a], A. Kaminski[b], D. Blanc[c], B. Bazer-Bachi[c] , M. Lemiti[c] and A. Nouiri[d]
(a) Institut des Sciences et Technologies, Centre Universitaire de Souk Ahras, Souk Ahras, 41000.
(b) IMEP-LAHC, Grenoble INP, Minatec, 3 rue Parvis Louis Néel - BP 257 – 38016 Grenoble Cedex 1, France
(c) Université de Lyon, Institut des Nanotechnologies de Lyon, INL-UMR5270, CNRS, INSA Lyon, 69621 Villeurbanne, France.
(d) Département de Physique, Faculté des Sciences, Université Larbi Ben M'hidi, Oum El-Bouaghi
Corresponding author: Tel. : +213.30.95.29.35 ; email : yassine.sayad@cu-soukahras.dz, say_phy@yahoo.fr
Received: 23 May 2011, accepted: 30 September 2011

Abstract:
Light or Laser beam induced current technique (LBIC) is conventionally used to measure minority charge carrier's diffusion length L_n by scanning a light spot away from collector (abrupt pn junction or Schottky contact). We show here the necessary precautions to be taken in order to apply this method on materials used in photovoltaics. We talk about SRLBIC or spectral response LBIC when this technique is combined with spectral reflectivity to allow determination of cells quantum efficiency. From internal quantum efficiency analysis, one deduces an effective carrier diffusion length, L_{eff}, including bulk and surface recombinations. LBIC is, also, often used to reveal electrically active extended defects such as grain boundaries and dislocations, and to check passivation efficiency of fabricated cells.
Key words: *LBIC, solar cells, crystalline silicon, diffusion length, extended defects, surface passivation.*

1. Introduction

Since the end of Second World War, the world economy has grown exponentially, which exploded its energy demands. To the head of energy sources coming fossil fuels (oil, gas and coal) which are non-renewable and causing greenhouse gases emissions, which pushed governments in industrialized countries to take decisions to encourage renewable energies sector. To the head of this sector comes photovoltaic industry.

In photovoltaic, crystalline silicon remains the most used material, and the global demand for this material has grown exponentially exceeds, since 2003, integrated circuit industry and the price of solar grade silicon increased from $20\$/kg$to $200\$/kg$ in short period. To face this shortage of silicon, the photovoltaic specialists tend to produce more and more thinner cells (currently cells with less than $180\mu m$theckness are commercialized) and to use less pure materials (compensated metallurgical grade silicon). Emergence of such thin and/or low quality materials has increased needs in characterization techniques.

In this paper, we focus on photovoltaic applications of LBIC technique. We begin with extraction of minority carrier's diffusion length by light spot scanning method in crystalline silicon used in photovoltaic. This method is known since 1980, but its application has not been, always, unmistakable on photovoltaic materials. We, also, see technique capabilities to detect extended defects (grain boundaries and dislocations), and to check passivation efficiency of cells.

2. Extraction of charge carrier's diffusion length in crystalline silicon wafers by light spot scanning method.

The method consists in scanning an laser beam away from collector and recording short circuit current at each point (Fig.1.). A collector structure may be Schottky contact or abrupt pn junction. We have chosen to make Schottky contacts by depositing a very thin (25 nanometers) and transparent Chromium layer, however, a pn junction collect better the photogenerated carriers. We should, also, passivate surface recombination centers before measurements.

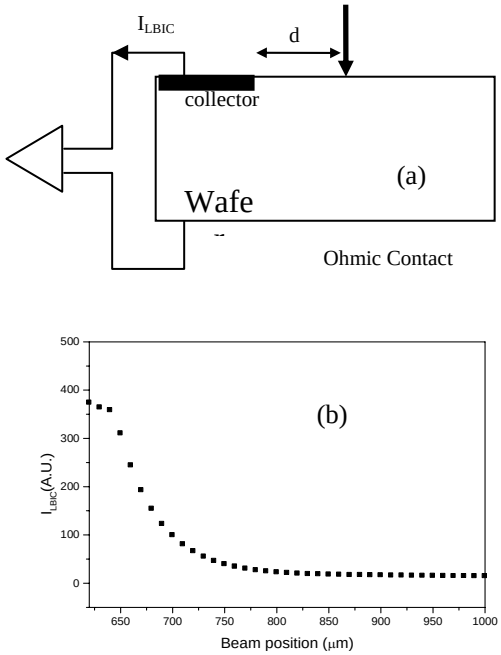

Fig. 1. Measurement structure of induced current (a) and a typical experimental profile obtained using p-Cz sample (b).

Our ISE TCAD simulations [1,2] showed that if silicon wafer hada thickness ofat least four times minority carrier diffus e on length, $\boldsymbol{w > 4L_D}$,
one obtain a photocurrent decay obeying to the following law,

$$I_{LBIC} \propto d^{-n} exp(-d/L_D) \quad (1)$$

Where n is between 0 and 1.5, L_D is bulk diffusion length.

Table 1 recapitulate measurement results of electrons diffusion length in a thick p type multicrystalline silicon sample (2.5mm) with resistivity of $0.5\,\Omega.cm$. The frontal surface is passivated by a hydrogen rich double dielectric layer SiOx/SiNy. Carrier collector is a Schottky contact formed by deposition of thin chromium layer, and measurements were performed in different grains.

Table. 1. Diffusion length in a thick p type silicon

n	L_D (µm)
0.34	58
1.33	70
0.43	190
1.02	419
0.59	395
1.03	520

In relatively thin wafers, where $w < 4L_D$, which is always the case of mono and multi crystalline silicon wafers used for fabrication of solar cells, where $L_D \sim w$, one obtain a simple exponential decay,

$$I_{LBIC} \propto exp(-d/L_{eff}) \quad (2)$$

Where, L_{eff} , is an effective diffusion length including bulk and surface recombination. Our simulations [1,2] shows that L_{eff} value becames very close to L_D for low recombination velocities of carriers at surfaces (fig. 2). Practically, one can reach carriers recombination velocities around $20\,cm.s^{-1}$ using silicon thermal oxide, SiO_2.

Figure 3 shows a photocurrent profile in semi-logarithmic scale, obtained on thin layer of p-type crystalline silicon (50 microns). This thin layer was epitaxially grown on a thick and highly doped CZ substrate, P+. The frontal surface was passivated in Hydrogenated silicon nitride SiNx:H. The collector is a Schottky contact obtained by deposition of thin Chromium layer.

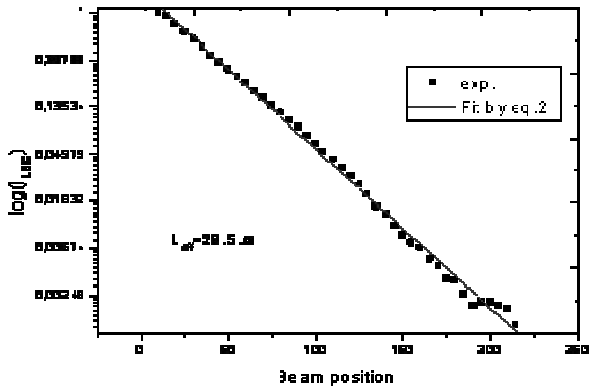

Fig.2. Extraction of diffusion length

3. Extraction of charge carriers diffusion length in finished cells.

In fabricated cells, one can deduce carrier's diffusion length from spectral analysis of cell internal quantum efficiency. In this case, one measure short circuit current $(I_{SC})$and reflectivity (R)at each wavelength, then, one deduce internal quantum efficiency using following relationship,

$$IQE(\lambda) = \frac{hc}{\lambda q P_{in}(\lambda)} \frac{I_{sc}(\lambda)}{(1-R(\lambda))} \quad (3)$$

$P_{in}(\lambda)$is incident beam power at wavelength λ .

In other hand, Basore [3] showed that in spectral domain$[800nm, 1000nm]$, the inverse the quantum efficiency is related to light absorption depth by following relationship,

$$IQE^{-1} = 1 + \frac{1}{L_{eff}}\left(\frac{1}{\alpha}\right) \quad (4a)$$

Where L_{eff} is an effective diffusion depends on bulk diffusion length L_D and electrons recombination velocity at cell rear surface, S.

$$L_{eff} = L_D \left[\frac{\frac{sr L_D}{D} + tanh\left(\frac{w}{L_D}\right)}{1 + \frac{sr L_D}{D} tanh\left(\frac{w}{L_D}\right)}\right] \quad (4b)$$

We note that effective diffusion length approaches the bulk diffusion length, $L_{eff} \sim L_D$, for $\frac{W}{L_D} > 1$.

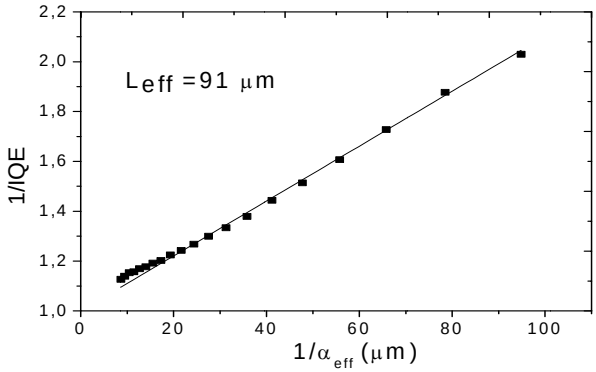

Fig. 3. Internal quantum efficiency inverse versus light penetration depth of commercial solar cell, effective diffusion length of $91\mu m$ is obtained by fitting to eq.3.

4. Highlighting extended defects in solar cells.

Extended defects such as grain boundaries and dislocations are preferential sites for segregation of impurities and points defects, and causes photocurrent loss in solar cells.

Figure 4 shows cartography of square areas $(1.5cm \times 1.5cm)$ of commercialized solar cell performed by 532nm laser diode (which corresponding to depth absorption of light of $1.3\mu m$) with scanning step of $50\mu m$. This cartography shows bright and dark grains, which corresponding a high and low carrier lifetime grains, respectively.

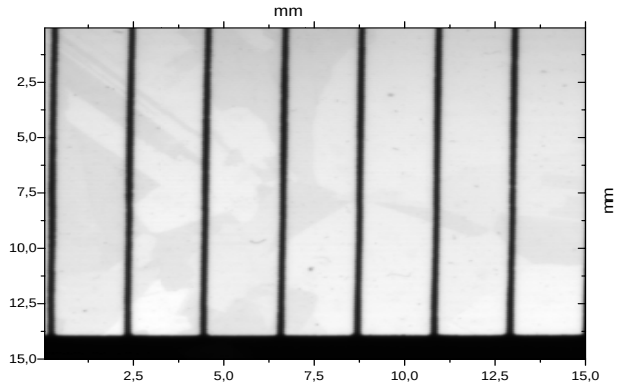

Fig. 4. LBIC cartography of a square surface $(1.5cm \times 1.5cm)$ performed by à 532nm laser $\left(\frac{1}{\alpha} = 1.3\mu m\right)$, with a scanning step of $50\mu m$.

LBIC profiles, like the showed one in figure 5, may be analyzed using analytical models [4-7] to extract minority carrier

recombination velocity at grain boundary.

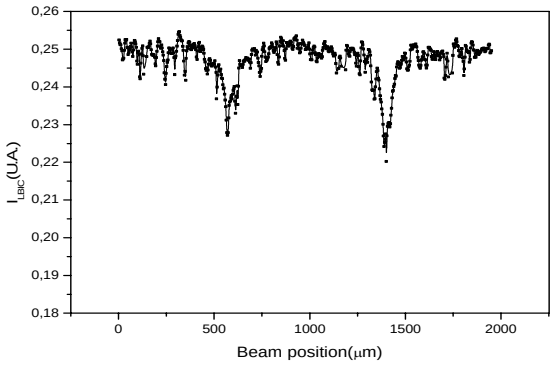

Fig.5. LBIC signal measured with 632nm laser in vicinity of two adjacent grain boundaries in silicon solar cell. Beam spot size at cell surface is about $6\mu m$.

31

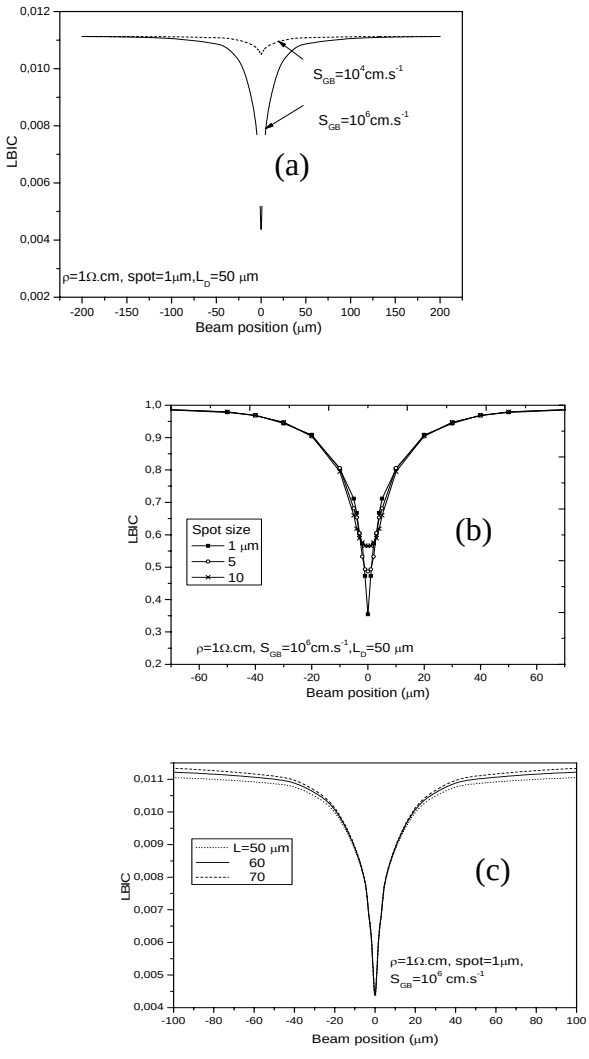

Fig.6. Simulated LBIC signal in vicinity of grain boundary. Impact of carrier recombination velocity (a), spot size (b) and diffusion length (c)

Figure 6 show ISE TCAD simulations of photocurrent at vicinity of grain boundary under different conditions of recombination velocity at grain boundary (a), spot size (b) and of carrier diffusion length (c).Dislocations may be origin of shorts in solar cells and, thus, decreases cell shunt resistance. Figure 7 shows cartography of a square area ($1cm \times 1cm$) of one solar cell, this cell have previously undergone a thermal annealing at 850°C of one hour duration before emitter diffusion step. The cartography shows formation of dislocations in high density.

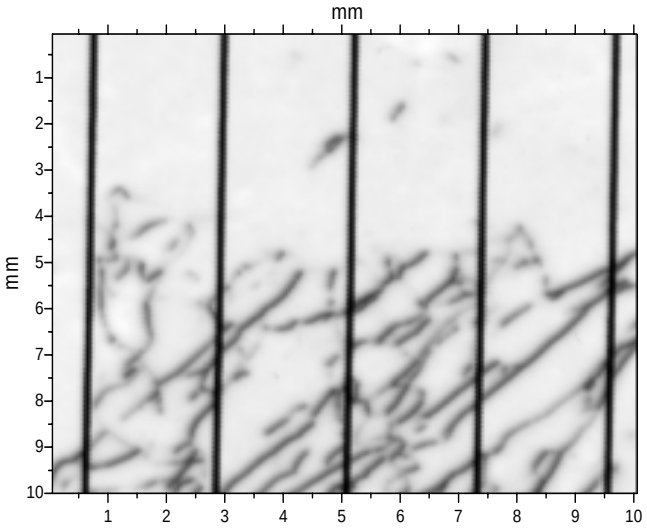

Fig. 7. LBIC cartography of square surface ($1cm \times 1cm$) performed by 980nm laser $\left(\frac{1}{\alpha} = 103\mu m\right)$, with step of $50\mu m$. Spot size at cell surface is $11\mu m$.

5. Displaying passivation efficiency.

Cartography of photocurrent may be used to compare passivation efficiency at different cell places. In figure 8, LBIC cartography of a solar cell measured by 980nm laser diode, the cell rear surface is passivated by triple dielectric layers (SiNx and SiOx). We remark a more photocurrent in areas passivated by dielectric layers than at localized grid of BSF (back surface field).

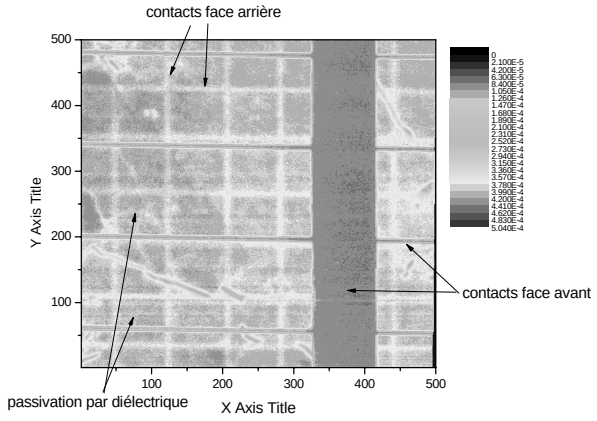

Fig.8. LBIC cartography of solar cell using 980nm laser diode, the cell rear surface is passivated by triple dielectric layers. Scanning step is 20 μm.

6. Conclusion

Using LBIC technique one can determine charge carriers diffusion length in silicon thin films and wafers, as well as in finished cells. This allows assessing possible degradation or improvement of starting material quality during cell process.

LBIC cartographies using different wavelengths allow probing cells from frontal to rear surfaces, to view electrically active defects and to evaluate passivation efficiency.

References :

[1] Y. Sayad, A. Kaminski, D. Blanc, A. Nouiri and M. Lemiti, Superlattices and Microstructures 45 (2009) 393-401

[2] PhD Thesis (online): *Détermination de la longueur de diffusion des porteurs minoritaires dans le silicium cristallin par interaction lumière-matière.*2009, INSA de Lyon.

[3] P.A. Basore, 23rd IEEE Photovoltaic Specialists Conference, 1993, p. 147-152.

[4] J. Marek, J. Appl. Phys., vol.55, Issue 2,1984, pp.318-326.

[5] J. D. Zook, Appl. Phys. Lett., vol. 42, Issue 7, 1983, pp.602-604.

[6] C. Donolato, J. Appl. Phys., vol. 54, Issue 3, 1983, pp.1314-1322.

[7] A. Mittiga and M. Capizzi, J. Appl. Phys., vol. 62, Issue 18, 1987, pp. 3443-3445.

Journal of New Technology and Materials
JNTM
Vol. 01, N°00 (2011)33-38

OEB Univ. Publish. Co.

Reflexion/ Transmission of a plane wave on a plane interface

F. Rahmi[a], H. Aklouche[a], N. Bedrici-Fraï[b,c], Ph. Gatignol[b], C. Potel[d]

[a] *Laboratoire Dynamique Des Moteurs et Vibroacoustique, Université M. B. de Boumerdès 35 000, Algérie.*

[b] *Laboratoire Roberval, UMR CNRS 6253, Université de Technologie de Compiègne, BP 20529, 60205 Compiègne Cedex, France.*

[c] *ESTACA, BP 76121, 53061 LAVAL Cedex 9, France.*

[d] *LAUM, UMR CNRS 6613, Université du Maine, 72 085 LE MANS Cedex 9, France.*

* Corresponding author : Tel : +213 774 65 75 44; Fax : + 213 24 91 30 99; Email : rahmifahim@gmail.com

Received: 23 May 2011, accepted: 30 September 2011

Abstract

On a plane interface between two elastic half-space, P and SV waves propagating in the (x,z) *pare related by Snell's law and the law of continuity of displacement components* u_x *and* u_z *and constraints* σ_{zz} *and* σ_{zx} *on both sides of the interface. An incident wave P or wave SV generates two P or SV reflected waves and two transmitted waves P or SV. The four continuity equations are written in the form of a matrix multiplied by a vector transmission-reflection coefficient, defined for potential movement of the particles. For an planar boundary between fluids with different characteristic impedances, there is continuity of* u_z *and* σ_{zz} *on both sides of the interface and the shear* σ_{zx} *in the medium must vanish at the interface (fluid media involving only perfect no viscosity, so that was normal stresses, not shear stress* $\sigma_{xz}=0$*). As soon as the angle of incidence exceeds a critical value of incidence, the wave for which the value of incidence is greater than* 30° *becomes evanescent. The reflection-transmission coefficients become complex.*

Keywords : *P waves, incidence, reflection, transmission.*

1. Introduction

The non destructive characterization of structures has grown considerably in recent years. The ultrasonic methods have become the preferred tool for non destructive evaluation of mechanical properties of materials [1]. They also have the advantage of being applicable to a wide range of materials. Surface waves were a long time the subject of extensive studies which had applications in both non-destructive tests in signal processing [1, 2]. Much research has been conducted on the interaction of such waves with surface discontinuities but most on the reflection and transmission. The elastic waves that result from moving particles propagate only in material media, so that electromagnetic waves propagate in a vacuum also. It was possible to address immediately the propagation of elastic waves in a fluid because this medium is a set of free particles; their properties are expressed using scalar parameters: density ρ, coefficient of compressibility χ, mean free path (average distance traveled by a particle between two collisions). The propagating waves are fully described by a scalar, pressure, or potential expansion of the displacement or velocity [1, 2, 3].

In summary, in a perfect fluid :

- The polarization of the wave, that is to say, the particle motion is necessarily longitudinal, parallel to its wave vector, the absence of viscosity preventing any shearing motion;
- The speed of propagation is expressed by $c=1/\sqrt{\rho\chi}$;
- The Poynting vector indicating the direction of energy propagation is parallel to the wave vector;
- The polarization of reflected and transmitted waves, on both sides of a surface separate two media of different impedances, and that of the incident wave. Their amplitudes and propagation directions are given by the Snell-Descartes in which only are involved the impedances of the media and the angle of the incident wave.
- The wave continues to propagate when the distance between a maximum and minimum pressure becomes the order of magnitude of the mean free path of particles.

2. Reflection / transmission at a plane interface

Consider the interface between two homogeneous fluids of different velocities (c_1 and c_2); when changing propagation environment, changing the characteristics of a plane wave is particularly interesting. The change in speed causes a specular reflection of the wave in the first medium (in a direction symmetrical to the normal at the point of incidence) and a refraction of the wave in the second medium at an angle given by famous law of Snell.

A progressive plane wave acoustic pressure $\widehat{p}_a$ which is of the form $\widehat{f}_1\left(t-\vec{n}_a.\vec{r}/c_1\right)$, maintained by a source located at infinity (for z tends to $-\infty$), propagates in a half-space fluid (density ρ_1 and speed c_1), bounded by a planar interface located at $z=0$, separating it from another half-space ρ_2 velocity of c_2) (Figure 1).

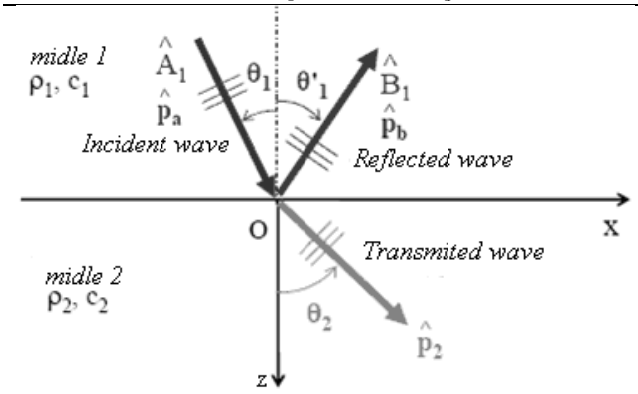

Figure 1. Reflection / transmission at the interface between fluids with different characteristic impedances.

The axes are chosen so that the direction of propagation of the incident wave is located in the plane (Oxz), and it makes an angle θ_1 with the axis (Oz) (obliquely incident). The interaction of the oblique incident plane wave with the interface generates a reflected wave in the middle F1 amplitude $\hat{B}_1$ (and direction of propagation making an angle θ_1' with the axis (Oz)), and a wave transmitted in the middle F2 amplitude $\hat{A}_2$ (and direction of propagation making an angle θ_2' with the axis (Oz)).

2. 1. Writing the problem in the middle F1

The propagation equation in the fluid medium is written F1

$$\left(\frac{\partial^2}{\partial x^2}+\frac{\partial^2}{\partial z^2}-\frac{1}{c_1^{\,2}}\frac{\partial^2}{\partial t^2}\right)\hat{P}_1(x,z;t)=0,\forall x,\forall z\le 0,\forall t \quad (1)$$

Conditions at the boundary (interface F1 / F2) $z=0$ (equal sound pressures normal and peculiar velocities in each medium) are written as follows:

$$\hat{p}_1(x,z;t)=\hat{p}_2(x,z;t),\ \forall x,z=0,\forall t \quad (2\text{-a})$$

$$\hat{\vec{v}}_1(x,z;t).\vec{n}=\hat{\vec{v}}_2(x,z;t).\vec{n},\ \forall x,z=0,\forall t \quad (2\text{-b})$$

Where $\vec{n}$ is the normal to the interface $(here\ \vec{n}=\vec{e}_z)$.

The projection on the normal $\vec{n}$ of Euler's equation outside sources in the medium F1 is written:

$$\rho_1\frac{\partial\hat{\vec{v}}_1}{\partial t}.\vec{n}+\frac{\partial\hat{p}_1}{\partial n}=0 \quad (3)$$

Because the projection operators on scalar $\vec{n}$ and $\partial/\partial t$ commute,

$$\rho_1\frac{\partial\left(\hat{\vec{v}}_1.\vec{n}\right)}{\partial t}+\frac{\partial\hat{p}_1}{\partial n}=0 \quad (4\text{-a})$$

Similarly, in the middle F2,

$$\rho_2\frac{\partial\left(\hat{\vec{v}}_2.\vec{n}\right)}{\partial t}+\frac{\partial\hat{p}_2}{\partial n}=0 \quad (4\text{-b})$$

By using equations (4), the boundary condition (2-b) can be written, equivalently

$$\frac{1}{\rho_1}\frac{\partial\hat{p}_1}{\partial n}(x,z;t)=\frac{1}{\rho_2}\frac{\partial\hat{p}_2}{\partial n}(x,z;t),\ \ \forall x,z=0,\forall t \quad (5\text{-a})$$

Or

$$\frac{1}{\rho_1}\frac{\partial\hat{p}_1}{\partial z}(x,z;t)=\frac{1}{\rho_2}\frac{\partial\hat{p}_2}{\partial z}(x,z;t),\ \ \forall x,z=0,\forall t \quad (5\text{-b})$$

The reflected wave propagates to infinity (note that this is not a condition of Sommerfeld for the existing field at infinity).

2. 2. Writing the problem in the middle F2

The propagation equation in the fluid medium is written as F2

$$\left(\frac{\partial^2}{\partial x^2}+\frac{\partial^2}{\partial z^2}-\frac{1}{c_2^{\,2}}\frac{\partial^2}{\partial t^2}\right)\hat{P}_2(x,z;t)=0,\forall x,\forall z\le 0,\forall t \quad (6)$$

The boundary conditions at the interface $z=0$ are identical to those written in §. 2. 1. The medium F2 containing neither source nor border other than at $z=0,$ write a condition of no return.

3. Solutions of the problem

The pressure field $\hat{p}_1$ in the middle F1 is the sum of the pressure field incident $\hat{p}_a$ and $\hat{p}_b$ reflected pressure field can be written as follows

$$\hat{p}_1(x,z;t)=\hat{p}_a(x,z;t)+\hat{p}_b(x,z;t)=\hat{f}_1\left(t-\frac{\vec{n}_a.\vec{r}}{c_1}\right)+\hat{g}_1\left(t-\frac{\vec{n}_b.\vec{r}}{c_1}\right) \quad (7)$$

And the field F2 is written in the middle

$$\hat{p}_2(x,z;t)=\hat{f}_2\left(t-\frac{\vec{n}_2.\vec{r}}{c_2}\right) \quad (8)$$

Where $\vec{n}_a,\vec{n}_b\ and\ \vec{n}_2$ denote the conditions of wave propagation incident, reflected and transmitted and $\vec{r}$ denotes the position vector $\overrightarrow{OM}=x\vec{e}_x+z\vec{e}_z$.

The condition (2-a) equal pressures $\hat{p}_1$ and $\hat{p}_2$ at the

interface $z = 0,$ whatever are the values of variables. Following the functions $\hat{f}_1, \hat{g}_1 \text{ and } \hat{f}_2$ which are identical, and their arguments :

$$t - \frac{\vec{n}_a.\vec{r}}{c_1} = t - \frac{\vec{n}_b.\vec{r}}{c_1} = t - \frac{\vec{n}_2.\vec{r}}{c_2}, \forall x, z = 0, \forall t \qquad (9\text{-a})$$

Or, noting $n_{xa}, n_{xb} \text{ and } n_{x2}$ the respective components on the axis (Ox) vectors $n_a, n_b \text{ and } n_2,$

$$\frac{n_{xa}x}{c_1} = \frac{n_{xb}x}{c_1} = \frac{n_{x2}x}{c_2}, \forall x, z = 0, \forall t \qquad (9\text{-b})$$

This implies

$$\frac{n_{xa}}{c_1} = \frac{n_{xb}}{c_1} = \frac{n_{x2}}{c_2} \qquad (9\text{-c})$$

By expressing the components $n_{xa}, n_{xb} \text{ and } n_{x2}$ according to angles $\theta_1, \theta_1' \text{ and } \theta_2,$ equations (9-c) are written

$$\frac{\sin\theta_1}{c_1} = \frac{\sin\theta_1'}{c_1} = \frac{\sin\theta_2}{c_2} \qquad (10)$$

As a result, since $\theta_1 \text{ and } \theta_1'$ are between 0 and $\pi/2,$

$$\theta_1 = \theta_1' \qquad (11)$$

They are reflecting equal angles of incidence and reflection. It should be noted firstly that the establishment of Snell's laws do not require the assumption of monochromatic wave, and secondly it is the conservation of the projection vector propagation directions on interface that involves laws of Snell, and not vice versa.

3. 1. Slowness surface

Slowness surface (L) is the location of the ends of the vector $\vec{m} = \vec{n}/C$ led to a fixed point *O*. Since $\vec{m} \text{ and } \vec{C}$ are collinear and $mC = 1,$, surface area and slow speeds to match in reverse pole *O* and power 1. Slowness surface, analogous to the surface of optical indices, plays an important role in the problems of reflection and refraction. The slow surface of a material own supplies for any direction, the solutions of the wave equation. Accordingly, since the vector of the incident wave is known, simply add the Snell's law to the surfaces of delays for the two materials without calculation, the vectors of the waves could propagate in the one another, their polarization and acoustic rays (that is to say, the direction of energy propagation).

In fluid medium, the speed is the same for any direction of propagation, the slow surface is a sphere and its intersection with the plane of incidence (Oxz) here is a circle.

Case $c_1 < c_2$:

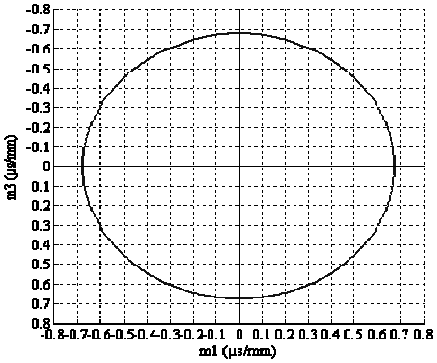

Figure 2. Slowness surface case $c_1 < c_2$.

Noting that each term of equation (10) corresponds to the projection on the *x*-axis vector slowness of the incident reflected and transmitted waves, using the intersection with the plane of incidence, surface delays of each of semi-infinite F1 and F2, can view, graphically some properties of waves propagating in each medium. It suffices to draw a line parallel to the axis Oz corresponding to the angle of incidence for θ_1 on the axis $Ox,$ the amount $\sin\theta_1/c_1$ (Figure 3. Where $c_1 < c_2$ so $1/c_1 > 1/c_2$). Delaying this amount to the right provides an intersection with each curve of slow circles F1 and F2 and consequently, yields the angles of reflection and transmission.

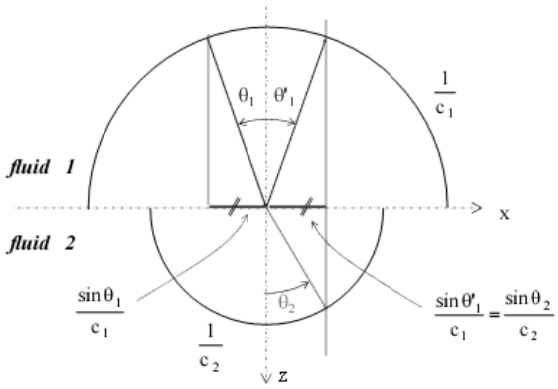

Figure 3. Using the intersection with the plane of incidence of the slowness surface of each semi-infinite medium [3].

3. 2. Harmonic solution

The source to infinity is monochromatic pulsation $\omega,$ a vector wave number associated with each plane wave pressure $\hat{p}_a, \hat{p}_b \text{ and } \hat{p}_2$ can be defined,

Are

$$\vec{k}_a = k_1\vec{n}_a = \frac{\omega}{c_1}\vec{n}_a \qquad (12\text{-a})$$

$$\vec{k}_b = k_1\vec{n}_b = \frac{\omega}{c_1}\vec{n}_b \qquad (12\text{-b})$$

$$\vec{k}_2 = k_2\vec{n}_2 = \frac{\omega}{c_2}\vec{n}_2 \qquad (12\text{-c})$$

And the use of a solution can be written

$$\left(\hat{p}_i(x,z;t) = \hat{A}_i \exp\left\{-i\left(\vec{k}_i.\overrightarrow{OM} - \omega t\right)\right\} \right)$$

$$\hat{p}_a(x,z;t) = \hat{A}_1 \exp\left\{-i\left(\vec{k}_a.\overrightarrow{OM} - \omega t\right)\right\} \quad (13\text{-a})$$

$$\hat{p}_b(x,z;t) = \hat{B}_1 \exp\left\{-i\left(\vec{k}_b.\overrightarrow{OM} - \omega t\right)\right\} \quad (13\text{-b})$$

And

$$\hat{p}_2(x,z;t) = \hat{A}_2 \exp\left\{-i\left(\vec{k}_2.\overrightarrow{OM} - \omega t\right)\right\} \quad (13\text{-c})$$

According to equations (9-c) written in paragraph (§ 3) that come from writing the boundary conditions at the interface $z = 0,$ written for all values of *x* and *t*, the projections on the interface (Ox) vector wave number $\vec{k}_a, \vec{k}_b \text{ and } \vec{k}_2$ are equal :

$$k_{xa} = k_{xb} = k_{x2} = k_x \quad (14)$$

The laws of Snell (10) and equal angles of incidence and reflection (11) who sell require, in the F1 environment, equality (at sign) projections on the axis (Oz) vector wave number $\vec{k}_a \text{ and } \vec{k}_b,$:

$$k_{za} = -k_{zb} = k_{z1} \quad (15)$$

In summary we write :

$$\vec{k}_a = k_x\vec{e}_x + k_{z1}\vec{e}_z \quad (16\text{-a})$$

$$\vec{k}_b = k_x\vec{e}_x - k_{z1}\vec{e}_z \quad (16\text{-b})$$

$$\vec{k}_2 = k_x\vec{e}_x + k_{z2}\vec{e}_z \quad (16\text{-c})$$

And

$$\overrightarrow{OM} = x\vec{e}_x + z\vec{e}_z \quad (16\text{-d})$$

The formula for the pressure field in the middle F1

$$\hat{p}_1(x,z;t) = \hat{p}_a(x,z;t) + \hat{p}_b(x,z;t) = \hat{A}_1 e^{-i(k_x x + k_{z1} z - \omega t)} + \hat{B}_1 e^{-i(k_x x - k_{z1} z - \omega t)} \quad (17)$$

And that F2 is in the middle

$$\hat{p}_2(x,z;t) = \hat{A}_2 e^{-i(k_x x + k_{z2} z - \omega t)} \quad (18)$$

Equality of pressures (2-a) $z = 0$ leads to

$$\hat{A}_1 e^{-i(k_x x - \omega t)} + \hat{B}_1 e^{-i(k_x x - \omega t)} = \hat{A}_2 e^{-i(k_x x - \omega t)}$$

Hence

$$\hat{A}_1 + \hat{B}_1 = \hat{A}_2 \quad (19\text{-a})$$

Or

$$-\hat{R}_p + \hat{T}_p = 1 \quad (19\text{-b})$$

$$\hat{R}_p = \hat{B}_1 / \hat{A}_1 \quad (20\text{-a})$$

$$\hat{T}_p = \hat{A}_2 / \hat{A}_1 \quad (20\text{-b})$$

Are the coefficients of reflection and transmission of pressure amplitude.

The partial derivatives with respect to z pressures can be written

$$\frac{\partial \hat{p}_1}{\partial z}(x,z;t) = ik_{z1}\left\{-\hat{A}_1 e^{-ik_{z1}z} + \hat{B}_1 e^{ik_{z1}z}\right\} e^{-i(k_x x - \omega t)} \quad (21\text{-a})$$

And

$$\frac{\partial \hat{p}_2}{\partial z}(x,z;t) = -ik_{z2}\hat{A}_1 e^{-ik_{z2}z} e^{-i(k_x x - \omega t)} \quad (21\text{-b})$$

Their report in the condition (4-b) equality normal speeds (4-b) $z = 0$ leads to

$$\frac{ik_{z1}}{\rho_1}\left(-\hat{A}_1 + \hat{B}_1\right) e^{-i(k_x x - \omega t)} = -\frac{ik_{z2}}{\rho_2}\hat{A}_2 e^{-i(k_x x - \omega t)}, \forall x, z = 0, \forall t$$

Or

$$\frac{k_{z1}}{\rho_1}\left(-\hat{A}_1 + \hat{B}_1\right) = -\frac{k_{z2}}{\rho_2}\hat{A}_2 \quad (22\text{-a})$$

Hence

$$\frac{k_{z1}}{\rho_1}\hat{R}_p + \frac{k_{z2}}{\rho_2}\hat{T}_p = \frac{k_{z1}}{\rho_1} \quad (22\text{-b})$$

Solving the system of two equations (19) and (22) with two unknowns $\hat{R}_p \text{ and } \hat{T}_p$ leads to

$$\hat{R}_p = \frac{-k_{z2}/\rho_2 + k_{z1}/\rho_1}{k_{z2}/\rho_2 + k_{z1}/\rho_1} \quad (23\text{-a})$$

And

$$\hat{T}_p = \frac{2k_{z1}/\rho_1}{k_{z2}/\rho_2 + k_{z1}/\rho_1} \quad (23\text{-b})$$

By replacing $k_{z1} \text{ and } k_{z2}$ by their respective expressions in terms of $k_1, \theta_1, k_2 \text{ and } \theta_2$

$$k_{z1} = k_1 \cos\theta_1 \quad (24\text{-a})$$

And

$$k_{z2} = k_2 \cos\theta_2 \quad (24\text{-b})$$

And introducing the characteristic impedances $Z_1 \text{ and } Z_2$ of the two media F1 and F2

$$Z_1 = \rho_1 c_1 \quad (25\text{-a})$$

And

$$Z_2 = \rho_2 c_2 \quad (25\text{-b})$$

The coefficients of reflection and transmission (23) can be written

$$\widehat{R}_p = \frac{-\cos\theta_2/Z_2 + \cos\theta_1/Z_1}{\cos\theta_2/Z_2 + \cos\theta_1/Z_1} \qquad (26\text{-a})$$

And

$$\widehat{T}_p = \frac{2\cos\theta_1/Z_1}{\cos\theta_2/Z_2 + \cos\theta_1/Z_1} \qquad (26\text{-b})$$

Or

$$\widehat{R}_p = \frac{Z_2/\cos\theta_2 - Z_1/\cos\theta_1}{Z_2/\cos\theta_2 + Z_1/\cos\theta_1} \qquad (27\text{-a})$$

And

$$\widehat{T}_p = \frac{2Z_2/\cos\theta_2}{Z_2/\cos\theta_2 + Z_1/\cos\theta_1} \qquad (27\text{-b})$$

Examples of changes in coefficients of reflection and transmission of pressure amplitude, depending on the angle of incidence are presented in the figures below. For an angle of incidence equal to 30° [1, 2, 3], a ''rupture'' appears in these curves. This angle is the critical angle for the interface considered above which the transmitted waves are evanescent.

3. 3. Evanescent waves

In the case where $c_1 > c_2$ and $\theta_1 > \theta_c$, the transmitted wave becomes evanescent : its amplitude decreases exponentially with a distance from the interface [1, 2, 3]. The total reflection phase shift accompanied χ by a reflection given by the argument of the complex reflection coefficient. The sum of the incident wave and the reflected wave produces a standing wave totally vertically and horizontally progressive.

4. Numerical results

Example 1 :

$\rho_1 = 2000\ Kg/m^3, c_1 = 750\ m/s, \rho_2 = 2500\ Kg/m^3, c_2 = 1500\ m/s$

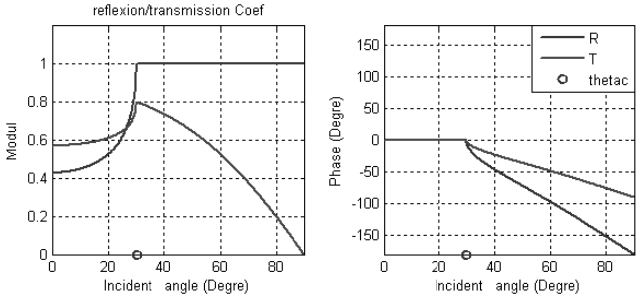

Figure 4. Magnitude and phase of the reflection and transmission coefficient for Example 1

Example 2 :

$\rho_1 = 3000\ Kg/m^3, c_1 = 750\ m/s, \rho_2 = 1000\ Kg/m^3, c_2 = 1500\ m/s$

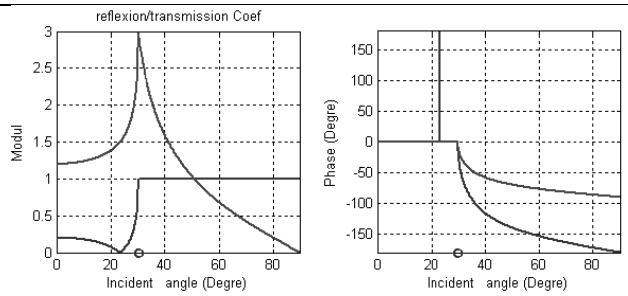

Figure 5. Magnitude and phase of the reflection and transmission coefficient for Example 2

.

Example 3 :

$\rho_1 = 1000\ Kg/m^3, c_1 = 750\ m/s, \rho_2 = 1000\ Kg/m^3, c_2 = 1500\ m/s$

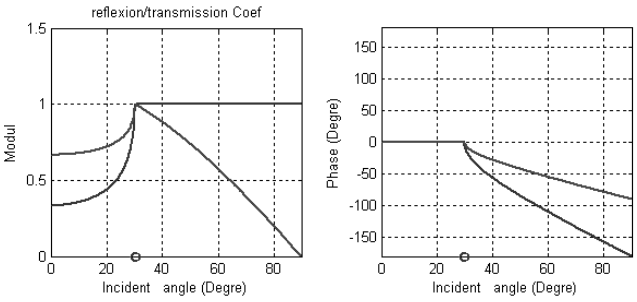

Figure 6. Magnitude and phase of the reflection and transmission coefficient for Example 3.

With :

R: Reflection coefficient;

T: Transmission coefficient;

Using the construction of Figure 3, it appears that from a certain angle of incidence noted θ_c and called critical angle for the interface F1/F2 considered (where $c_1 < c_2$) [1, 2, 3], there is no longer intersects the line parallel to Oz with the slow curve of the medium (Figure 7-a). Corresponding waves in the middle F2 are no longer propagating and become evanescent: they see their energy propagating in parallel to the interface whereas the pressure amplitude decreases exponentially in the direction of z increasing.

The value of the critical angle θ_c is given by : $\theta_c = \arcsin c_1/c_2$.

This corresponds to $\theta_{c2} = \pi/2$.

When $c_1 > c_2$, construction of Figure 7-c. shows that there is no critical angle on the interface considered.

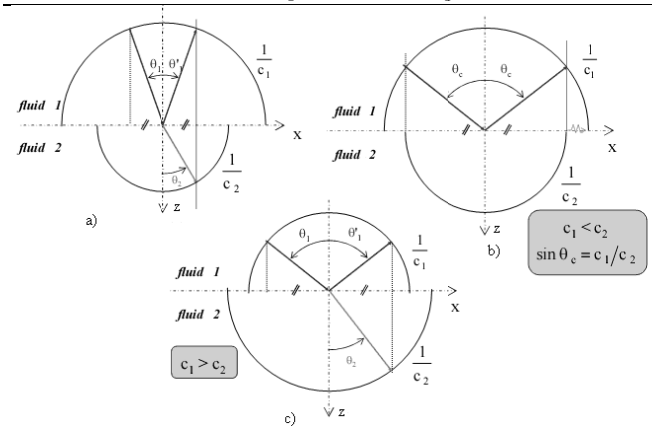

Figure 7. Intersection with the plane of incidence of the slowness surface for an interface F1/F2 –a) $c_1 < c_2$, –b) $c_1 < c_2$, – c) $c_1 > c_2$ [3].

4. 1. Discussion of results

In the ideal case where the interface is considered perfectly flat, while the second medium has characteristics different from those acoustic (ρ_1, c_1) and (ρ_2, c_2), a portion of the energy of the incident wave will be transmitted in the second medium. The consequence is that the reflected wave will be assigned a reflection coefficient of modulus less than or equal to **1** [1, 2, 3, 4, 5, 6]. If the reflecting medium has a velocity greater than that of the F1 community, we have seen that there exists a critical angle θ_c at which transmission is impossible, the modulus of the reflection coefficient is then equal to **1** [1, 2, 3 , 4, 5, 6] (the phenomenon of total reflection). At the critical angle the reflection coefficient decreases sharply with the angle, and when close to vertical it depends only on the characteristic impedances of two media. In the presence of damping in the second medium the phenomena will be slightly modified; in particular the coefficient of total reflection will be slightly less than 1. Finally, if the reflecting medium is impedance is very small or very large compared to that of the F1 community, the incident wave will reflect almost no energy loss, the reflection coefficient (the ratio of the amplitudes of waves reflected and incident) will equal **1** regardless of the angle [1, 2, 3].

The reflection coefficient of transmission of the pressure in the second medium, affecting the amplitude of the refracted wave is given by $T = 1 + R.$ The pressure level of the transmitted wave can exceed that of the incident wave. This result simply reflects greater continuity of pressure on both sides of the interface, and in no way violates the law of conservation of energy and can easily show that the intensity is equal to the sum reflected and transmitted intensities.

5. Conclusion

When the speeds of wave propagation in c_1 and c_2 circles F1 and F2 are such that $c_1 < c_2$, there is an angle of incidence θ_1 rated θ_c called critical angle for this interface from which the transmitted wave in the middle F2 becomes evanescent. The reflectance in the middle F1 becomes equal to **1** module (total reflection), but there is always the presence of acoustic energy in the medium F2. The evanescent transmitted wave propagates parallel to the interface, while its amplitude decreases exponentially with depth (when z increases), perpendicular to the interface.

References

[1] L. E. Kinsler, A. R. Frey, A. B. Coppens, J. V. Sanders, Fourth edition, John Wiley & Sons, Inc, New york. 548 pages, ISBN 0-471-84789-5.
[2] E. S. Krebes and P. F. Daley, Geophys. J. Int, 170, 205–216, 2007.
[3] C. Potel, M. Bruneau, Ed. Ellipse collection Technosup, 352 pages, 2006.
[4] C. Potel, J.F. De Belleval, J. of Applied Physics, 77, 12, 6152-6161, 1995.
[5] C. Potel, J.F. De Belleval, E. Genay, Ph. Gatignol, Acustica-Acta Acustica, 82, 5, 738-748, 1996.
[6] C. Potel, S. Devolder, A.U. Rehman, J.F. De Belleval, J.M. Gherbezza, O. Leroy, M. Wevers, J. Appl. Phys., 86, 2, 1128-1135, 1999.

Journal of New Technology and Materials
JNTM
Vol. 01, N°00 (2011)39-43

OEB Univ. Publish.Co.

Realization and study of ZnO thin films intended for optoelectronic applications

L. Herissi[(1)*], L. Hadjeris[(1)], H. Moualkia[(1)], N. Abdelmalek[(1)], N Attaf[(2)], M. S. Aida[(2)] and J. Bougdira[(3)]

[1] *LMSSEF, Université d'Oum El Bouaghi, 04000. Algérie*
[2] *LCMI, Université Mentouri, Constantine, 25000, Algérie*
[3] *Institute Jean Lamour UMR 7198, Department CP2S University of Nancy*
Corresponding author: Tel: +213773595986 Fax: +21332412419 Email: hlabidi12@gmail.com
Received: 23 May 2011, accepted: 30 September 2011

Abstract :

The objective of this study is the realization of zinc oxide (ZnO) thin films intended for optoelectronic applications. For this purpose, thin films were prepared by spray pyrolysis technique from zinc acetate solutions of different molarities (0.025 M, 0.05 M and 0.1 M) used as precursors on Si and glass substrates heated between 200 and 500 °C. The nozzle to substrate distance was varied between 20 and 30 cm. Structural, optical and electrical properties of the films have been studied. The results indicated that the films deposited were transparent in the visible region, well adherent to the substrates and presented surface roughness. All samples were polycrystalline in nature, having hexagonal würtzite type crystal structure. A (002) preferred orientation was observed at 450°C and a 0.025M molarity. The optical energy gap measured was about 3.3 eV. The refractive index values presented small variations with the deposition conditions and were located between 1.8 and 2.0. The electrical properties showed that the samples are natively n-type semiconductor and the electrical conductivity at room temperature varied between 10^{5} and 10^{8} $(\Omega.cm)^{-1}$.

Keywords :*thin films, semiconductor, band-gap, refractive index, electrical conductivity, optoelectronic.*

1. Introduction

Zinc oxide (ZnO), a II-VI type semiconductor with a large direct band gap of 3.4 eV, belongs to the family of transparent conducting oxides (TCO). It is a potential candidate for transparent front face electrodes on solar cells and flat panel displays owing to its electrical conductibility along with its high transparency [1-4]. Spray pyrolysis deposition (SPD), used here to prepare ZnO films, consists of spraying a Zn-containing precursor solution onto a heated substrate. The film forms as the solution's atomized aerosol droplets vaporize on the heated substrate leaving behind a dry precipitate for thermal decomposition. SPD has the advantages of set-up easiness vacuum-less, cost-effective, and flexibility over the plasma film deposition methods [5]. Large surface ZnO films can thus be deposited under atmospheric conditions on substrates from low-priced chemicals, while monitoring the preparation process step by step [6]. However, the physical and chemical properties of the films thus prepared depend on the process parameters such as the substrate temperature, the precursor concentration of the starting solution, the gas pressure, the solution flow rate, the deposition time and the nozzle-substrate distance [7-8]. The aim of this work is to study the structural, optical and electrical properties of ZnO thin films prepared by SPD under different substrate temperatures, precursor molarity values and spraying gun nozzle-substrate distances in order to optimize the deposition conditions yielding ZnO films with desired physical properties for particular applications. X-ray diffraction (XRD), transmittance measurements under UV-Visible, ellipsometry and electrical measurements were used to evaluate these properties. The evolution of the properties of the sprayed ZnO films is discussed and correlated to the deposition conditions.

2. Experimental Details

A. Sample preparation

The zinc oxide films were deposited by spraying a solution of zinc acetate dihydrate ($Zn(CH_3COO)_2$, $2H_2O$) dissolved in doubly distilled water onto silicon and glass substrates. The substrate temperature was varied between 200 and 500°C and measured via a Chromel–Alumel thermocouple. Precursor concentrations of 0.025M, 0.05M and 0.1M were used. The distance between the substrates and the spray gun nozzle was varied between 20 and 30 cm.

B. Sample Characterization

The structural properties of films were studied by X-ray diffraction, using Cu-K_α radiation of wavelength λ = 1.5405 Å. The size D of the crystallites was calculated from the Scherer's formula [9]. The thickness and the index of refraction were determined from ellipsometric measurements performed on ZnO films deposited onto Si substrates. The transmittance of the layers deposited on glass was measured in the UV-Visible region using a double beam spectrophotometer (Shimadzu 3101PC). The gap energy E_g of the ZnO films deposited on glass substrates was determined from their transmittance $T(\lambda)$. The absorption coefficient $\alpha(\lambda)$, in the spectral region of absorption of the light, was deduced from the Beer-Lambert law [10]. According to the Tauc's theory for the direct allowed transitions such as those occurring in the direct gap of ZnO, $\alpha(h\nu)$ close to the band edge is :

$$\alpha \cdot h\nu = A\sqrt{h\nu - E_g}$$

where A is a constant of proportionality and $h\nu$ is the energy of the incidental light photons. E_g can be estimated by extrapolating to the $h\nu$ - axis the linear part of the $(\alpha h\nu)^2$ -

curve. The limit of absorption below E_g can be described, empirically, by :

$$\alpha(h\nu) = \alpha_0 \exp\left(\frac{h\nu}{E_{Urb}}\right), \quad h\nu < E_g \qquad (2)$$

The E_{Urb} parameter was determined by the variation of $\log(\alpha)$ with $h\nu$. The electrical properties of the layers were determined using the $I(V)$ characteristics measured by the two points technique for a coplanar structure with two gold electrodes deposited by pulverization.

3. Results and Discussion

A. Structural Characterization

X-ray diffractograms of ZnO thin films deposited on glass at various substrate temperatures and a concentration of 0.05M are represented on figure 1. The films are polycrystalline, made of only one hexagonal phase of würtzite type. They show a maximum intensity for the peaks (100), (002) and (101). The (002) peak appears in all the diffractograms and its intensity increases with the temperature.

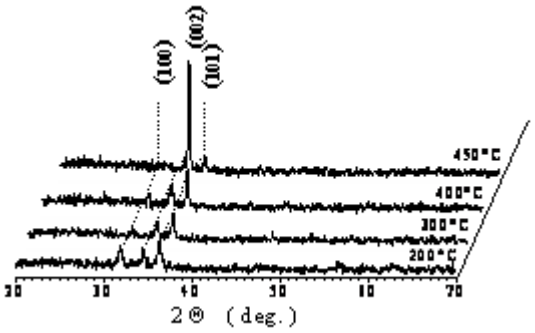

Fig. 1 XRD patterns of ZnO thin films with a molarity of 0.05M deposited by spray pyrolysis for various substrate temperatures.

The domination of this peak, at 450°C, indicates that the growth with the *c* axis perpendicular to the substrate is favored. This type of growth is especially important for piezoelectric applications. The orientations (100) and (101), corresponding to an *c* axis parallel to the surface, have as a basic plan formed of a mixture of zinc and oxygen atoms of equal numbers, which facilitate the arrangements between these atoms, and consequently requires less energy, and this explains their appearance at low temperature. The preferential orientation (002) is observed at 450°C. This result is critical for piezoelectric applications [11]. Krunks et al. have related this preferred orientation in sprayed films to the higher chemical purity of the layers grown at high substrate temperature. It was shown that the chemical purity of the films is controlled by the level of thermal decomposition of metalorganic complex compounds formed in the starting solutions [11-13].The variations of estimated grains size D with temperature are represented on figure 2. The size of the grains increases from 27 to 80 nm when the temperature of growth varies from 200 to 450°C. This evolution is normal because the increase in the temperature of deposition or treatment is always accompanied by an increase in the size of the grains whatever the technique of development used [14]. The samples deposited at high temperature grow more slowly, which is equivalent to an annealing of the layer in formation, involving an increase in the size of the grains. The results obtained here agree well with the works of Chopra and Roth et al. [15-17] that showed that the grains size increase with the films thickness.

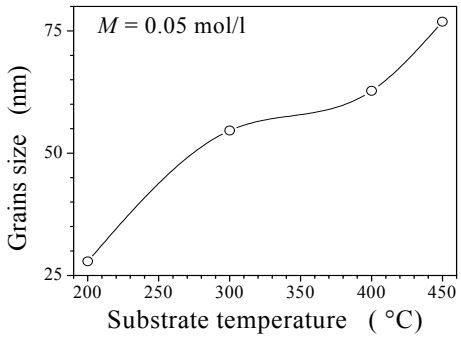

Fig. 2 Variation of the estimated grains size with the substrate temperature.

B. Optical Characterization

The transmittance spectra $T(\lambda)$ of ZnO films deposited on glass are shown on figures 3 and 4. Transmittance strongly depends on the temperature. As mentioned above, at low temperature, the reaction of decomposition of the droplets remains incomplete and the impurities are self incorporated in the material. Consequently, the mass deposited will be more important and, moreover, absorption will be stronger, which explains the low coefficient of transmission and its dependence on the wavelength in the visible region. On the other hand, at 450°C,

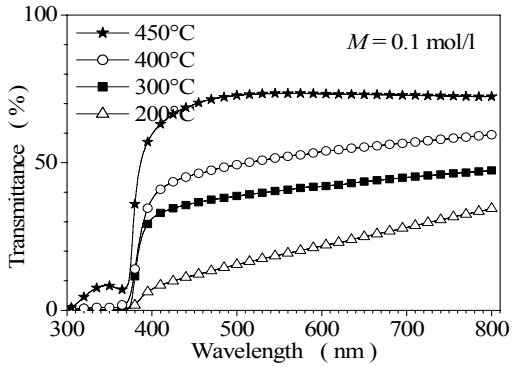

Fig. 3 Variation of the optical transmittance with the wavelength for different temperatures of deposition at 0.1M.

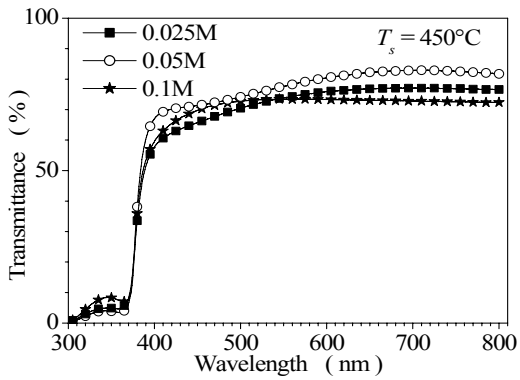

Fig. 4 Variation of the optical transmittance with the wavelength for different molarities at 450°C.

The transmittance is raised and depends slightly on the molarity. This indicates a complete thermal decomposition of the droplets involving the formation of a material close to the stoichiometry, which leads to layers of lower thicknesses. This is in good agreement with the results of Zaouk et al. who showed that at higher temperatures, there is enough energy available for the thermal decomposition, solvent evaporates before the droplets reach the substrate and only the solid precursor reaches the substrate where thermal decomposition occurs [11]. Consequently, the grown material is dense and the obtained films are relatively thin. Moreover the flat nature of the spectrum in the visible indicates that the material does not absorb in this region, which minimizes the thickness effect and thus the dependence on the molarity. That is also a consequence of the disappearance of the impurities following volatilization, at high temperature, of the secondary reaction products. The values found for the coefficient of transmission are about 70 to 85%, which gives the thin ZnO films the character of transparency in the visible region and makes this material a potential candidate for optoelectronic applications.

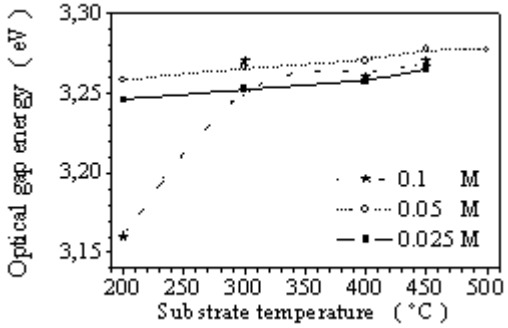

Fig. 5 Variation of the optical gap energy with the temperature of deposition for different molarities .

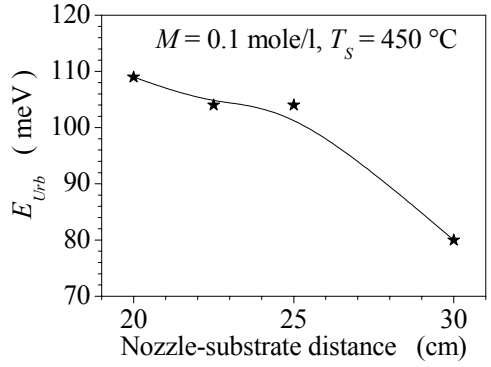

Fig. 6 Variation of the Urbach parameter with the nozzle-substrate distance.

The fundamental absorption region, due to the electronic inter-band transitions in ZnO films, is located in UV. According to (1), the value of the energy of the gap, E_g, is estimated by extrapolating to the $h\nu$-axis the linear part of the $(\alpha h\nu)^2$-curve. In figure 5, it can be seen that there is an influence of the conditions of deposition on the gap. In particular, this latter grows with the temperature. The energy of the forbidden band of our layers is approximately 3.3 eV which is lower than the value 3.37 eV of massive ZnO. Our results are in agreement with the work of Srikantand Lin et al. [18,19]. The increase in E_g can be correlated to the size of the grains which increases with temperature [14], this makes the value of E_g tend towards that of the massive ZnO. This point of view is similar to the observation of Ayouchi et al. [20], who had, on the contrary, obtained values of E_g higher than those of stoichiometric massive ZnO and thus observed a decrease of E_g with the temperature. This phenomenon was attributed to the reduced grains size in the thin layers of ZnO prepared by this technique and to the oxygen deficiency confirmed by XPS studies [20]. The low value obtained for the optical gap, for the film prepared with a molarity 0.1M at 200°C, is probably due to the incorporation of impurities and to structural defects which can be correlated with measurements of the refractive index. The low value obtained under these conditions indicates that the film is more porous than the others. From the variations of the refractive index with the deposition temperature, for various molarities, values situated between 1.7 and 2.0 are deduced, in agreement with the literature. The reduction of the refractive index with the raise of the concentration, observed, is compatible with the fact that the layer thickness increases with the molarity to the detriment of the density and, consequently, the drop of the index can be correlated to porosity.

It is possible to estimate the disorder existing in the layers by studying the variations of the absorption coefficient [20]. According to (2), the band tail width, E_{Urb}, is determined by the variations of $\log(\alpha)$ with $h\nu$ The values found for the Urbach energy are comparable with those found by other authors [21]. The decrease in E_{Urb}, by increasing the deposition temperature or, as can be seen in figure 6, the nozzle-substrate distance, indicates that, under these conditions, the structural disorder and the defects decrease. Indeed, increasing the distance between the substrate and the spraying nozzle makes the layer to be formed at a longer time and, when the temperature is raised enough, that is equivalent to annealing the layer being formed.

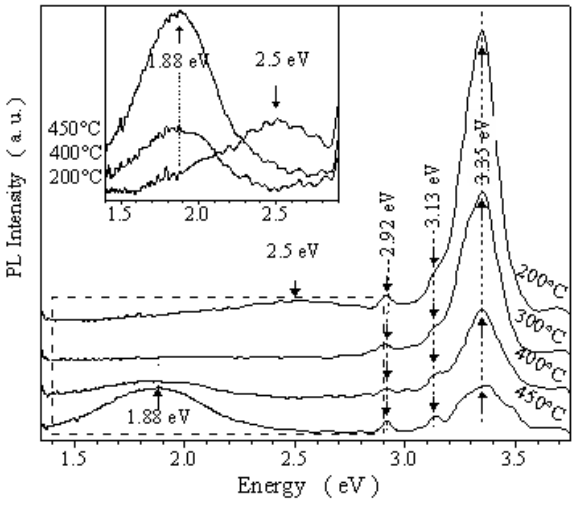

Fig.7. Photoluminescence spectra, at room temperature, of ZnO thin films deposited on Si substrates at different temperatures with a concentration of 0.025M. The inset is a magnification of low energy region (1.4-2.9 eV)

The photoluminescence (PL) was detected in all our ZnO samples and the shape of the spectra depends on the conditions of deposition (Fig. 7). In the ZnO film deposited at 200°C, a green luminescence band appears at about 2.5 eV (clearly seen in the inset of figure 7). It may be attributed to oxygen vacancies [22,23] due to an incomplete reaction when the film is deposited at low temperature. The green-yellow emission bands are usually assigned to one of the donor and acceptor mid-band-gap defect states such as oxygen vacancies, zinc interstitials, zinc vacancies, or antisite defects [24]. In the PL spectra of the samples deposited at 400 and 450°C the green luminescence band quenches and a red luminescence band appears at about 1.88 eV. The band is broad with a FWHM of about 0.5 eV. Its shape is Gaussian and the peak intensity increases with temperature. Even though the origin of red emission bands in ZnO remains an open question, this may be a result of an increase in the concentration of defects caused by oxygen interstitials [25-27]. Another peak seen for all films is located at 3.35 eV. Its intensity decreases with the deposition temperature. The bandgap of ZnO at room temperature found being about 3.3 eV, this suggests that this emission peak is excitonic in nature [28, 29].

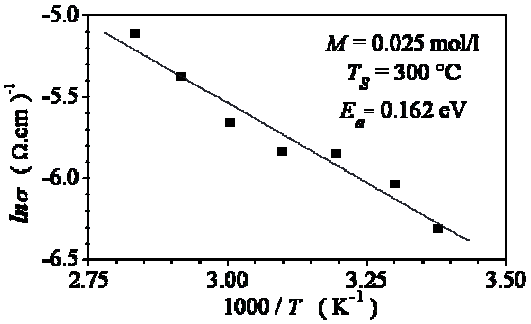

Fig. 8 Variation of the electrical conductivity of the ZnO thin layers with the heating temperature.

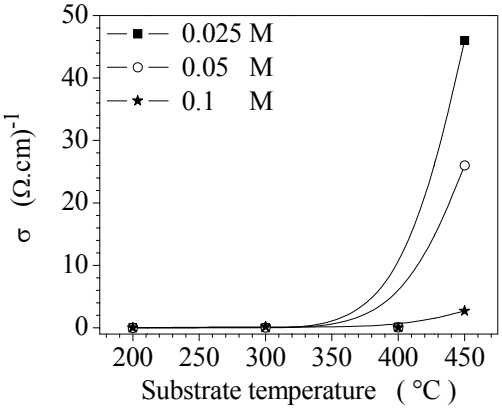

Fig. 9 Variations of the electrical conductivity with the temperature of deposition for various concentrations.

C. Electrical Characterization

The electrical properties of the ZnO thin layers are of a considerable interest, in particular in the photovoltaic applications. Fig. 8 represents the variation of the electric conductivity σ of the ZnO thin films with the heating temperature. It is expressed as a linear decrease of $log(\sigma)$ with the reverse of the temperature. The behaviour is characteristic of a semiconductor. Fig. 9 shows the variations of σ with the deposition temperature T_S for various concentrations. At low deposition temperatures the conductivity remains low. This can be correlated to the structure of the films. Indeed, XRD results indicated the presence, at low temperature, of grains of small size. As the grain boundaries reduce the mobility of the carriers and since the conductivity is proportional to this parameter, this explains the low values of the conductivity of the prepared samples at low temperature. However, by increasing the temperature of the substrate beyond 400°C, the quality of films improves and the increase in grains size justifies the raise of the conductivity.

The activation energy informs about the position of the Fermi level E_F relatively to the bottom of the conduction band E_C. It is deduced from the measurement of conductivity σ at various temperatures by using (3), k_B being the Boltzmann constant :

$$\sigma = \sigma_0 . \exp\left(\frac{-E_a}{k_B T}\right), \; E_a = E_C - E_F$$

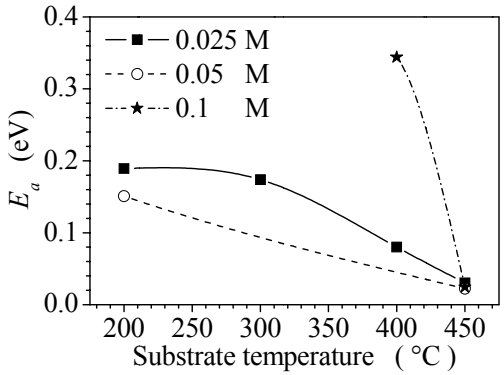

Fig. 10 Variation of the activation energy with the deposition temperature for different molarities.

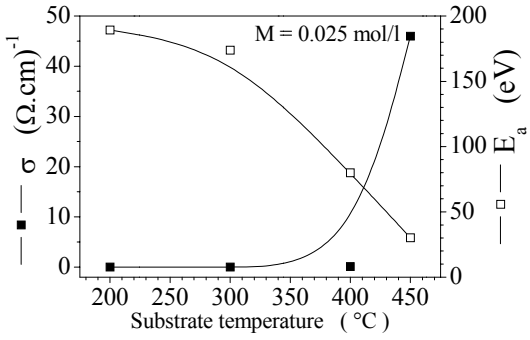

Fig. 11 Variation of the electric conductivity and the activation energy with the deposition temperature.

Fig. 10 shows variations of E_a with the deposition temperature for different concentrations of the starting solution. The maximum value of the activation energy found with our samples is about 0.35 eV. This value is lower than the half of the found energy gap which is about 3.3 eV. This indicates that the films are n-type semiconductors. This is in agreement with the literature since it is generally known that the ZnO thin layers are

natively n-type. In Fig. 11, it is shown that at given measurement temperature the conductivity increases when the activation energy decreases. This is in agreement with (3) and confirms, again, the semiconducting behavior of the deposited layers.

4. Conclusion

In this work, ZnO thin films were prepared by the spray pyrolysis technique under various experimental conditions. Thus, various substrates (glass and silicon), several temperatures of deposition (from 200 to 500°C), various concentrations of a zinc acetate solution (0.025M, 0.05M and 0.1M) and spraying gun nozzle-substrate distances varying from 20 to 30 cm were used. The deposits were carried out in air. Several series of samples were prepared and their structural, optical and electrical properties studied. The analysis of the results showed that the deposited films characteristics depend on the experimental conditions. The correlation with the properties of the layers made it possible to optimize the parameters of deposition that lead to semiconducting ZnO thin layers having a great transparency. This makes ZnO thin films a serious candidate in optoelectronic applications. The highly orientated films obtained at a temperature of 450°C and a molarity of 0.025M show that this simple technique can be effective in piezoelectric applications for the manufacture of cheap ultrasonic oscillators and transducers devices.

References

[l] S.A. Studenikin, NickolayGolego, and Michael Cocivera, Journal of Applied Physics Vol. 83 (4), (1998), 2104-2111.

[2] B.M. Ataev, W.V. Lundin, V.V. Mamedov, A.M. Bagamadova1 and E.E. Zavarin, J. Phys.: Condens. Matter 13 (2001) 211–214.

[3] A. Elhichou, A. Bougrine, J.L. Bubendorff, J. Ebothe, M. Addou, and M. Troyon Semicond. Sci. Technol. 17 (2002) 607 – 613.

[4] S.A. Studenikin, N. Golego, M. Cocivera, J. Appl. Phys., 84(4), (1998), 2287.

[5] F. Paraguay D and M. Miki-Yoshida, J. Morales, J. Solis, and W. Estrada L., Superficies y Vacío 9, (1999) 245-247. Sociedad Mexicana de Ciencia de Superficies y de Vacío.

[6] S. Roy and S. Basu, Bull. Mater. Sci., Vol. 25 (6) (2002), 513–515.

[7] W.T. Seeber, M.O. Abou-Helala, S. Bartha, D. Beila, T. HoÈchea, H.H. Afify, S.E. Demian, Materials Science in Semiconductor Processing 2 (1999), 45-55.

[8] B.J. Lokhande, M.D. Uplane, Applied Surface Science 167 (2000) 243–246.

[9] R. Ayouchi, D. Leinen, F. Martin, M. Gabas, E. Dalchiele, J.R. Ramos-Barrado, Thin Solid Films 426 (2003) 68-77.

[10] A. Bougrine, A. El Hichou, M. Addou, J. Ebothé, A. Kachouna, M. Troyon, Material Chemistry and Physics 80 (2003) 438-445.

[11] D. Zaouk, Y. Zaatar, R. Asmar, J. Jabbour, Microelectronics Journal 37 (2006) 1276–1279.

[12] M. Krunks, E. Mellikov, Thin Solid Films 270 (1995) 33-36.

[13] M. Krunks, E. Mellikov, E. Sork, Thin Solid Films 145 (1986) 105-109.

[14] A. Moustaghfir, Thèse de doctorat, Université Blaise Pascal, D.U. 1540 (2004).

[15] M.T. Mohammad, A.A. Hashim and M.H. Al-Maamory, Materials Chemistry and Physics 99 (2006) 382–387.

[16] K.L. Chopra, S. Major and D.K Panday, Thin Solid Films, 102 (1983)1-46.

[17] O.P. Rath, D.F. William, J. Appl. Phys. 52 (1981) 11.

[18] V.Srikant and D.R.Clarke, Journal of Applied Physics, 83 (10), (1998), 5447- 5451.

[19] S.S. Lin, J.-L. Huang, Surf. Coat.Technol., 185 (2004) 222.

[20] Ayouchi R., Martin F., Leinen D., Ramos-Barrado J.R., Journal of Crystal Growth, 247 (3) (2003), 497-504.

[21] V. Srikant et D. R. Clarke, J. App. Phys., 81 (1997) 6357.

[22] R.B. Lauer, J. Phys. Chem. Solids 34, (1973) 249-253.

[23] Y.G. Wang, S.P. Lau, X.H. Zhang, H.W. Lee, S.F. Yu, B.K. Tay, H.H. Hng, *Chemical Physics Letters* 375 (2003), 113-118.

[24] Ü. Özgür, Ya. I. Alivov, C. Liu, A. Teke, M. A. Reshchikov, S. Doğan, V. Avrutin, S.-J. Cho, and H. Morkoç, *Journal of Applied Physics* **98**, 041301, 2005.

[25] J. I. Pankove, "Optical Processes in Semiconductors" (Dover, New York, 1971).

[26] Yu.M. GerbshteinandYa.M. Zelikin, *Opt. Spectrosc.*28, 521, 1970.

[27] W. Lehmann, J. Electrochem. Soc. 115, 538 1968.

[28] M. Suscavage, M. Harris, D. Bliss, P. Yip, S.-Q. Wang, D. Schwall, L. Bouthillette, J.Bailey, M. Callahan, D. C. Look, D. C. Reynolds, R. L. Jones, and C. W. Litton, MRS Internet *J. Nitride Semicond. Res.* 4S1, G3.40 (1999).

[29] Ya. I. Alivov, E. V. Kalinina, A. E. Cherenkov, D. C. Look, B. M. Ataev, A. K. Omaev, M. V. Chukichev and D. M. Bagnall, *Applied Physics Letters*, 83 (23) (2003).

Journal of New Technology and Materials
JNTM
Vol. 01, N°00 (2011)44-46

OEB Univ. Publish. Co.

Substrate effect temperature on Cu_2ZnSnS_4 thin films deposited by ultrasonic technique

W. Daranfed[(1)], R. Fassi[(1)], A. Hafdallah[(1)], F. Ynineb[(1)], N. Attaf[(1)], M.S.Aida[(1)], L. Hadjeris[(1,2)], H. Rinnert[(3)] and J. Bougdira[(3)]

[(1)] *Laboratory of Thin films and Interface, Exact Faculty of Science, Department of Physics, University Mentouri of Constantine 25000 Algeria, e-mail: daranfadouarda@hotmail.com*

[(2)] *Laboratoire des Matériaux, et structures des Systèmes électromécaniques et leurs Fiabilité, University Larbi ben Mhidi OEB Algeria,*

[(3)] *Institute Jean Lamour UMR 7198, Department CP2S University of Nancy.*

Received: 23 May 2011, accepted: 30 September 2011

Abstract

Cu_2ZnSnS_4 (CZTS) thin films are a potential candidate for absorber layer in thin film solar cells. CZTS films were deposited by spray ultrasonic technique. An aqueous solution composed of copper chloride, zinc acetate, tin chloride and thiourea like precursors is sprayed on heated glass substrates at various temperatures. The substrate temperature was changed from 280°C to 360°C in order to investigate its influence on CZTS films properties. The DRX analyses indicated that Cu_2ZnSnS_4 films have nanocrystalline structure with (112) preferential orientation and a crystalline size, ranged from 30 to 50 nm with increasing substrate temperature. The obtained films are composed of SnS, ZnO, ZnS and Cu_2ZnSnS_4 phases. The optical films characterization was carried by the measurement of UV-visible transmission. The optical gap was deduced from the absorption spectra. Broad emissions at around 1.27 eV was observed in the photoluminescence spectrum measured at 77 K.

Keywords: *CZTS, photoluminescence, thin films, Transmission, spray technique, XRD.*

1. Introduction

Quaternary Cu_2ZnSnS_4 (CZTS), which consists of abundant materials, is one of the promising materials for absorber in thin films solar cell, due to its excellent properties, such as suitable band-gap energy of 1.4–1.5 eV, and large over $10^4 cm^{-1}$absorption coefficient [1]. Therefore, these properties make Cu_2ZnSnS_4 a potential material for photovoltaic applications. It is known that the electrical, optical, morphological and structural properties of this material are strongly influenced by the used deposition technique and by the related experimental parameters. Several techniques have been employed for preparing CZTS thin films: sputtering [1, 2], thermal evaporation [3], photo-chemical deposition [4].... Among these techniques, spray ultrasonic appears as an interesting technique for preparing Cu_2ZnSnS_4 thin films [5]. This technique is very attractive because it is inexpensive, easy and allows obtaining optically smooth, uniform and homogeneous layers. In this work, the effect of substrate temperature on both of the structure, chemical composition, optical and electrical properties of Cu_2ZnSnS_4 thin films, deposited by ultrasonic spray, has been investigated.

2. Experimental procedure

CZTS Thin films were deposited by spray ultrasonic in air. The initial solution is prepared from Copper chloride $CuCl_2$ (0.01M), zinc acetate (0.005M), tin chloride $SnCl_2$ (0.005M) and thiourea SC $(NH_2)_2$ (0.04M). These salts used as sources of different elements (Cu, Zn, Sn and S) are diluted in methanol. In order to optimize the temperature deposition, the substrate temperature was changed from T=280°C to 360°C with a step of 20°C and the spraying duration was fixed at 45min. The structural properties were determined by XRD using a Philips X' Pert system with CuK_α radiation (CuK_α =1.5418Å). The films morphology and composition were analyzed using a microscopic scanning SEM equipped with an EDX analysis system. The Optical transmissions in the UV-Visible range (300-2400nm) measurements were used with a Shimadzu UV-3101 PC spectrophotometer.

Finally, for photoluminescence the samples were excited by a 60 mW laser diode emitting at 488 nm. The PL signal was analyzed by a monochromator equipped with a 600 grooves/mm grating and by a photomultiplier tube cooled at 190 K. The spectral response of the detection system was precisely calibrated with a tungsten wire calibration source. For measurements at low temperature, the samples were inserted in a cryostat equipped with fused silica windows.

3. Results and discussion

3.1 Structural properties

The X-ray diffraction patterns of the CZTS thin films synthesized at various substrate temperatures are shown in figure 1. The diffraction angles vary from 20° to 60°. For all of the as-deposited films, peaks assigned to the (112), (200), (204) and (312) planes of CZTS are presents in the whole diffraction patterns. However, preferential (112) orientation was observed for all deposited films. Moreover, for higher substrate temperatures, one can clearly see the apparition of CZTS new peaks assigned by the (114) and (031) orientations [6].In addition, peaks of ZnS, ZnO and SnS related to the secondary phases are seen in figure 1.The individual crystalline size (D) in the films has been determined from (112) peak by using the Scherrer's formula [7].

$$D = \frac{K\ \lambda}{\beta\ \cos\ \theta}$$

Where K is the Scherrer constant value corresponding to the quality factor of the apparatus measured with a

reference single crystal, λ is the wavelength of the X-ray used; β is the full width at half maximum of the peak and θ is the Bragg angle. The crystalline size in films of different thicknesses is of the order 30-50 Å and is in good agreement with the reported values [8].

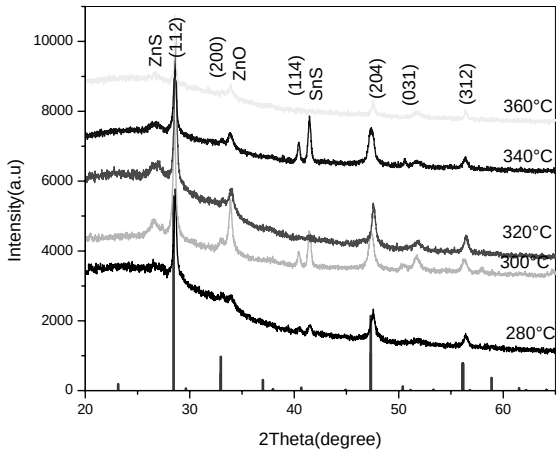

Figure 1: XRD patterns of CZTS films deposited by the spray ultrasonic at different substrate temperature.

3.2 Optical properties

Optical properties of the deposited Cu_2ZnSnS_4 films are studied by the analysis of the spectroscopic optical transmittance in the visible range. In figure 2 is reported the transmittance spectra of films deposited with various substrate temperatures. From the solid band theory, the relation between the absorption coefficient α and the energy of the incident light (hν) is given by:

$$(\alpha h\nu)^n = B\,(h\nu - E_g)$$

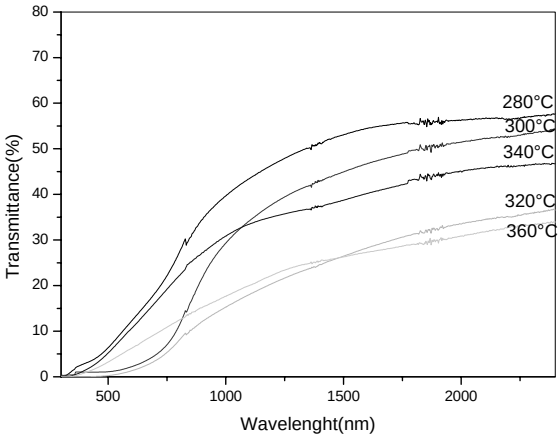

Figure 2: Optical transmission spectra of CZTS thin films prepared at various substrate temperatures.

Where B is a constant, E_g the band gap energy and n=2 or 1/2 for crystalline (direct transition) or amorphous CZTS, respectively.

The variation of the deduced optical gap of films with substrate temperature is reported in figure 3, as seen, at substrate temperature of 280°C, 300°C and 320°C the values of optical gap are 1.6 eV, 1.5eV and 1.45 eV respectively. These values are in good agreement with Cu_2ZnSnS_4 band gap values reported by other authors [9, 10]. Higher substrate temperatures 340°C and 360°C yielded to 1.8 eV and 1.76 eV optical gaps.

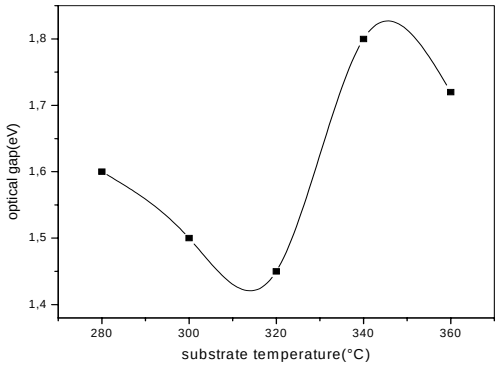

Figure 3: Variation of the optical gap as a function of the substrate temperature

The increase in optical gap with increasing substrate temperature can be due to improvement in the films crystallinity as shown in figure 1. Such a band gap shift can be related to the formation of different Zn-content according to the DRX diffractograms and EDX (Zn-riche, Cu-poor) analysis. The incorporation of ZnS (with gap above 3.5 eV) has resulted in a large shift of the band gap of other materials such as $CuInS_2$ [11]. In another work, Torodov and al [12] fabricated CZTS thin films by soft-chemistry method and they reported that the optical gap vary from 1.33 to 1.86 eV where the films are Zn-riche and Cu-poor.

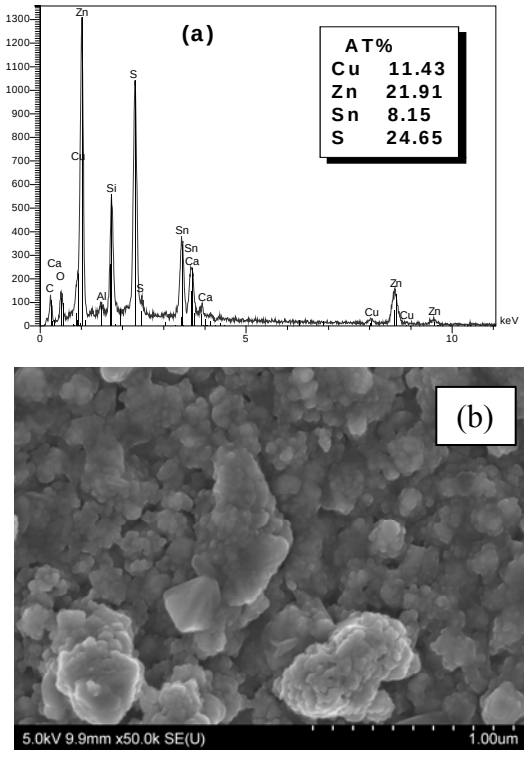

Figure 4: (a), EDX characterizations of as-synthesized CZTS thin films.
(b), Surface morphology images by SEM observation.

3.3 Morphological and composition

As shown in figure 4(a) the elemental composition of Cu_2ZnSnS_4 of thin films deposited at 360°C of substrate temperatures is determined from EDS analysis. From this analysis we conclude that CZTS films are Zn-rich, Cu-poor and sulphur deficient. Sulphur deficiency is significantly higher with increasing substrate temperatures; this is due to the sulphur volatility. Sundra et al [8] have also noticed the sulfur deficiency in CZTS thin films prepared by RF magnetron sputtering. Spray-deposited CZTS films obtained from pure aqueous solution by Nakayama et al [13] in the substrate temperature range 553–633K are also sulphur-deficient (28–38 at %). Previous works suggests that a slightly Zn-rich and Cu-poor composition gives good optoelectronic properties [14, 15, 9].

Figure 4(b) presents the surface morphology images by SEM observation at substrate temperature 360°C. It can be seen from the figure that the films consist of compact structure grains with sub-micron size. Our film had larger and more densely packed grains than that reported in Ref. [16]. It is well known that the efficiency of polycrystalline solar cells increases with increasing grain size in the absorber layer, hence larger grains are required for the fabrication of high efficiency solar cells [16, 17].

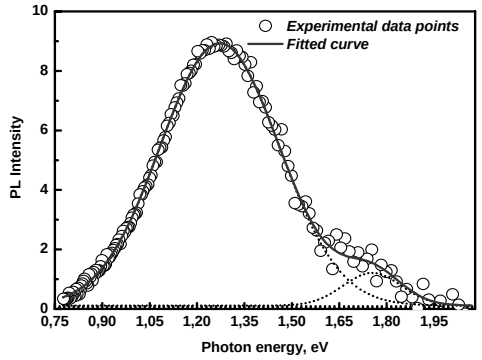

Figure 5: PL spectra of the CZTS thin films grown at substrate temperatures of 320°C.

3.4 Photoluminescence

Figure 5 shows the photoluminescence spectrum of the CZTS film at 320 °C measured at 77 K. As seen, a large peak of emission localized at 1.27 eV was observed. This later peak was observed by several authors [17. 18.19] which is intense and perfectly symmetrical. However, the same authors have noted also the dissymmetry in this peak of emission.

4. Conclusion

Cu_2ZnSnS_4 thin films have been successfully deposited by spray ultrasonic technique. The effect of substrate temperature on the growth of spray-deposited Cu_2ZnSnS_4 thin films was investigated. In conclusion, kesterite structured CZTS with satisfactory nearly stoichiometry and the crystalline sizes in the range 30–50 nm were obtained. The band gap of the obtained CZTS films was ranged from 1.45 to 1.8 eV indicating that the deposited film at 320°C has suitable optical properties for efficient solar energy conversion.

References

[1] K. Ito, T. Nakazawa, Jpn. J. Appl. Phys, Vol. 27, 1988, pp. 2094.
[2] J.S. Seol, S.Y. Lee, J.C. Lee, H.D. Nam, Sol. Energy Mater. Sol. Cells 75, vol. 155, 2003, pp. 1978.
[3] T.M. Friedlmeier, N. Wieser, T. Walter, H. Dittrich, in Proceedings of the 14th European Conference of Photovoltaic Science and Engineering and Exhibition, Belford, 1997, pp. 1242.
[4] K. Moriya, K. Tanaka, H. Uchiki, Jpn. J. Appl. Phys. Vol. 44, (2005), pp. 715.
[5] A. Ashour, H. Afif, S.A. Mahmoud, Thin Solid Films. Vol. 263, 1995, pp. 248.
[6] N. Kamoun, H. Bouzouita, B. Rezig, Thin Solid Films, vol. 515, 2007, pp. 5949–5952.
[7] C. M. Lampert, Sol. Energy. Mater, 1981, pp. 6- 11.
[8] Y.B. Kishore Kumar, G. Suresh Babu, P. Uday Bhaskar, V. Sundara Raja, Solar Energy Materials & Solar Cells, vol. 93, 2009 pp. 1230–1237.
[9] H. Katagiri, Thin Solid Films, vol. 426, 2005, pp. 480–481.
[10] N. Nakayama, K. Ito, Applied Surface Science, vol. 92, 1996, pp. 171.
[11] S. Schorr, V. Riede, D. Spemann, Journal of Alloys and Compounds, vol. 414, 2006, pp. 26–30.
[12] T. Todorov, M. Kita, J. Carda, P. Escribano, Thin Solid Films, vol. 517, 2009, pp. 2541–2544.
[13] N. Nakayama, K. Ito, «Sprayed films of stannite Cu_2ZnSnS_4», Appl. Surf. Sci, vol. 92, 1996, pp. 171–175.
[14] Jonathan, J.Scragg, Phillip J. Dale, Laurence M. Peter, Electrochemistry Communications, vol. 10, 2008, pp. 639–6423.
[15] T. Kobayashi, K. Jimbo, K. Tsuchida, S. Shinoda, T. Oyanagi, Appl. Phys, vol. 44, 2005, pp. 783.
[16] J. Seol, S. Lee, J. Lee, H. Nam, K. Kim, Sol. EnergyMater. Sol. Cells, vol. 75, 2003 pp. 155.
[17] T. Tanaka, D. Kawasaki, M. Nishio, Q. Guo, Phys. Stat. Sol, vol. 3, 2006, pp. 2844.
[18] K. Tanaka, Y. Miyamoto, H. Uchiki, K. Nakazawa, Phys. Status Solidi, vol. 203,2006,pp.2891.
[19] Y. Miyamoto, K. Tanaka, M. Onuki, Journal of Applied Physics, Vol. 47, 2008, pp. 596–597.

Journal of New Technology and Materials
JNTM
Vol. 01, N°00 (2011)47-50

OEB Univ. Publish. Co.

Investigation on chemical bath deposited CdS thin films

H. Moualkia [1,*], N. Attaf [2], L. Hadjeris [1], L. Herissi [1], N. Abdelmalek[1]

[1] *Laboratoire des Matériaux et Structure des Systèmes Electromécaniques et leur Fiabilité, Faculté des Sciences et de la Technologie, Université Larbi Ben M'Hidi, Oum El Bouaghi, Algérie*

[2] *Laboratoire de Couches Minces et Interfaces, Faculté des sciences, Université Mentouri, Constantine, Algérie.*

[*] *Corresponding author: moua_lkia@ yahoo.fr*

Received: 23 May 2011, accepted: 30 September 2011

Abstract

This paper presents the effect of solution temperature on optical, electrical and photoconducting properties of CdS films prepared by chemical deposition method. The solution temperatures used varied between 55 and 75 °C. X-ray diffraction analysis showed that the prepared films have an hexagonal structure with (002) reflection. The transmittance data analysis showed a high transmission coefficient in visible range (85%) and an optical band gap lying between 2 and 2.4 eV. Scanning electron microscopy (SEM) and electrical measurements showed a pronounced effect of the solution temperature on thickness, dark conductivity and photoconductivity to dark conductivity ratio ($\sigma_{phot}/\sigma_{dark}$) parameters. The evolution of such parameters as a function of temperature are presented and discussed. It was found that the ($\sigma_{phot}/\sigma_{dark}$) ratio reaches high values of the order of 10^4 and 10^3 at 55 and 65 °C, respectively. These results indicate that CdS thin films prepared at these temperatures are convenient for optoelectronic and photovoltaic applications.

Keyswords*: CdS thin films, Chemical bath deposition (CBD), Physical properties, Solar cell.*

1. Introduction

Nowadays, the fabrication of high efficiency solar cells based on CdS/CdTe, CdS/$CuInSe_2$ and CdS/$CuIn(Ga)Se_2$ thin films heterostructure [1-4] has increased the studies on this technologically relevant semiconductor material. The chemical bath deposition (CBD) of thin films is the most widely employed method [5] for fabricating n-type window layers on $CuIn(Ga)Se_2$, $CuInSe_2$ and CdTe solar cells [6-9]. Several studies reported in the literature showed the role of the chemically deposited CdS films window layer on solar cells efficiency [2, 3, 10]. For this purpose several properties are required for the CdS thin films such as: (i) relatively high transparency and wide band gap (ii) relatively large conductivity to reduce the electrical solar cells losses and higher photoconductivity to not alter the solar cell spectral response. However, the production of CdS films still requires further investigation. In the present work, CdS thin films were grown by chemical bath deposition method. Optical, electrical and photoconducting properties have been investigated as a function of bath temperature in order to study their growth mechanism and achieve highly transparent, conductive and photoconductive layers.

2. Experimental

The CdS thin films were deposited on glass substrates from a chemical bath containing deionised water, cadmium acetate $Cd(CH_3COO)_2 2H_2O$ ($5\ 10^{-3}$ M), Thiourea $SC(NH_2)_2$ ($2\ 10^{-2}$ M) and ammonia NH_4OH (2M). Cadmium acetate and thiourea were employed as cadmium and sulphur sources, respectively. The substrates were cleaned ultrasonically in acetone and methanol, rinsed in distilled water and dried in hot air. After drying, the samples were inserted vertically into the chemical bath. The solution temperatures were varied from 55 to 75°C. The deposition time was 60 min for each film.

After elaboration, films thicknesses were determined from profilometry measurements. The surface morphology of the films was analysed by scanning electron microscopy (SEM). The structural characterization was carried out by the X-ray diffraction (XRD) technique using an X-ray diffractometer (Philips X'Pert) with CuKα radiation. The transmittance of the films was studied using a Shimadzu 3101 PC UV-visible spectrophotometer. The electrical conductivity and the photoconductivity of the films were measured in a coplanar structure obtained by evaporation of two golden strips on the film surface. For the photoconductivity measurements, the samples were illuminated by unfiltered white light from a halogen lamp; the light intensity was 3000 Lx.

3. Results and discussion

3.1 Structure and morphology

The SEM images of CdS films deposited at the solution temperatures: (a) Ts = 60°C and (b) Ts = 65°C are shown in Figure 1. The images display homogeneous and continuous thin layers with small crystallites. These thin layers are originated from heterogeneous reaction via the ion by ion mechanism as has been reported in previous works [11, 12].
Figure 2 shows XRD pattern of CdS thin film deposited at Ts = 60°C. It shows only one line that corresponds to the (002) reflection of the hexagonal structure in accordance with earlier findings where several authors have observed that the preferential orientation of the CdS thin films is along the (002) direction [13-15]. It is also interesting to note that CdS thin film with hexagonal structure is highly favourable for solar cell applications as a window layer due to its stability [16].
The variation of the thickness of CdS thin films as a function of the solution temperature is presented in Figure 3. It is clear from the figure that the thickness increases with increasing temperature up to 65 °C, then decreases at higher

solution temperature (T_s > 65 °C). This latter behaviour can be interpreted as follows:

(i) In the temperature range ($T_s \leq 65$°C), the thickness increase is attributed to the increase of the releasing rate of the Cd^{+2} and S^{-2} ions which nucleate on the substrate to form CdS particles. Moreover, in accordance with SEM analysis, the CdS thin film grow with an ion by ion mechanism and it is known that the ion by ion mechanism yields films with larger thickness [17].

(ii) At higher temperature (Ts > 65°C) the releasing rate of Cd^{+2} and S^{-2} ions become too high because of the thermal effect. Hence, the deposition mechanism changes into cluster by cluster which needs higher temperatures to occur as shown in our previous work [18].

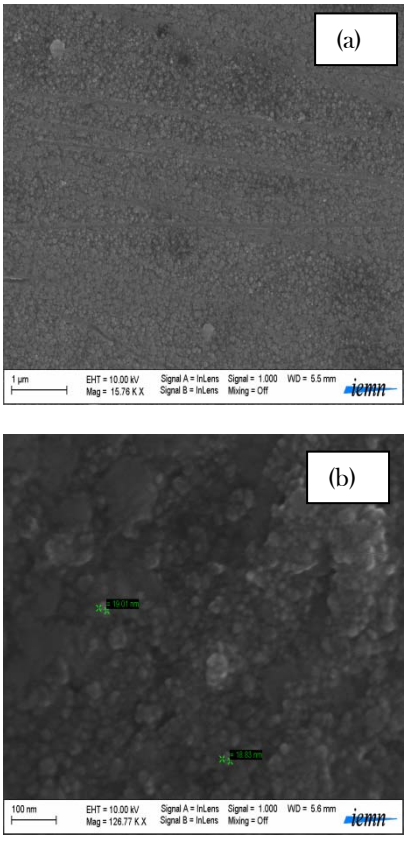

Figure 1: SEM micrograph of CdS sample deposited at the solution temperatures (a) Ts = 60°C, (b) Ts = 65°C

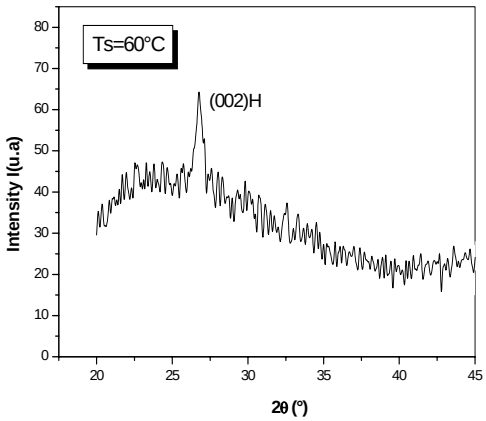

Figure 2: X-Ray spectrum of a typical CBD-CdS sample deposited at the solution temperature Ts= 60°C

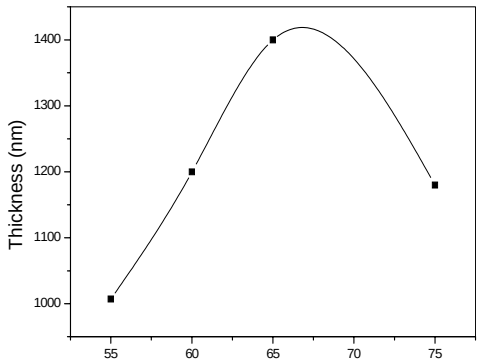

Figure 3: Evolution of CdS thickness with the solution temperature

In this deposition process conditions, CdS can take place by both heterogeneous and homogeneous reactions leading to the formation of continuous CdS film at the surface of the substrate and to the formation of large CdS particle (Clusters) in the bulk of the solution, respectively. The heterogeneous reaction competes with the homogeneous one, which depletes the reactants to form CdS particles in the bulk solution resulting in a decrease of the thickness.

3.2. Optical properties

Figure 4 shows the optical transmittance of CdS thin films deposited at various solution temperatures. All films exhibit optical transmittance more than 60 % for wavelengths larger than 500 nm, which is one of the prerequisites for solar cells window layer [19]. We note a sharp absorption edge in the range of 400 - 440 nm [20, 21]. The transmittance in the low wavelength region extends to 300 nm. This means that there are disorder effects or presence of amorphous components in the film [21].

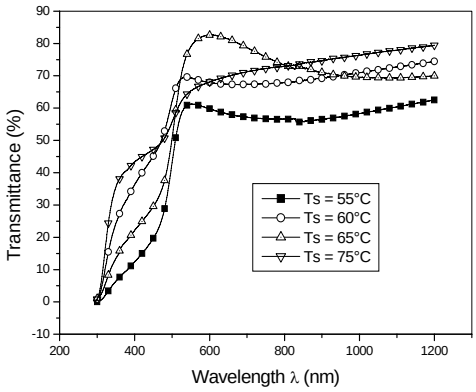

Figure 4: Influence of solution temperature on the optical transmittance of CdS films

The absorption coefficient α of CdS thin films was calculated from the transmittance spectra using the beer-Lambert approximation. The absorption coefficient α can be expressed by Urbach relation:

$$\alpha = \frac{A(h\upsilon - Eg)^n}{h\upsilon} \qquad (1)$$

Where A is a constant, Eg is the energy band gap, υ is the frequency of the incident radiation and h is Plank's constant. The exponent n is 0.5 for direct allowed transitions. CdS is a direct band gap material; several workers reported this type of transition [22-24]. The energy band gap of the films at various temperatures have been determined by extrapolating the linear portion of the plots of $(\alpha h\upsilon)^2$ versus $h\upsilon$ to the energy axis. The band tail width E_u (the so-called Urbach energy) was deduced from the slope of the graph $Ln(\alpha) = f(h\upsilon)$. The band gap and the band tail width E_u for different solution temperatures are given in table 1. The same band gap values (Eg = 2- 2, 4 eV) were reported by A. Ates et al. [25].

Table 1: Optical parameters of CdS thin films for different solution temperatures

Samples	Solution temperatures (°C)	Band gap (eV)	Urbach's energy E_u (meV)
1	55	2,3	257
2	60	2,2	380
3	65	2,4	209
4	75	2	590

3.3. *Electrical properties*

The variation of the dark conductivity as a function of reverse temperatures is illustrated in Figure 5.

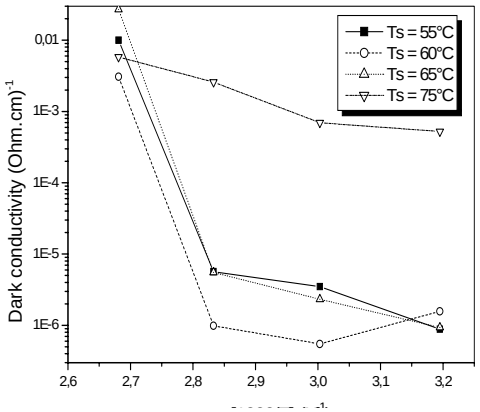

Figure 5: Variation of the dark conductivity as a function of reverse temperatures for different samples

The dark conductivity increases with increasing measurement temperature indicating the semiconducting nature of the films. From the variation of the dark conductivity versus (1000/T) we have deduced the electrical activation energy E_A (see table 2).

To determine the Fermi level position in the forbidden band, one calculates the ratio $\left(\frac{2E_A}{Eg}\right)$. The results are presented in table 2.

Table 2: $\left(\frac{2E_A}{Eg}\right)$ ratio of CBD-CdS films.

Samples	Solution temperatures (°C)	E_A	$\left(\frac{2E_A}{Eg}\right)$
1	55	0,24	0,208
2	60	0,32	0,290
3	65	0,40	0,333
4	75	0,13	0,13

As can be seen from the table 2, the $\left(\frac{2E_A}{Eg}\right)$ values are less than the unity for all solution temperatures indicating that the deposited films are of n-type. This is in agreements with earlier findings [26, 27].

The variation of the dark conductivity as a function of the solution temperature, Ts, is presented in Figure 6. For Ts lower than 65 °C, where the growth mechanism is achieved via the ion by ion mechanism, the dark conductivity varies from 10^{-6} to 10^{-7} $(\Omega\ cm)^{-1}$. These values are too low due probably to the presence of structural disorders and dislocations as interpreted by D. Padiyan and al [28]. However, in the high temperature region (Ts > 65°C), where the deposition is achieved via cluster by cluster process, the conductivity reaches 10^{-4} $(\Omega\ cm)^{-1}$. This behaviour is probably due to the presence of the hydroxide cadmium $Cd(OH)_2$ or to the sulphur deficiency in the deposited films. Indeed, Lincot et al. [29] concluded that the coexistence of the oxide and hydroxide cadmium forms is the possible reason for the sulphur deficiency.

Consequently, we suggest that CdS thin films deposited at high temperatures contain a high concentration of sulphur vacancies and cadmium interstices which act as donors defects in CdS thin films. We conclude that by varying the growth temperature it is possible to promote the deposition mechanism in order to obtain a high conductivity.

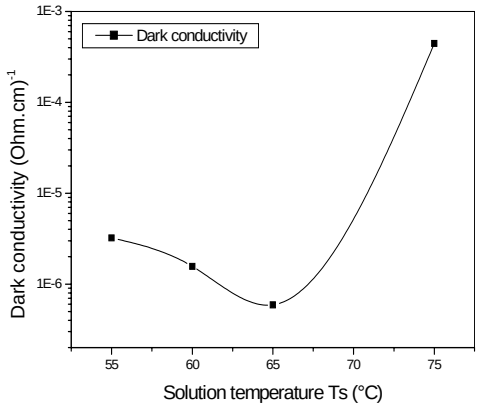

Figure 6: Dependence of dark conductivity on the solution temperature

The variation of the photoconductivity to the dark conductivity ratio $\frac{\sigma_{phot}}{\sigma_{dark}}$ as a function of the solution temperature is shown in figure 7. The photoconductivity of

the deposited films is two to five orders of decade larger than the dark conductivity. The $\frac{\sigma_{phot}}{\sigma_{dark}}$ ratio is higher in the case of films deposited at 55 and 65°C. Its value is of the order of 10^4 and 10^5 at 55 and 65°C, respectively. Whereas, films deposited at temperatures 60 and 75°C exhibit low $\frac{\sigma_{phot}}{\sigma_{dark}}$ ratio. As discussed above the films deposited at these temperatures contain more structural defects (see table 1). These defects act as traps for photogenerated carriers, and hence the reduction in their photoconductivity as suggested by Rakhshani et al [30].

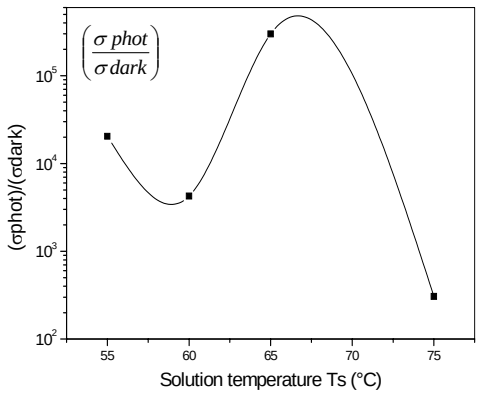

Figure 7: Variation of the photoconductivity on the dark conductivity ratio $\frac{\sigma_{phot}}{\sigma_{dark}}$as a function of the solution temperature.

4. Conclusion

In this paper, we have successfully deposited CdS thin films by the chemical bath deposition method with varied solution temperature and using a $Cd(CH_3COO)_2 2H_2O$ as a cadmium source. The films present hexagonal crystalline structure as confirmed by X-ray diffraction measurements. From the variation of the thickness and SEM images as a function of solution temperature we concluded that the CdS films are grown by the ion by ion mechanism at low temperatures (Ts < 65 °C), then changes towards cluster by cluster mechanism at higher deposition temperatures (Ts > 65 °C). Films grown show good optical transmission in visible light range and band gap values vary between 2 and 2.4 eV. The solution temperature shows a pronounced effect on the electrical property where the dark conductivity values increase from 10^{-7} to 10^{-4} $(\Omega.cm)^{-1}$ at higher temperature (Ts > 65°C). The photoconductivity of the deposited films is two to five decade larger than the dark conductivity. According to our experimental data the deposited films possess good properties which are the prerequisites for opto-electronic devices, especially for solar cell window layers.

References

[1] A. Romeo, D.L. Batzner, H. Zogg, C. Vignali, A.N. Tiwari, Sol. Energy Mater. Sol. Cells 67 (2001) 311.
[2] M.A. Contreras, M.J. Romeo, B. To, F. Hasoon, R. Noufi, S. Ward, K. Ramanathan, Thin Solid Films 403 -404 (2002) 204-211.
[3] R. Mendoza-Pérez, J. Aguilar-Hernandez, J. Sastre-Hernandez, N. Ximello-Quiebras, G. Contreras-Puente, G. Santana-Rodriguez, O. Vigil-Galan, E. Moreno-Garcia, A. Morales-Acevedo, Sol. Energy 80 (2006) 682.
[4] H. Bayhan, A. S. Kavasoglu, Sol. Energy 80 (2006) 1160.
[5] K.L. Chopra, R.C. Kaintla, D.K. Pandya, A.P. Thakoor, Phys. Thin Films 12 (1982) 167.
[6] T.L. Chu, S.S. Chu, C. Ferekides, C.Q. Wu, J. Britt, C. Wang, J. Appl. Phys. 70 (1991) 7608.
[7] L. Stolt, J. Hedström, J. Kessler, M. Ruckh, K.O. Velthaus, H.W. Schock, Appl. Phys. Lett. 62 (1993) 597.
[8] A. Catalano, Solar Energy Mater. Solar Cells 41-42 (1996) 205.
[9] B. Dimmler, E. Gross, R. Menner, M. Powalla, D. Hariskos, M. Ruckh, U. Rühle, H.W. Schock, Proc. 25th IEEE Photovoltaic Specialists Conf., Washington, DC, (1996)757.
[10] X. Wu, J. Keane, R. Dhere, C. de Hart, A. Duda, T. Gessert, S. Asher, D. Levi, P. Sheldon, in: Proccedings of the 17th European Photovoltaic Solar Conference, Munich, Germany, 22 -26, October 2001, p. 995.
[11] M.L. Breen, J.T. Woodward, D.K. Schwartz, A.W. Apblett, Chem. Mater. 10 (1998) 710.
[12] M. Kostoglou, N. Andritsos, A.J. Karabelas, Ind. Eng. Chem. Res. 39 (2000) 3272.
[13] L. Wenyi, C. Xun, C. Qiulong, Z. Zhibin, Mater. Lett. 59 (2005) 1.
[14] S.N. Sharama, R.k. Sharma, K.N. Sood, S. Singh, Mater. Chem. Phys. 93 (2005) 368.
[15] J.H. Lee, Thin Solid Films 515 (2007) 6089.
[16] I. Kaur, D.K. Pandya, K.L. Chopra, J. Electrochem. Soc. 127 (1980) 943.
[17] G. Hodes, Chemical Solution Deposition of Semiconductor Film, Marcel Dekker, Inc 2002.
[18] H. Moualkia, S. Hariech, M.S. Aida, N.Attaf, E.L. Laifa, J. Phys. D: Appl. 42 (2009) 135404 (7pp)
[19] J. Hiie, T. Dedova, V. Valdna, K. Muska, Thin Solid Films 511-512 (2006) 443.
[20] F. Chen, W. Jie, X. Cai, Thin Solid Films 516 (2008) 2827-28.
[21] J.N. Ximello-Quiebras, G. Contreras-Puente, J. Aguilar-Hernandez, G. Santana-Rodriguez, A. Arias-Carbajal Readigos, Sol. Energy Mater & Sol. Cells 82 (2004) 265.
[22] S. G. Munde, M. P. Mahabole, R. S. Khainar, J. Instrum. Soc. India 30 (1) (2000) 25.
[23] S. S. Kale, U. S. Jadhav, C. D. Lakhande, Indian J, Pure, Appl. Phys. 34 (1996) 324.
[24] G. C. Morris, R. Vanderveen, Sol. Energy Mater. Sol. Cells 27 (1992) 305.
[25] A. Ates, M.A. Yildirim, M. Kundakci, M. Yildirim, Chin. J. Phys. 45 (2-I) (2007) 135.
[26] L. Wenyi, G. Xun, C. Qiulong, Z. Zhibin, Mater. Lett. 59 (2005) 5.
[27] O. A.Ilperuma, C. Vithana, K. Premaratne, S.N. Akuranthilaka, S.M. Megregor, I.M. Dharmadasa, J. Mater. Sci. 9 (1998)367.
[28] D. P. Padiyan, A. Marikani, K. R. Murali, Mater. Chem. Phys. 78 (2002)51. [29] D. Lincot, R. Ortega-Borgees, M. Froment, Philos. Mag. B 68 (1993)185.
[30] A. E. Rakhshani, A. S. Al-Azab, J. Phys: Condens. Matter 12 (2000)8745-8755.

Journal of New Technology and Materials
JNTM
Vol. 01, N°00 (2011)51-54

OEB Univ. Publish. Co.

Elaboration and characterization of zinc oxide varistors

A. Bouchekhlal [a], Y. Beggah [b], M.S. Aida[b]

[a]*Materials Research Laboratory, Faculty of Engineering Science, Physics Department. University of Jijel, 1800 Algeria.*
[b]*Laboratory for Thin Film and Interface, Science Faculty, Department of Physics, University of Constantine Mantouri, 2500 Algeria. E-mail : ahmed_electronique81@yahoo.fr*
Received: 23 May 2011, accepted: 30 September 2011

Abstract

ZnO-based varistors were fabricated by sintering zinc oxide micro crystals with several additives of metal Oxides. The effect of sintering temperature on varistor properties of (Bi, Co, Cr, Mn, Sb, Al)-doped ZnO ceramics was investigated in the range of 1280–1350 °C. The average grain size increased to 5.13 to 7.88 µm with the increase of sintering temperature. However, the nonlinear coefficient of this system was nearly constant in the range of sintering temperature. The highest breakdown voltage was 1143.4 v / cm for the varistor sintered at 1350 °C the sample C sintered exhibited the best electrical properties.
Keywords*: ZnO; Microstructure; Electrical properties; Varistors*

1. Introduction:

ZnO varistors have been widely used as surge protection devices due to their highly nonlinear current–voltage (I–V) characteristics in the normal case, varistors are subjected to a voltage below their characteristic breakdown and pass only a leakage current. When the voltage exceeds the breakdown voltage during voltage fluctuations, the varistor becomes highly conducting and draws current through it, usually to ground. When the voltage returns to normal, the varistor returns to its highly resistive state. [1] Zinc oxide (ZnO) varistors are formed by sintering mixture of ZnO powders with small amounts of other oxides, such as Bi_2O_3, Sb_2O_3, Al_2O_3, MnO_2, Cr_2O_3, etc., the relationship between the voltage across the terminal, V, and the current in the devices, I, is typically expressed by $I = kV^{\alpha}$. The term α in the equation is a nonlinear coefficient, inherent parameter of varistors representing the degree of nonlinearity of conduction. It is very important to comprehend the influence of the sintering process on varistor properties. The influence of sintering temperature on varistor properties is different with existing compositions of ceramics. [2]

The purposes of the present study are to develop the ZnO-based ceramic varistors. In this work, ZnO-based ceramic varistors with more than five additives of metal oxides have been fabricated. The microstructure of the varistors were studied using scanning electron microscopy (SEM) and X-ray diffraction(XRD) analysis and the properties of the ZnO based ceramic for use as varistors were discussed on the basis of the measurements of V(I) and C(V) characteristics.

2. Experimental procedure

2.1. Sample preparation

ZnO– Bi_2O_3-based varistor samples with a nominal composition of 97.2 mol.% ZnO, 0.5 mol.% Bi_2O_3, 1.0 mol.% Sb_2O_3, 0.3 mol.% Al_2O3, 0.5 mol.% Cr_2O_3, and 0.5 mol.% MnO_2 were used, samples (B). Reagent-grade raw materials were pulverized by an agate mortar/pestle for 1h. Reagent-grade raw materials were used for preparing the varistor (C) of 98 mol.% ZnO, 0.5 mol.% Bi_2O_3, 1.0 mol.% Sb_2O_3, 0.5 mol.% Cr_2O_3, Reagent-grade raw materials were mixed and homogenized in absolute ethanol media in a polyethylene bowl with zirconia balls for 24 h. After milling, the mixture was calcined in air at 750 °C for 2 h. [3] The calcined powders were pressed into discs of 13 mm in diameter and 1 mm thickness at a pressure of 1000 kg/cm2. The discs were sintered at four fixed sintering temperatures 1280 °C, 1300 °C, 1320 °C, and 1350°C in air for 1 h in a furnace (Nabertherm, MORE THAN HEAT 30-3000 °C), at a heating rate of 5 °C/min and then cooled in the furnace. Finally, the surfaces of the sintered Samples were grinded and covered with silver paste to obtain electrodes. [4]

2.2. Characterization

The microstructure was examined by a scanning electron microscope PHILIPS (XL 30). The average grain size (d) of the ceramics was determined by the linear intercept method , given by d = 1.56L/MN,[5] where L is the random line length on the micrograph, M is the magnification of the micrograph, and N is the number of the grain boundaries intercepted by lines. [6] The crystalline phases were identified by an X-ray diffractometry (BRUKER - AXS type D8) with CuKα radiation. The electric field–current density (E–J) characteristics were measured using a V–I source (TEKTRONIX 370) The breakdown field ($E_{1mA/cm2}$) was measured at 1.0mA/cm^2 and the leakage current density (J_L) was measured at 0.8 $E_{1mA/cm2}$ In addition, the nonlinear coefficient (α) is defined by the empirical law, $J = CE^{\alpha}$ where J is the current density, E is the applied electric field, and C is the constant. ˛ was determined in the current density range of 1mA/cm^2 to 10mA/cm^2, where $\propto = 1/(logE_2 - Elog_1)$, and E_1 and E_2 are the electric fields corresponding to 1.0mA/cm^2 and10mA/cm^2, respectively. The capacitance–voltage (C–V) characteristics were measured at 1 MHz as test frequency using an RLC meter (KEITHLE 590). The donor concentration (N_d) and the barrier height (Φ_b) were determined by the equation $(1/C_b - 1/2C_{b0})^2 = 2(\varphi_b + V_{gb})/q\varepsilon N_d$ where C_b is the capacitance per unit area of a grain boundary, C_{bo} is the value of C_b when V_{gb}=0, V_{gb} is the applied voltage per grain boundary, q is the electronic charge, ε is the permittivity of ZnO (ε=8.5εo). [7]

3. Results and discussion

Fig. 1 shows XRD patterns to the samples for different sintering temperatures. In all cases diffraction peaks corresponding to the major ZnO hexagonal phase are obtained (JCPDS card no 36-1451), together with some secondary peaks attributed to the Zn7Sb2O12 spinel and the Bi2O3 phases (JCPDS cards no 36-1445 and no 41-1449, respectively). The spinel phase plays an important role as the grain growth inhibitor during the sintering process of the varistor sample. Actually, this is the characteristic distribution of crystalline phases for a varistor formulation based in the ZBS ternary system. [8][9] For all temperatures a shift in the peaks positions to the right was observed with increase of sintering temperature.

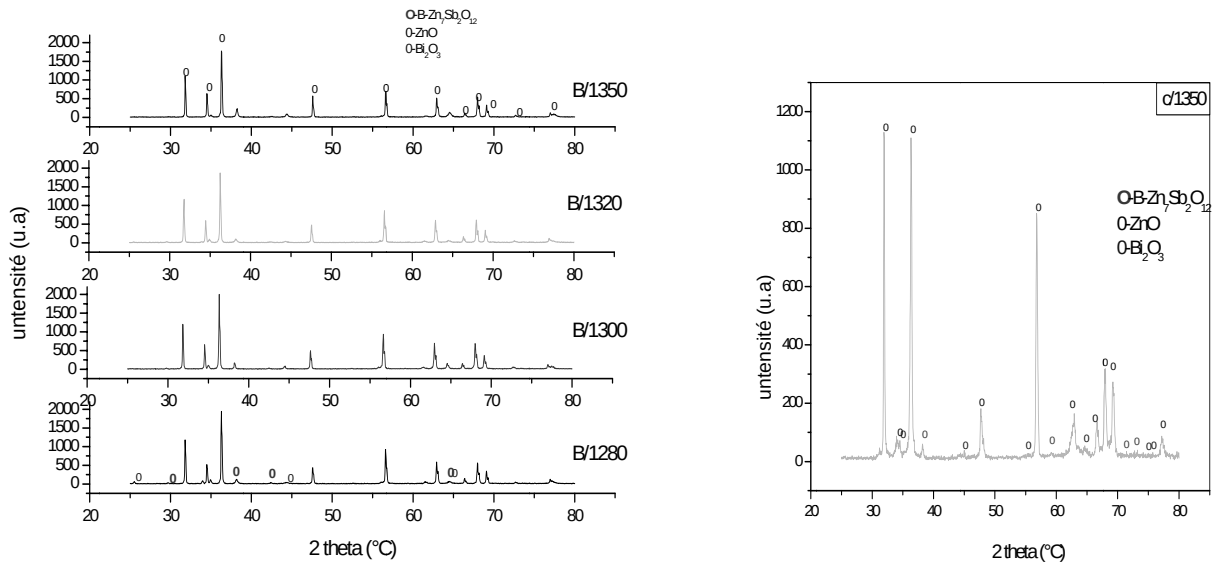

Fig. 1 XRD patterns of the samples for different sintering temperatures

Table 1:Microstructure and E_J characteristic parameters of the samples for various sintering temperatures

Sintering temperature (°C)	d(μm)	E(v/cm)	α	J_L (μA/cm^2)	N_d(10^{18}cm^{-3})	φ_b(ev)
B/1280	4.54	31.34	1.64	62.5	0.0043	1.21
B/1300	5.14	36.59	1.47	93.3	1.01	0.77
B/1320	5.81	6.35	1.04	77.6	1.93	0.30
B/1350	6.06	13.79	1.42	79.4	0.55	0.29

The SEM micrographs of the varistor samples for various sintering temperatures are shown in Fig. 2. There is no remarkable difference in the phases, which consisted of ZnO grains and intergranular layers in accordance with sintering temperatures. The average grain size (d) greatly increased from 4.54 to 7.88 μm in accordance with increasing sintering temperatures. The detailed microstructure parameters are summarized in Table 1.

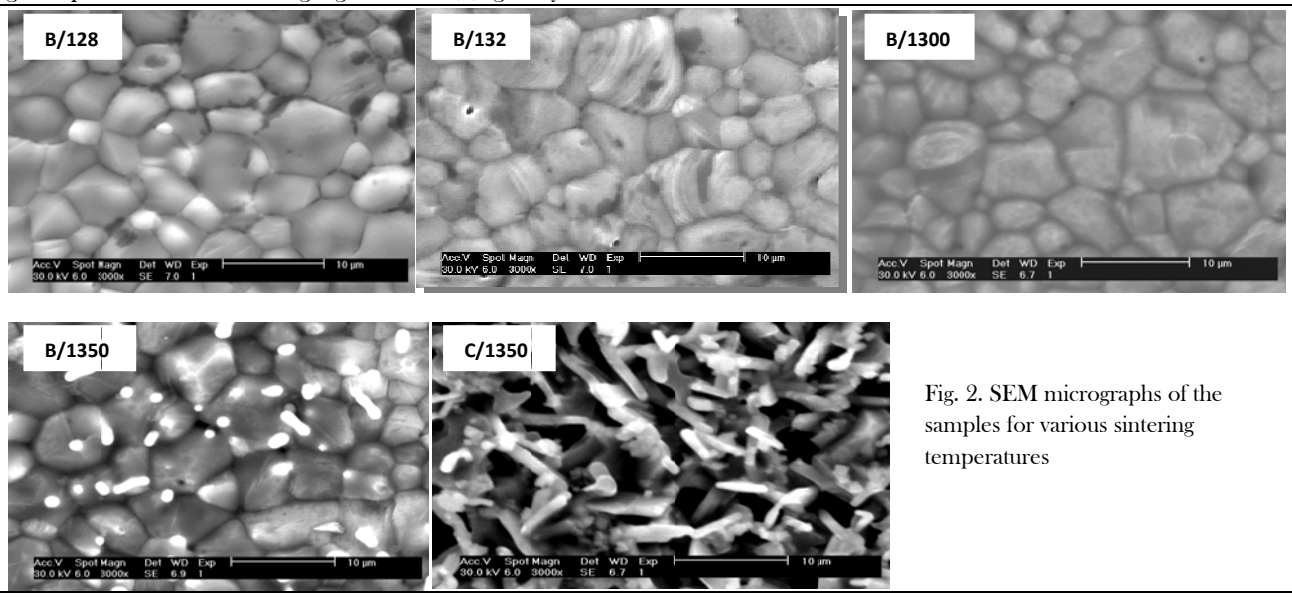

Fig. 2. SEM micrographs of the samples for various sintering temperatures

Fig. 3 shows the E–J characteristics of the samples for different sintering temperatures. The conduction characteristics of varistors are divided into a linear region with much higher. impedance before breakdown field and a nonlinear region with much lower impedance after breakdown field. The E–J characteristic parameters calculated from Fig. 3 are summarized in Table 1. Results showed that sample (C) sintered at 1350°C had the best nonlinear electrical property since it had the largest nonlinear coefficient of 3.39. The minimum J_L value (59.06 $\mu A/cm^2$) was obtained in that sample (C) sintered at 1350°C . The nonlinear coefficient (α) decreased slightly with the increase of sintering temperature. [1] The variation of J_L, on the whole, was opposite to that of nonlinear coefficient. The breakdown field (E) decreased with the increase of sintering temperature. This is attributed to the decrease in the number of grain boundaries caused by the increase in the ZnO grain size.

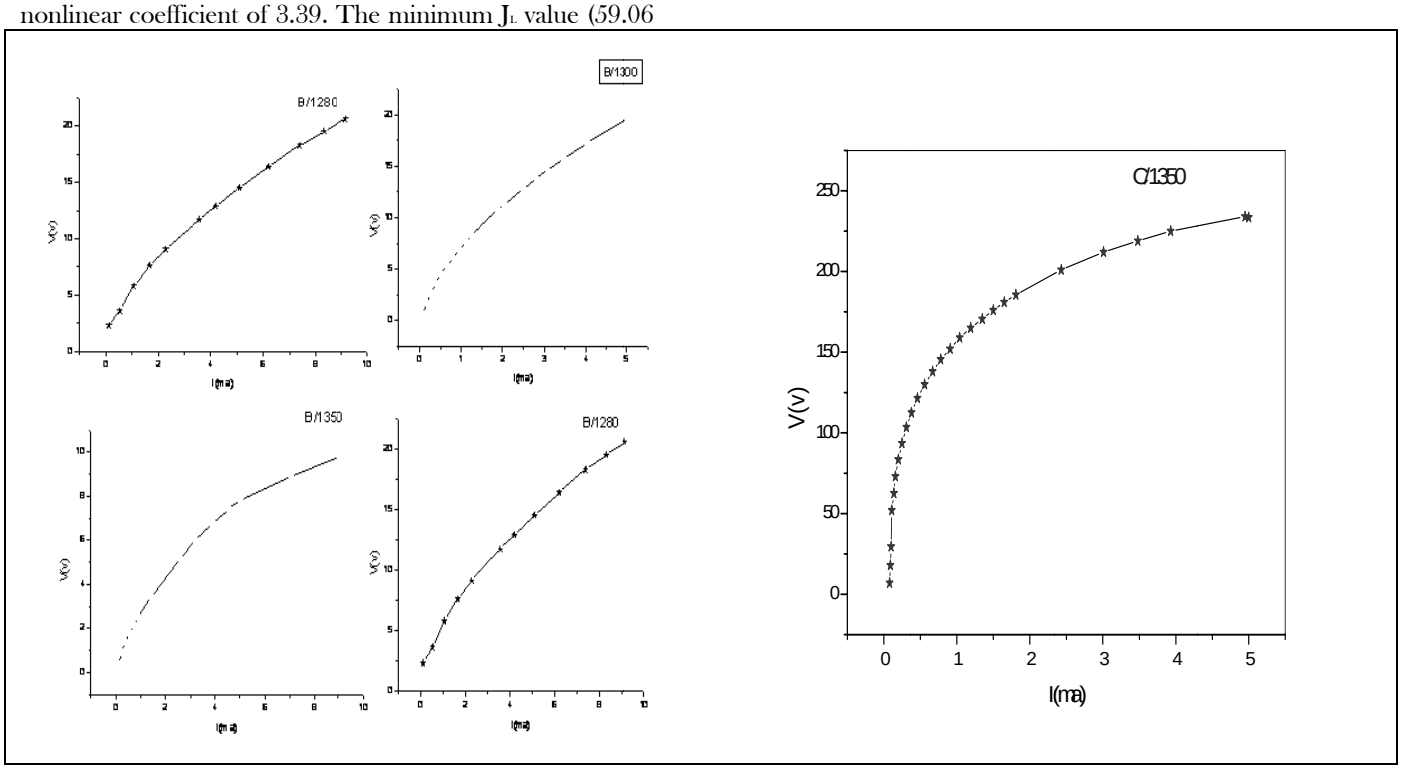

Fig. 3. I_V characteristics of the samples for various sintering temperatures

The *C–V* characteristics of the samples for different sintering temperatures are shown in Fig. 4. Modified C-V curves gradually shifted upward with decreasing sintering temperatures . The detailed *C–V* characteristic parameters are summarized in Table 1. the donor concentration (N_d) and barrier height (φ_b) are calculated by the modified C-V equation. The N_d value decreased slightly from $2.8^* 10^{18}$ to $0.39^* 10^{18}$ cm^{-3} with the increase of sintering temperature. The decrease of the N_d value is assumed to be due to an increase of oxygen. The barrier height (φ_b) at the grain boundaries decreased from 1.21 ev to 0.29eV with the increase of sintering temperatures. This coincides with the variation of the α in the E_J characteristics.

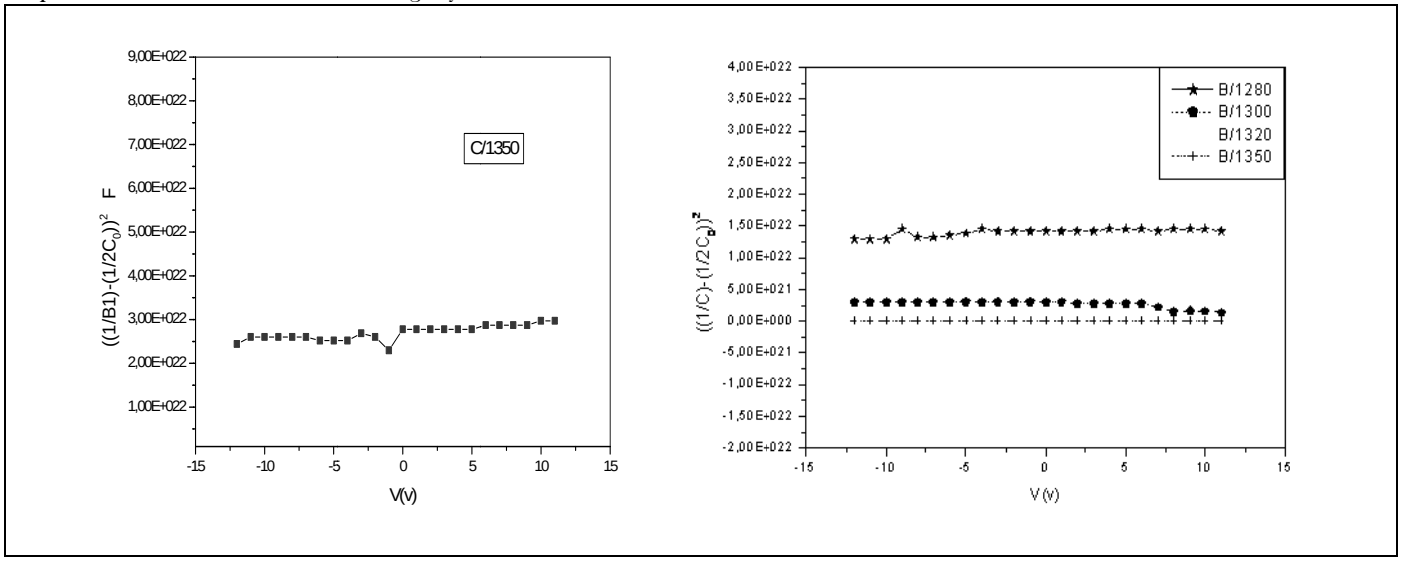

Fig. 4. C_V characteristics of the samples for various sintering temperatures.

4. Conclusions

The dependence of the microstructure and electrical propertie of Zn–Bi-Sb-Al-Mn-based varistors on the sintering temperatures was investigated. The average grain size greatly increased with the increase of sintering temperature. The breakdown field decreased due to the increase of ZnO grain size and the decrease of the breakdown voltage per grain boundary. A maximum value (3.39) of the nonlinear coefficient was obtained for the sample (C) sintered at 1350°C. Conclusively, this system provides the advantage of applications because it exhibits a nearly constant nonlinear coefficient.

References

[1] Wangcheng Long, Jun Hu, Effects of cobalt doping on the electrical characteristics of Al-doped ZnO varistors, Materials Letters 64 (2010) 1081–1084

[2] C.-W. Nahm The effect of sintering temperature on varistor properties of (Pr, Co, Cr, Y, Al)-doped ZnO ceramics, Materials Letters 62 (2008) 4440–4442

[3] Choon-W Nahm, The preparation of a ZnO varistor doped with Pr_6O_{11}_CoO_Cr_2O_3_Y_2O_3_Al_2O_3 and its properties, Solid State Communications 149 (2009) 795_798

[4] Dong Xu, Liyi Shi, microstructure and electrical proprieties of ZnO- Bi_2O_3 based varistors ceramics by different sintering processes, journal of the European ceramic society 29(2009) 1789-1794.

[5] M.F. Yan, A.H. Heuer, Additives and Interfaces in Electronic Ceramics, Am. Ceram. Soc., Columbus, OH, 1983, p. 80.

[6] J.C. Wurst, J.A. Nelson, Lineal intercept technique for measuring grain size in two-phase polycrystalline ceramics, J. Am. Ceram. Soc. 55 (1972) 109–111.

[7] M. Peiteado, Y. Iglesias, A.C. Caballero, Sodium impurities in ZnO–Bi2O3–Sb2O3 based varistors, Ceramics International 37 (2011) 819–824.

[8] Choon-W. Nahm, Varistor properties of ZnO-Pr6O11-CoO-Cr2O3-Y2O3-In2O3 ceramics, Materials Letters xxx (2011) xxx–xxx

[9] E. Olsson, G. Dunlop, R. O¨ sterlund, Development of functional microstructure during sintering of a ZnO varistor material, J. Am. Ceram. Soc. 76 (1993) 65–71

Journal of New Technology and Materials
JNTM
Vol. 01, N°00 (2011)55-58

OEB Univ. Publish. Co.

Electronic structure calculation of the GaAs/AlAs quantum dot superlattices

F. kanouni, A. Brezini, N. Sekkel, A. Saidane, D. Chalabi, A. Mostefa
Labo.CaSiCCE, ENSET-Oran, Algeria, Department of Electrical Engineering
Received: 23 May 2011, accepted: 30 September 2011

Abstract

Theoretical investigation of the electronic structure of GaAs/AlAs quantum dots superlattices is presented. We use the envelope function approximation in connection with Kronig-Penney model to calculate the conduction band structure of the cubic quantum dot crystal. . We show that, when quantum dots are separated by a finite barrier and positioned very close to each other so that there is a significant wave function overlap, the discrete energy levels split into three-dimensional minibands. We can control the electronic structure of this artificial quantum dot crystal by changing theirs technological parameters, the size of quantum dots, interdot distances, barrier height, and regimentation. This type of structure provides electronic and optical properties very important that are different to that of bulk and quantum well superlattices. The proposed engineering of three-dimensional minibands in quantum dot crystals allows one to fine-tune electronic and optical properties of such nanostructures.

Keywords: *quantum dots, semiconductor superlattices, envelope function approximation*

1. Introduction

Recently low dimensional systems at nanometer scale have stimulated a new promising research in condensed matter. Mainly these structures opened a crossover between the physics of bulk condensed matter and few body systems. The progress of experimental techniques have made feasible the possibility of quantum confinement of only few electrons, often referred as "man made structures" [1]. In particular, semiconductor quantum dots (QD) have many potential applications in various domains such in electronic devices, information processing and non-linear optic.

Nanometer-sized semiconductor quantum dots can be grown in the Stranski-Krastanow mode using molecular beam epitaxy [2] or metal-organic chemical vapor deposition [3].

The interest in quantum dot superlattices (QDS) structures combined system lies on the ability to tune optical transition energies by varying SL period as well as by changing QD parameters. Nowadays, the suitability of mid-infrared photodetectors was confirmed [4,5].

In addition, it was shown that QDS together with their wetting layer modify significantly the energy structure in the case of GaAs/AlAs Therefore, in order to determine optimal design for applied purposes, an appropriate knowledge about their optical properties and electronic structures of combined QD/SL systems is fundamental.

The aim of this paper is to investigate the electron energy band structure in a 3D *regimented* array of QD semiconductors by means the envelope function approximation. The regimentation, namely spatial site correlation, along the three directions results in the grow of an artificial crystal, where quantum dots play the role of atoms. Such structure is then referred as a *quantum dot crystal* (QDC). As originally considered by [6], we paid our attention on simple cubic QDC consisting in very small (size about of 5–10 nm) GaAs quantum dots grown on AlAs and surrounded by AlAs cap layer.

In the next section, we outline the theoretical formalism used for calculating 3D energy minibands. It is followed by Section. III, which presents results of the numerical simulation and discussion. Our conclusions are given in Sec. IV.

2. Analytical study

In order to simplify our analytical calculation, we restrict our analysis to simple structures formed by the periodic arrangement of cubic quantum dot, along the three axes x, y and z as shown in Fig (1.a). We also show in this figure the notations used throughout the rest of the article. Our goal in this section is develop a simple, almost analytical, formalism using the envelope function approximation, for carrier transport in QDC that would serve as a useful tool for experimentalists and materials growers.

Theoretical models for quantum dots within the envelope function approximation usually lead to a complex multidimensional Schrödinger equation, which needs to be solved using finite elements method, or plane wave expansion. Application of the pseudopotential methods for QDC is computationally challenging.

In our analyzis, we intersent to the conduction band of the GaAs/AlAs QDC. We this is done for several reasons. First of all, the most of the band gap discontinuity between GaAs and AlAs goes to the conduction band. Second, the potential energy minimum in the conduction band is located in Γ point, which greatly simplifies the model and justifies our omission of carrier Bloch functions from consideration [7].

The Schrödinger equation that describes the motion of a single electron in such a system can be written in the following form:

$$\left[-\frac{\hbar^2}{2}\nabla_r \frac{1}{m^*(r)}\nabla_r + V(r)\right]F(r) = EF(r) \qquad (1)$$

Here, the atomic structure of the host semiconductor enters the analysis as an effective mass m^*. This parameter assumes different values in the quantum dot and the barriers.

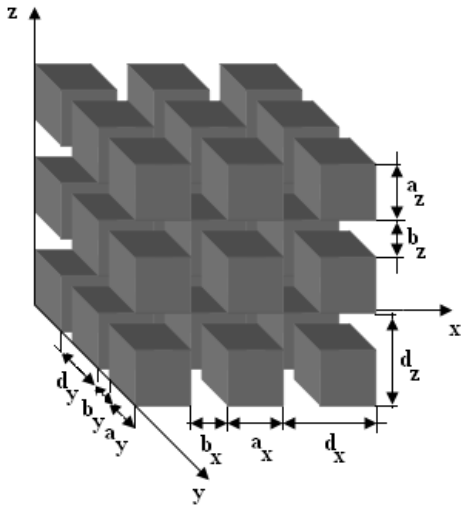

FIG.1. Schematic structure of the cubic QDC

The potential $V(r)$ corresponds to an infinite sequence of quantum dots of size, a_x, a_y and a_z separated by the barriers of thickness, b_x, b_y and b_z. We assume that it is written as a sum of three independent periodic functions of coordinates, x, y and z with periods of d_x, d_y and d_z

$$V(r) = V_x(x) + V_y(y) + V_z(z) \qquad (2)$$

where

$$V_\xi(\xi) = 0 \quad \text{For} \quad \left|\xi - \eta_\xi d_\xi\right| \le a_\xi / 2 \qquad (3)$$

$$V_\xi(\xi) = V_0 \quad \text{For} \quad \left|\xi - \eta_\xi d_\xi\right| \ge a_\xi / 2$$

with $$d_\xi = a_\xi + b_\xi \qquad (4)$$

Here η_ξ are the integer numbers and subscript ξ denotes a particular coordinate axis. This choice of potential allows us to separate the carrier motion along three coordinate axes. The 3D envelope wave function $F(r)$ can therefore be presented as a product of three 1D eigenfunctions ϕ_ξ in the following way:

$$F(r) = F_{n_x,n_y,n_z}(x,y,z) = \phi_{n_x}(x)\phi_{n_y}(y)\phi_{n_z}(z) \qquad (5)$$

The 3D Schrödinger equation also decouples in this case into three identical one-dimensional (1D) quantum-well superlattices.

$$\left[-\frac{\hbar^2}{2}\frac{\partial}{\partial x}\frac{1}{m^*(x)}\frac{\partial}{\partial x} + V_x(x)\right]\phi_{n_x}(x) = E_{n_x}\phi_{n_x}(x) \qquad (6a)$$

$$\left[-\frac{\hbar^2}{2}\frac{\partial}{\partial y}\frac{1}{m^*(y)}\frac{\partial}{\partial y} + V_y(y)\right]\phi_{n_y}(y) = E_{n_y}\phi_{n_y}(y) \qquad (6b)$$

$$\left[-\frac{\hbar^2}{2}\frac{\partial}{\partial z}\frac{1}{m^*(z)}\frac{\partial}{\partial z} + V_z(z)\right]\phi_{n_z}(z) = E_{n_z}\phi_{n_z}(z) \qquad (6c)$$

Here n_ξ denote the quantum number. The total energy spectrum for the wave function $F(r)$ is given by:

$$E_{n_x,n_y,n_z} = E_{n_x} + E_{n_y} + E_{n_z} \qquad (7)$$

Where E_n are the eigenvalues of the one-dimensional Schrödinger's equation.

For the chosen geometry of QDC and band offsets the carrier wave functions and energy spectrum are mostly determined by the nearest-neighbor interaction between dots separated by the potential barrier V_0.

The corner potentials induce only minor corrections, which are particularly small for the below-the-barrier states. This observation is important because the confining potential of Esq. (2) and (3) does not describe a simple QDC of a rectangular quantum dot surrounded by the potential barrier of the equal height.

In two dimensions, this situation is clear. Fig (2a) illustrates the two-dimensional confinement potential; with this configuration it is not possible to write the two-dimensional potential as a sum of two independent one-dimensional potential, and thus it is not possible to separate the x- and y-motions.

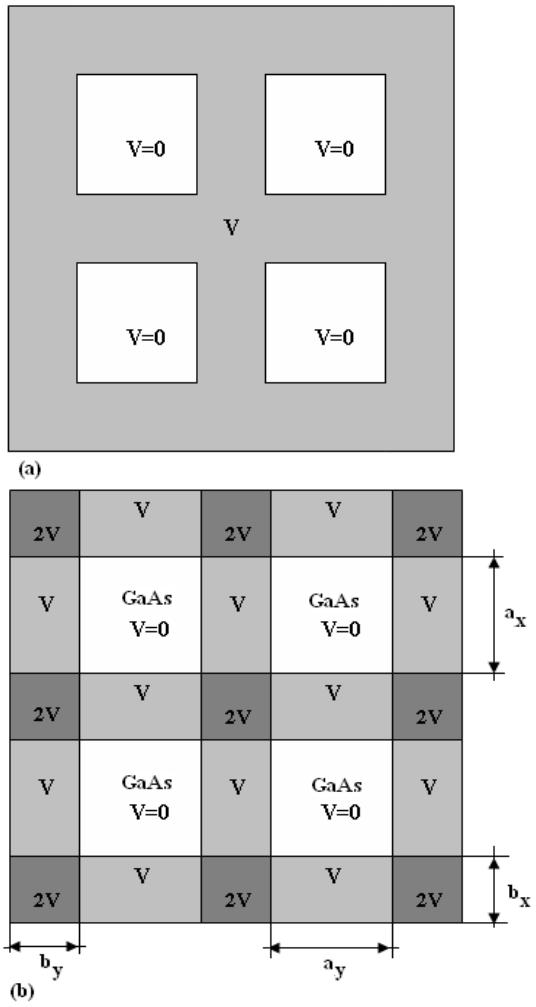

FIG.2. (a) the rectangular cross-section confinement potential ; and (b) an approximation form for the potential, suitable for decoupling the motion Note that the carrier states in quantum dots are mostly determined by interaction with nearest-neighboring dots separated from each other by the potential V0

However, a very loose approximation may be to write the potential as in Fig (2b) [8]. With this form, the potential does equal the sum of tow independent finite well potential. The approximation occurs in the corner region outside of the quantum dots where the two quantum well potential barrier heights V_0 sum to give $2V_0$. Similarly, in 3D, there exist outer regions where the overlap of 1D potentials along each axes gives rise to a potential barrier of $3V_0$.

The solution of Eq (1) with the potential of Eqs (2) and (3) has the form familiar from the Kronig–Penny model [9]. By using the transfer matrix method [10] and the boundary condition of Bastard [11], we arrive:

For $E_\xi > V_0$ (8a)

$$\cos(q_\xi d_\xi) = \cos(k_\xi^w a_\xi)\cos(k_\xi^b b_\xi) - \frac{1}{2}\left(R + \frac{1}{R}\right) \times \sin(k_\xi^w a_\xi)\sin(k_\xi^b b_\xi)$$

For $0 < E_\xi < V_0$ (8b)

$$\cos(q_\xi d_\xi) = \cos(k_\xi^w a_\xi)\cosh(k_\xi^b b_\xi) - \frac{1}{2}\left(-R + \frac{1}{R}\right) \times \sin(k_\xi^w a_\xi)\sinh(k_\xi^b b_\xi)$$

white

$$R = \frac{k_\xi^B m_w^*}{k_\xi^w m_B^*} \quad (9)$$

where

$$k_\xi^w = \frac{1}{\hbar}\sqrt{2m_w^* E_\xi}\ , \quad k_\xi^b = \frac{1}{\hbar}\sqrt{2m_b^* \left|E_\xi - V_0\right|} \quad (10)$$

The effective masses m_w^* and m_b^* used in Eqs. (8). and (10) depend on the crystallographic orientation of the quantum dot interfaces. Equations (8) and (10) allow us to calculate the carrier dispersion relation in the QDC:

$$E(q) = E_x(q_x) + E_y(q_y) + E_z(q_z) \quad (11)$$

Since for each given value of q_ξ there is an infinite number of solutions, we use the miniband index n_ξ to label the carrier energy.

3. Numerical results

In this section, we show that despite the simplicity of the theoretical formalism used, it is capable of capturing new features characteristic for 3D artificial QDC that are not present in real bulk crystals and quantum well superlattices.

We carry out our analysis of the 3D minibands in the artificial QDC, on the example of GaAs/AlAs material system. In our calculations, we used the following values for the effective masses:

$$m_w^* = m_{GaAs}^* = 0.067 m_0\ ,\ m_b^* = m_{AlAs}^* = 0.15 m_0$$

We show in Fig.3 the electron dispersion in a simple cubic QDC along [100] crystallographic direction. The energy band structure following from Eqs (8), it is not surprising. In fact, it is expected from the format similarity between them and the Kroing-Penny relation of the superlattices. The carrier wave vector is denoted by q with subscript showing particular quasi crystallographic direction. Zero energy along the ordinate axis corresponds to the position of the potential barrier.

The results in Fig. 2 are shown for a QDC that consists of quantum dots with the size $a = 6.5nm$ and interdot distance $b = 1.5nm$. The energy bands are denoted by three quantum numbers $n_x n_y n_z$ with the superscript indicating the degeneracy of the band.

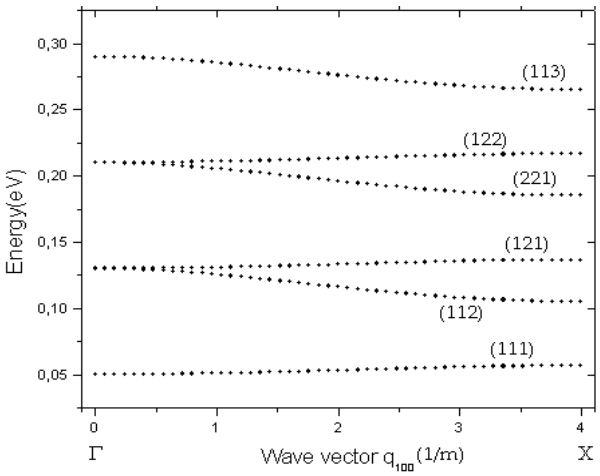

FIG. 3 Dispersion relation in a cubical QDC shown along [100] quasi crystallographic direction

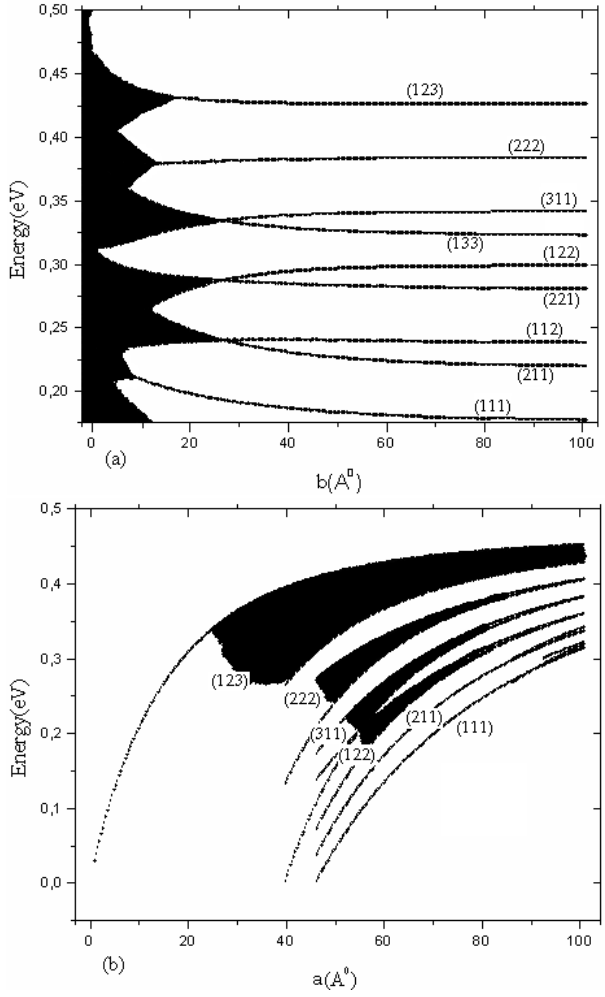

FIG. 4. (a) Miniband width as a function of the interdot distance. The size of the dots is 6.5nm. (b) Miniband energy as a function of dot size. The interdot distanc is 1.5nm.

The energy bands shown in Fig.3 are degenerated in the center of the quasi Brillouin zone (QBZ) of the artificial crystal. The highest, sixfold, degeneracy is achieved in minibands of cubical QDC characterized by different quantum numbers. If two of these three quantum numbers are equal, the degeneracy is threefold. Finally, if three quantum number are equal, there is no symmetry degeneracy in such a miniband. Moving from the point of high symmetry in the center of the QBZ to a point of lower symmetry, the energy bands split. This degeneracy is a result of the same symmetry of the dots and the superlattice. If their symmetries are different, the twofold degeneracy will be the maximum permitted in all directions.

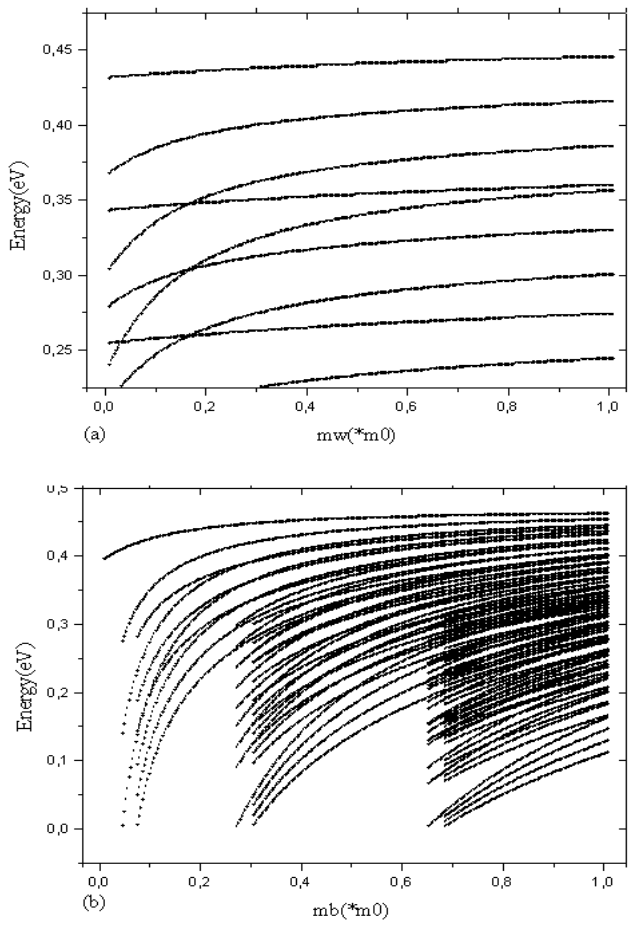

FIG.5. (a) Energy as a function of the masse in the well. (b) Energy as a function of the masse in the barrier

The formation of 3D minibands in QDC is illustrated in Figs. (4a) and (4b). It is well known that a single quantum dot has discrete spectrum below a potential barrier and continuous spectrum above the potential barrier. When quantum dots are separated by a finite barrier and positioned very close to each other so that there is a significant wave function overlap, the discrete energy levels split into minibands. This can be seen in Fig. (4a) for the interdot distance b below 3 nm. As the interdot distance increases, and the wave function overlap decreases, the minibands below the potential barrier reduce to discrete levels. This behavior is expected and consistent with what one observes in conventional quantum well superlattices. The 3D regimentation of quantum dots in QDC leads to appearance of "resonant" quasidiscrete energy levels above the potential barrier V_0 for large interdot distances (5 nm for GaAs/AlAs) as seen in Fig. (4a). Figure (4b) demonstrates a transformation of QDC minibands into discrete levels below the potential barrier and quasicontinuum above the barrier. Other important observations to make in Fig. (4b) are that the miniband width does not increase monotonously with the energy, and that for realistic interdot distances complete energy gaps (stop bands) are formed in QDC.

We can have the same information about the formation the minibands structure in GaAs/AlAs-QDC by the variation of the barrier and well masses (see Fig.5.)

4. Conclusion

Quantum dot superlattices QDSLs offer prospects for new generation of semiconductor devices. In particular; the GaAs/AlAs-QDSLs have attracted considerable attention due to application for infrared photodetector.

In this paper, the carrier band structure in a 3D *regimented* array of semiconductor quantum dots QDC has been analyzed. Numerical simulations have been carried out for the conduction band of a GaAs/AlAs quantum dot crystals. It was shown that the coupling among quantum dots leads to a splitting of the quantized electron energy levels of single dots, which results in the formation of 3D minibands. By changing the size of quantum dots, interdot distances, barrier height, and regimentation, one can control the electronic band structure of this artificial crystal. The properties of the artificial crystals turned out to be more sensitive to the dot regimentation than to the dot shape.

References

[1] S.M. Riemann and M. Manninen, Rev. Mod. Phys.74, 1283,(2002).

[2]J. L. Liu, W. G. Wu, A. Balandin, G. L. Jin, and K. L. Wang, Appl. Phys. Lett. 74, 185 (1999)

[3] P. C. Sharma, K. W. Alt, D. Y. Yeh, and K. L. Wang, Appl. Phys. Lett. 75, 1273 (1999)

[4] FF Schrey, L. Rebohle , T. Mueller, G. Strasser, K. Unterrainer, D. Nguyen, R. Regnault ,R. Ferreira and G. Bastard, PRB72, 15310; 2005

[5] R. Nedzniskas, B. Cechavicius, J. Kavaliaus, V. Karpus, G. Krivaitté, V. Tamosinuas, G. Valusis, F. Schrey , K. Unterrainer and G. Strasser, Acta Physica Polonica A113,975 (2008)

[6] O. L. Lazarenkova and A. N. Pikhtin, J. Appl. Sci. 89, 5509 (2001)

[7] M. Stslicka, R. Kucharczyk, A.Akjouj. Surface. Science. Raports 47 93(2002)

[8] P.Harrison, *Quntum Well, Wires and Dot*, the University of Leeds, UK (2000)

[9] R.D.Kronig and W.J.Penny, Proc. R. Soc London Ser. A. 130 499(1931)

[10] R.Tsu, *Superlattices to Nanoelectronics*, University of North Carolina, Charlotte, North Carolina, USA (2005)

[11] G. Bastard, *Wave Mechanics Applied to Semiconductor Heterostructures* (Halsted Press, New York, 1988)

Journal of New Technology and Materials
JNTM
Vol. 01, N°00 (2011)59-62

OEB Univ. Publish. Co.

Numerical analysis of GaAs MESFETs OPFET

I. Hamma[a], Y. Saidi[b], M. Zaabat[a] and C. Azizi[a]
[a]*Laboratoire Composants Actifs et Matériaux, Univesité dOum El Bouaghi*
[b] *Université Mentouri, Constantine, 25000, Algérie*
Received: 23 May 2011, accepted: 30 September 2011

Abstract
A Tow dimensional numerical model of channel potential for GaAs MESFET (Metal semiconductor field effect transistor) doped uniformly .the model takes into acount the effects in channel region considering both the photoconductive effect and photovoltaic effect at the gate schottky . the 2-D potential distribution function in the active layer of the divice is solved numerically under dark and illumination condition.
Keywords*: 2-D modeling potential distribution, Photodetector, Photovoltage.*

1. Introduction

Later on ,the optically controlled MESFET was named on optical Field effect transistor OPFET. The photosensitivity of the MESFET has opened up the possibility of their use for a variety of optoelectronic application. At present the GaAs MESFET's under illumination plays an important role in communication technology For wide band multimedia and high speed application. An idea that has been widely investigated recently for performing optically controlled functions and it can be used to form an additional input port in photonic (MMIC) [1] and also drawn considerable attention potential application ion due to their potential of device.

As a number of research of theoretical and experimental works have been reported on optically controlled MESFET . A simple analytical model of an ion implanted GaAs MESFET is useful for computer aided design of divices and integrated circuits (IC's).To examine the optical controlled characteristics of GaAs Mesfet is necessary used model of optically gated Mesfet photodetector considering the short channel effect .This paper present the two-dimensional numerical simulation of MESFET using the Liebman iterative method in order to simulate 2D channel Potential and Elecric field equation.

2. Theoretical model

The 2-D Poisson's equation in the space charge region of the device in illuminated condition and Schottky contact [2,3]. Can be written as

$$\frac{d^2\psi(x,y)}{dx^2}+\frac{d^2\psi(x,y)}{dy^2}=-\frac{q}{\varepsilon}\left(N_d(x,y)-A\exp(-\alpha y)\right) \quad (1)$$

$$A=\frac{P_{opt}(1-R_s)(1-R_m)\alpha\tau_L}{h\gamma} \quad (2)$$

Where, $\psi(x,y)$ is 2-D Potential distribution $N_d(x,y)=N_d$ corresponds to the donor (uniform doping density) ,q (Electron charge), ε_s (Permittivity of the GaAs), (R_m,R_s) (are Reflection coefficient at the entrance and Reflection coefficient at the metal semiconductor contact), P_{opt} (Incident optical power density), α (Optical absorption coefficient of the semiconductor at the operating wavelength), h (Planck's constant), γ (Frequency of the incident radiation), τ_L (Mean lifetime of the minority carriers under illumination condition [4]).

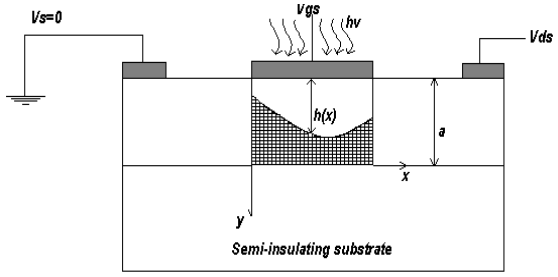

Fig.1 Schematic of MESFET under illumination

The boundary conditions as related to the Poisson's equation are taken from [3,5].

$$\begin{aligned}&\psi(x,0)=V_{gs}+V_{op}-\phi_{bi}\\&\psi(0,y)=V_{bi}\\&\psi(L,y)=V_{bi}+V_{ds}\\&\psi(x,a)=0\end{aligned} \quad (3)$$

Where
Vgs Gate to source voltage
Vds Drain to source voltage
Vbi Built in volge between the channels to source junction
Øbi Built in voltage of the Schottky barrier gate.

Due to illumination, the device performance varies due to the photovoltage developed at the Schottky junction. This photovoltage is calculated using the following relation [7]

$$V_{op} = \frac{nKT}{q} \ln\left[\frac{q}{J_{SC}} \frac{\alpha P_{opt}}{h\gamma L} \left(\int_0^L \int_0^{h(x)} \exp(-\alpha y) dx dy\right)\right] \quad (4)$$

where $h(x)$ is the extension of the Schottky junction depletion region in the channel measured from the surface is given as

$$h(x) = \left[\frac{2\varepsilon}{qN_d}\left(\phi_B - \Delta + V(x) - V_{gs}\right)\right]^{\frac{1}{2}} \quad (5)$$

$h'(x)$ is the is the extension of the Schottky junction depletion region in the channel measured from the surface under illumination is given by

$$h(x)' = \left[\frac{2\varepsilon}{qN_d}\left(\phi_B - \Delta + V(x) - V_{gs} - V_{op}\right)\right]^{\frac{1}{2}} \quad (6)$$

The excess carriers generated per unit volume in the semiconductor due to the absorption of incident optical power density is given by

$$\Delta n = \frac{1}{H_m} \int_0^{H_m} G_{op}(x, y) \tau_L dy \quad (7)$$

Where Hm is the maximum width of the depletion layer

$$H_m = \left[\frac{4\varepsilon \ln(\frac{N_a}{n_i})}{q\beta N_a}\right]^{\frac{1}{2}} \quad (8)$$

τ_L is the minority carrier life time given by

$$\tau_L = (\frac{n_i}{ni + \Delta n})\tau \quad (9)$$

and $G_{OP}(x, y)$ is the excess generation rate at any point y in the semiconductor and is given by

$$G_{op}(x, y) = A \int_0^L \int_0^a \exp(-\alpha y) dx dy \quad (10)$$

3. I-V Characteristics

The drain current Ids has been calculated by numerically integrating the charge in the channel region given by

$$I_{ds} = \mu_n \frac{Z}{L} \int_0^{V_{ds}} \varphi_n(V) dV \quad (11)$$

The charge is calculated using the relation (1)

$$\varphi_n(v) = q \int_{h(x)}^a N_d(y) dy + qA \int_0^a \exp(-\alpha y) dy \quad (12)$$

Where μn is the mobility of electrons, and $\varphi_n(V)$ is the charge in the neutral channel region per unit area at a point x where the channel voltage $V(x)$ is given by [6], $h(x)$ is function of the channel voltage $V(x)$.

3.1. Mobility model

The field dependent mobility of the charge carriers in the channe lis given by

$$\mu_n(E_x, E_y) = \frac{\mu_0(E_y)}{\left[1 + (\frac{E}{E_c})^2\right]^{\frac{1}{2}}} \quad (13)$$

3.2 Electric field

The electric fields along the x and y directions can be calculated as

$$\mathrm{E}_x = \frac{(\psi_{i+1,j} - \psi_{i-1,j})}{2L/Nx}$$
$$\mathrm{E}_y = \frac{(\psi_{i,j+1} - \psi_{i,j-1})}{2L/Ny} \quad (14)$$

Where Nx and Ny are the separation of the grid line along the x and y directions. Where E is the field electric given by

$$E = \sqrt{E_x^{\,2} + E_y^{\,2}} \quad (15)$$

These equations are used to calculate the field dependent mobility and drain current equation.

3. RESULTS AND DISCUSSIONS

Computations have been carried out for GaAs MESFET at 300K under Dark and illuminated conditions The gate metallisation has been assumed to be thin enough to allow 90% of the incident radiation to pass through.

The basic 2D Poisson's equation (1) is solved using 2D Poisson equation (1) is solved by finite iterative method (Liebmann iterative method) to determine the potential distribution at every grid point in conductor channel whith applied the approprite condition .

The voltage profile in the channel is divided into large number of elementary strips.

The parameters used in the calculation are shown inTable1

Table1. Simulation table parameters

Parameter	Values
Channel depth, a	0.22μm
Channel length, L	1.2 μm
Channel width, Z	0.4 μm
Absorption coefficient α	25 μm
Minority carrier life time,τ_L	106 /m
Intrinsic carrier concentration,ni	10-8s
Incident optical power, Popt	0.85 v
Reflection coefficient at entrance,Rm	0.2,0.5W/m2
Reflection coefficient at metal contact, Rs	10% of Pop
Position of Fermi level below the conduction band,Δ	0.02 eV
Built-in voltage of Schottky gate, Φbi	0.85 v

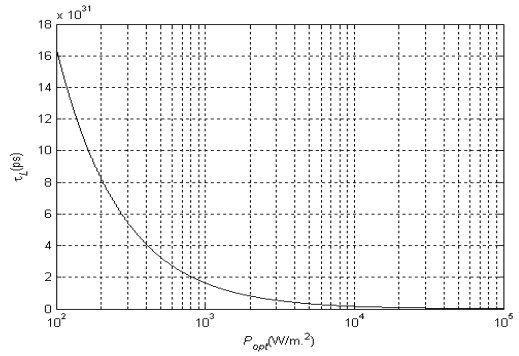

Fig.2. The variation of P_{opt} versus the minority carrier life time,τ_L

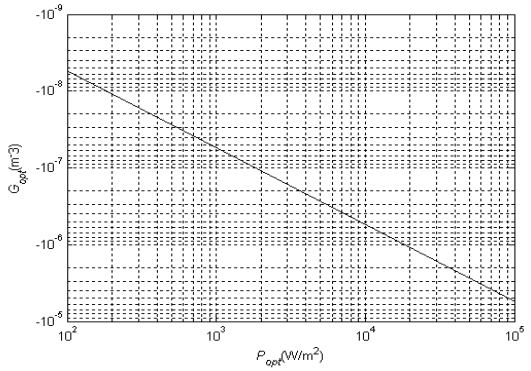

Fig.3. The variation of Incident optical power density P_{opt} versus photovoltage G_{opt}

Fig. 3 shows the increase of photvoltage Gopt with an increase in the incident optical power density ,Popt due to the reduction in lifetime of the carrier in the presence of illumination presented in Fig.2, which limits the excess photogeneration under intense illumination.

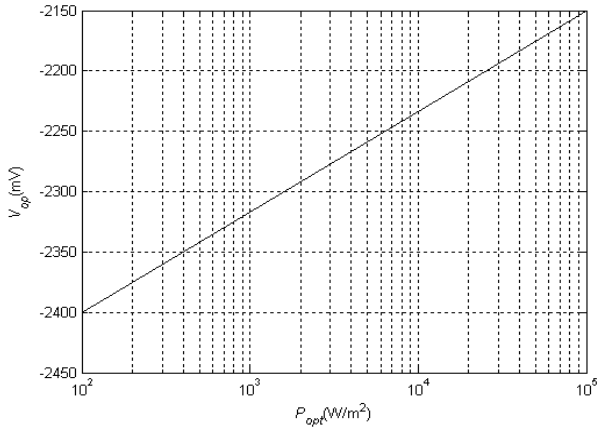

Fig4 shows the variation of the photo voltage V_{op} developed at the Schottky contact with the optical power density P_{opt}.

The Surface recombination has not been taken into account. The photo voltage developed at the Schottky junction increases with the incident optical power density P_{opt}.

The drain to source current Idsop can be written considering its continuity equation as

$$I_{dsop} = \left(Z\mu_n / L \right) \varphi_n(v) E \qquad (16)$$

Where μ_n is the field dependent mobility of carriers, E is the electric field at point (x,y) due to the field E_x and E_y.

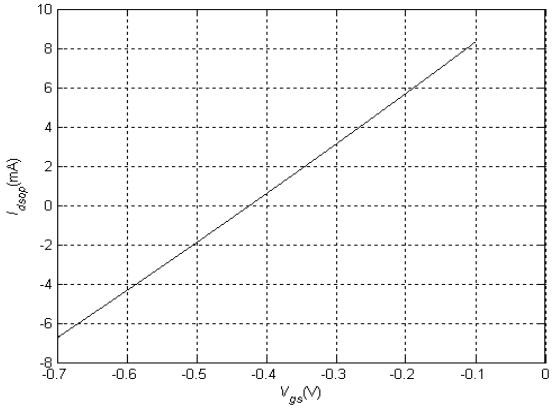

Fig *5* shows the variation drain to source curent Idsop with the Vgs under illumination.

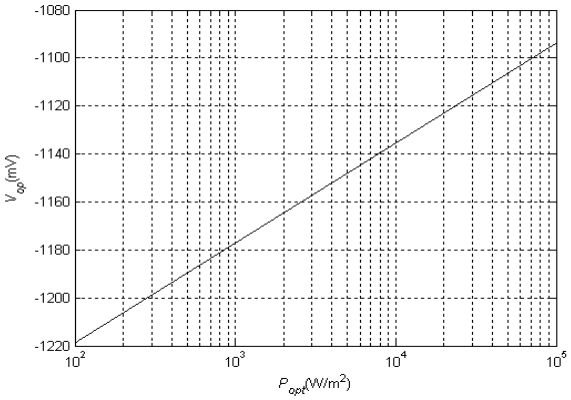

Fig. 6. Variation of the photovoltage Vop across the Schottky barrier with the incident optical power densityPopt.

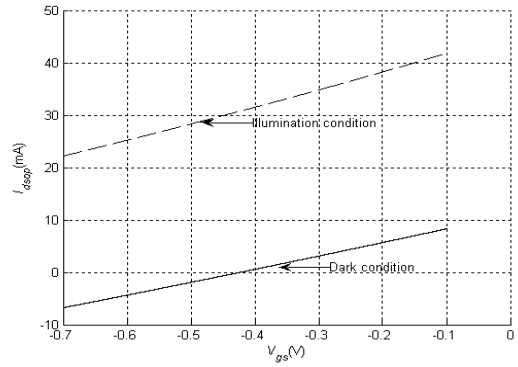

Fig.7. shows the variation drain to source curent Idsop with the Vgs under illumination and dark condition.

The curent Idsop increase with increase of the applied sourse to gate voltage and we observe the excess of Idsop in illumination condition than the dark condition.

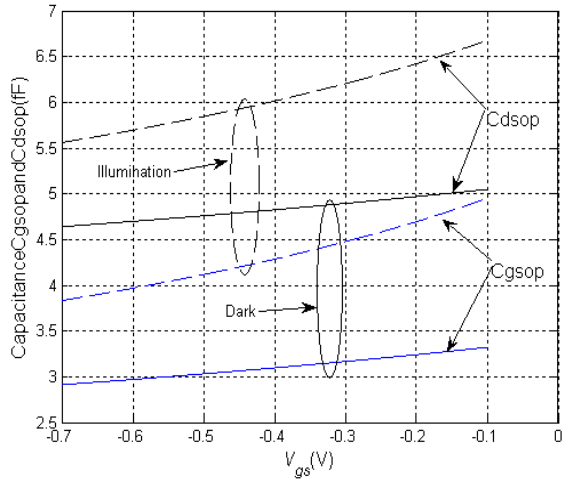

Fig.8 shows the variation of the gate to source capacitance Cgsop and Cdsop with the Vgs for different illumination (Popt1=0W/m2, Popt2=1E5W/m2).

It shows that the capacitance increases slightly with the increase in illumination.

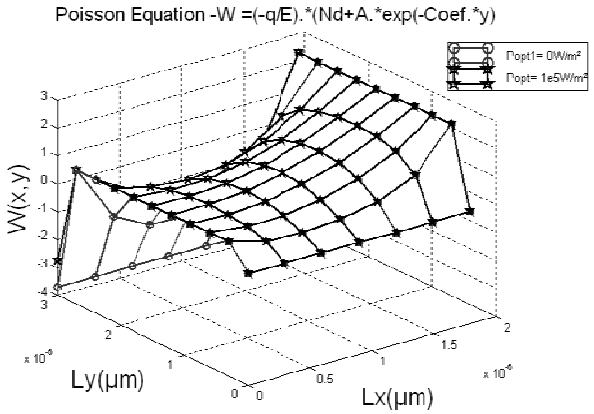

Fig.9 shows the variation of channel potential with Lx andLy for different illumination(Popt1=0W/m^2,Popt2=1E5W/^{2}).

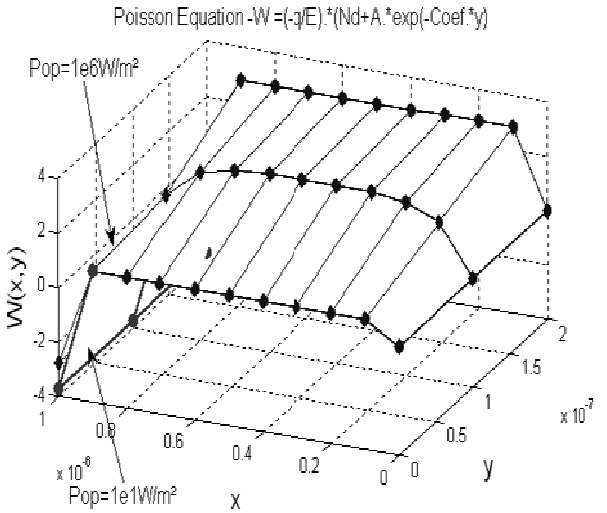

Fig.10 shows the variation of channel potential with Lx andLy for different illumination(Popt1=1E6W/m^2,Popt2=1E 1W/m^2).

It clearly shows that the channel potential increases towards the drain side. This is because the biasing is applied at the drain

The Fig.9 and Fig10 shows the two dimensional potential profile in the channel under dark and illumination conditions.

4. Conclusion

The 2D Poisson's equation is solved numerically for GaAsMESFET photodetector with uniform doping profile. The device characteristics and parameter have been calculated under the dark and illumination conditions. The effect of various internal device parameters such as electric filed, mobility of the carriers in the presence of illumination, potential distribution of the carriers have also been studied extensively through numerical simulation. The drain current and transfer characteristics of the GaAs MESFET photodetector has also been calculated. The present work is limited to modeling and simulation of uniformly doped two dimensional GaAs MESFET photodetectors.

References

[1] Nandita Saha Roy, B.B.Pal and R.U.Khan,, "Frequency dependent characteristics of an ion implanted GaAs MESFET with opaque gate under illumination", Journal of Lightwave Technology, Vol. 18, Issue 2, Feb 2000, pp. 221-229.

[2] M. S. Tyagi, "Introduction to Semiconductor Materials and Devices", New Delhi , 2000.

[3] Madheswaran Muthusamy and Kalaiarasi Kuppusamy, "Numerical simulation of GaAs MESFET photodetector for OEIC receivers", Proc. of SPIE Vol. 5881, 2005.

[4] P. Chakrabarti, N. L.Shrestha, S. Srivastava, and V. Khemba, " An improved model of an ion-implanted OPFET " IEEE Trans.Electron Device,vol. 39,pp. 2050-2059, Sept. 1992.

[5] Shan-Ping Chin and Ching-Yuan Wu, "A New Two-Dimensional Model for the Potential Distribution of Short Gate-Length MESFET's and its Applications" , Journal on Electron Devices,Vol.39, August 1992.

[6] R. B. Darling and J. P. Uyemura, "Optical gain and large signal characteristics of illuminatted GaAs MESFET , " IEEE J. Quantum Electron ,vol. QE-23, pp. 1160-1171, July 1987.

[7] Nandita Saha Roy, B.B. Pal and R.U. Khan, "Analysis of GaAs OPFET with Improved Optical Absorption under Back Illumination", Transactions on Electron Devices, Vol No 46, No 12, December 1999.

Journal of New Technology and Materials
JNTM
Vol. 01, N°00 (2011)63-65

OEB Univ. Publish. Co.

Spin polarized transport in semiconductor

A. Boudine[a], K. Benhizia[b] and L. Kalla[a]
[a]Université Larbi ben M'Hidi, 04000-Oum El Bouaghi, Algérie
[b]Université Mentouri, Route Ain El Bey, Constantine 25017, Algérie
Received: 23 May 2011, accepted: 30 September 2011

Abstract
In this paper, we study two-dimensional spin polarized transport in semiconductors. Based on the some semiclassical considerations and taking account of the spin relaxation. We determined the relationship of the polarization as a function of time and the distance. And we have also established the relationship of the drain current in a 2D channel of a transistor called "spin-FET" where it was matter to highlight this type of transport.

This study was crowned with a numerical study of the characteristics of spinFET 2D transistor depending on the external field and internal characteristics of the semiconductor.
Keywords: Spin polarized transport, spintronic, spinfet, Semiconducteur

1. Introduction

The study of spin-polarized transport across interfaces is a subject of long history [1, 2]. The recent advent of semiconductor-based electronic devices at the nanoscale has revived the interest in transferring, controlling and detecting spin currents. This research area has been termed spintronics due to the exciting possibility of future, successful spin-based electronic technology [3]. Nevertheless, spintronics is interesting as well for fundamental physics, both experimentally and theoretically, as its basic constituent—the spin—is of quantum nature only.

In the ideal situation where spin (or its projection along a direction) is conserved, spin current is simply defined as the difference between the currents of electrons in the two spin states. This concept has served well in early study of spin-dependent transport effects in metals. The ubiquitous presence of spin-orbit coupling inevitably makes the spin non-conserved, but this inconvenience is usually put off by focusing one's attention within the so-called spin relaxation time. In recent years, it has been found that one can make very good use of spin-orbit coupling, realizing electric control of spin generation and transport [3, 4, 5, 6, 7, 8, 9]. The question of how to define the spin current properly in the general situation therefore becomes urgent.

2. Hamiltonian And Theoretical Approaches

In semiconductor spintronic structures, where spin is carried by electrons and/or holes, the spin dynamics is controlled by magnetic interactions. Some of these are surveyed below.

-Interaction with an external magnetic field.

An external magnetic field $\vec{B}$ exerts a torque on a magnetic dipole and the magnetic potential energy is given by Zeeman term

$$U = \frac{g^* \mu_B}{2} \vec{\sigma}.\vec{B} \qquad (1)$$

where g^* is the effective g -factor, and σr represents a vector of the Pauli spin matrices, used in the quantum-mechanical treatment of spin ½, see [10]. The interaction (1) leads to the spin precession around the external magnetic field. This interaction is important in all system where a magnetic field is present. Moreover, fluctuations of $\vec{B}$ could lead to noise contributing to spin relaxation.

-Interaction with magnetic impurities, nuclei and other spin carriers.

An electron located in a semiconductor experiences different kinds of spin-spin interactions including direct dipole-dipole interactions with nuclear spins and other (free and localized) electrons, and the exchange interaction. The latter, in fact, is the result of the electrostatic Coulomb interaction between electrons, which becomes spin-dependent because of the Pauli exclusion principle [10]. Usually, at room temperatures in sufficiently clean, low-doped non-magnetic semiconductors these interactions are not very important.

3. Spin-orbit interaction

The spin-orbit (SO) interaction arises as a result of the magnetic moment of the spin coupling to its orbital degree of freedom. It is actually a relativistic effect, which was first found in the emission spectra of hydrogen. An electron moving in an electric field, sees, in its rest frame, an effective magnetic field. This field, which is dependent on the orbital motion of the electron, interacts with the electron's magnetic moment.

The Hamiltonian describing SO interaction, derived from the four-component Dirac equation [11], has the form

$$H_{SO} = \frac{\hbar^2}{4m^2c^2}\left(\vec{\nabla} \times V\right).\vec{\sigma} \qquad (2)$$

where m is the free electron mass, rp is the momentum operator, and is the gradient of the potential energy, proportional to the electric field acting on the electron. When dealing with crystal structures, the spin orbit interaction, Eq. (2), accounts for symmetry properties of materials. Here we emphasise two specific mechanisms that are considered to be important for spintronics applications. The Dresselhaus spin-orbit interaction [1] appears as a result of the asymmetry present in certain crystal lattices, e.g., the zinc blende structures. For a two-dimensional electron gas in semiconductor heterostructures with an appropriate growth geometry, the Dresselhaus SO interaction is of the form

$$H_D = \frac{\beta}{\hbar}(\sigma_x p_x - \sigma_z p_z). \qquad (3)$$

Here, β is the coupling constant.

The Rashba spin-orbit interaction [13] arises due to the asymmetry associated with the confinement potential and is of interest because of the ability to electrically control the strength of this interaction. The latter is utilized, for instance,

in the Datta-Das spin transistor [13]. The Hamiltonian for the Rashba interaction is written [38] as

$$H_R = \frac{\alpha}{\hbar}(\sigma_x p_z - \sigma_z p_x), \quad (4)$$

where α is the coupling constant. Other possible sources of spin-orbit interaction are non-magnetic impurities, phonons [14], sample inhomogeneity, surfaces and interfaces. In some situations these could play a role in spin transport and spin relaxation dynamics.

Consider the two-dimensional channel of a Spin Field Effect Transistor (SPIN-FET) in the x-z plane with current flowing in thex-direction. An electron's wavevector components in the channel are designated as kx and kz, while the total wavevector is designated as kt. Note that $k_t^2 = k_X^2 + k_Z^2$.

The gate terminal induces an electric field in the y-direction which causes Rashba interaction. The Hamiltonian operator describing an electron in the channel is

$$H = \frac{p_x^2+p_z^2}{2m^*}[\mathbf{I}] + \alpha[V_G](\sigma_x p_z - \sigma_z p_x) \quad (5)$$

where the *p*-s are the momentum operators, the *σ*-s are the Pauli spin matrices and [**I**] is the 2×2 identity matrix. Since this Hamiltonian is invariant in both *x*- and *z*-coordinates, the wavefunctions in the channel are plane wave states $e^{i(k_x x + k_z)}$. Consequently, in the basis of these states, the Hamiltonian is

$$H = \begin{bmatrix} \frac{\hbar^2 k_t^2}{2m^*} + \alpha[V_G]k_x & -\alpha[V_G]k_z \\ -\alpha[V_G]k_z & \frac{\hbar^2 k_t^2}{2m^*} - \alpha[V_G]k_x \end{bmatrix} \quad (6)$$

Diagonalization of this Hamiltonian yields the eigen energies and the eigen-spinors in the two spin-split bands in the two-dimensional channel:

$$\begin{aligned} E_l &= \frac{\hbar^2 k_t^2}{2m^*} - \alpha[V_G]k_t \quad \text{(lower band)} \\ E_u &= \frac{\hbar^2 k_t^2}{2m^*} + \alpha[V_G]k_t \quad \text{(upper band)} \end{aligned} \quad (7)$$

And

$$\begin{aligned} [\Psi]_l &= \begin{bmatrix} sin\theta \\ cos\theta \end{bmatrix} \quad \text{(lower band)} \\ [\Psi]_u &= \begin{bmatrix} sin\theta \\ cos\theta \end{bmatrix} \quad \text{(upper band)} \end{aligned} \quad (8)$$

where $\theta = (1/2)arctan\,(k_z/k_x)$. Note that an electron of energy E has two different wave vectors in the two bands given by $k_t^{(1)}$and $k_t^{(2)}$.

We will assume that the source contact of the SPINFET is polarized in the+*x*-direction and injects +*x*-polarized spins into the channel under a source-to-drain bias. We also assume that the spin injection efficiency at the source is 100%, so that only +*x*-polarized spins are injected at the complete exclusion of −*x*-polarized spins. An injected spin will couple into the two spin eigenstates in the channel. It is as if the x-polarized beam splits into two beams, each corresponding to one of the channel eigenspinors. This will yield:

$$\frac{1}{\sqrt{2}}\begin{bmatrix}1\\1\end{bmatrix} = C_1\begin{bmatrix} sin\theta \\ cos\theta \end{bmatrix} + C_2\begin{bmatrix} -cos\theta \\ sin\theta \end{bmatrix}$$

+*x*- polarized (9)

where the coupling coefficients C_1 and C_2 are found by solving Equation (9).

The result is

$$\begin{aligned} C_1 &= C_1(k_x, k_z) = sin\,(\theta + \pi/4) \\ C_2 &= C_2(k_x, k_z) = -cos\,(\theta + \pi/4) \end{aligned} \quad (10)$$

Note that the coupling coefficients depend on k_x and k_z.

At the drain end, the two beams recombine and interfere to yield the spinor of the electron impinging on the drain. Here, we are neglecting multiple reflection effects between the source and drain contacts in the spirit of ref. [1]. Since the two beams have the same energy *E* and transverse wavevector k_z (these are good quantum numbers in ballistic transport), they must have different longitudinal wavevectors $k_X^{(1)}$and $k_X^{(2)}$ since $k_t^{(1)} \neq k_t^{(2)}$. Therefore, these two beams have slightly different directions of propagation in the channel. In other words, the channel behaves like a "birefrigent" medium where waves with anti-parallel spin polarizations travel in slightly different directions.

Hence, the spinor at the drain end will be:

$$\begin{aligned} &[\Psi]_{drain} = \\ &C_1\begin{bmatrix} sin\theta \\ cos\theta \end{bmatrix} e^{i\left(k_X^{(1)}L + k_z W\right)} + C_2\begin{bmatrix} -cos\theta \\ sin\theta \end{bmatrix} e^{i\left(k_X^{(2)}L + k_z W\right)} \\ &= e^{ik_z W}\begin{bmatrix} sin\left(\theta + \frac{\pi}{4}\right) sin\theta e^{ik_X^{(1)}L} + cos\,(\theta + \pi/4)cos\theta e^{ik_X^{(2)}L} \\ sin\left(\theta + \frac{\pi}{4}\right) cos\theta e^{ik_X^{(1)}L} - cos\,(\theta + \pi/4)sin\theta e^{ik_X^{(2)}L} \end{bmatrix} \end{aligned} \quad (11)$$

Where *L* is the channel length (distance between source and drain contacts) and *W* is the transverse displacement of the electron as it traverses the channel.

Since the drain is polarized in the same orientation as the source, it transmits only +x-polarized spins, so that spin filtering at the drain will yield a transmission probability $|T|^2$ where *T* is the projection of the impinging spinor on the eigenspinor of the drain. It is given by

$$\begin{aligned} \mathrm{T} &= \frac{1}{\sqrt{2}}[1 \quad 1] \times \\ &\begin{bmatrix} sin\left(\theta + \frac{\pi}{4}\right) sin\theta e^{ik_X^{(1)}L} + cos\,(\theta + \pi/4)cos\theta e^{ik_X^{(2)}L} \\ sin\left(\theta + \frac{\pi}{4}\right) cos\theta e^{ik_X^{(1)}L} - cos\,(\theta + \pi/4)sin\theta e^{ik_X^{(2)}L} \end{bmatrix} e^{ik_z W} \\ &= \\ &e^{ik_z W}\left[sin^2\left(\theta + \frac{\pi}{4}\right) e^{ik_X^{(1)}L} + cos^2\,(\theta + \pi/4)cos\theta e^{ik_X^{(2)}L}\right] \end{aligned} \quad (12)$$

Here, we have assumed 100% spin filtering efficiency. Therefore,

$$\begin{aligned} |T|^2 &= cos^4\left(\theta + \frac{\pi}{4}\right)\left|1 + tan^4\left(\theta + \frac{\pi}{4}\right) e^{i\left(k_X^{(1)} - k_X^{(2)}\right)L}\right|^2 \\ &= cos^4\left(\theta + \frac{\pi}{4}\right) + sin^4\left(\theta + \frac{\pi}{4}\right) + \\ &\quad \frac{1}{2}cos(2\theta)cos(\theta L) \end{aligned} \quad (13)$$

where $\Theta = k_X^{(1)} - k_X^{(2)}$.

From Equation (8), we get that:

$$k_t^{(1)} - k_t^{(2)} = -\frac{2m^*\alpha[V_G]}{\hbar^2}$$

Expressing the wavevectors in terms of their *x*- and *z*-components, we get:

$$\Theta = \frac{-\frac{2m^*\alpha[V_G]}{\hbar^2 k_t^{(2)}} + 2(m^*)^2\alpha^2[V_G]/\hbar^4}{\left[k_X^{(1)} - k_X^{(2)}\right]/2} \qquad (14)$$

Now, if $\alpha\,[V_G]$ is small, then $\left[k_X^{(1)} - k_X^{(2)}\right]/2 \approx \sqrt{k_0^2 - k_z^2}$, where $k_0 = \sqrt{2m^*E}/\hbar$. Substituting theseresults in Equation (14), we get

$$\Theta = \frac{-\frac{2m^*\alpha[V_G]\sqrt{2m^*E}}{\hbar^3} - (m^*)^2\alpha^2[V_G]/\hbar^4}{\sqrt{\sqrt{2m^*E}/\hbar^2 - k_z^2}} \qquad (15)$$

The current density in the channel of the SPINFET (assuming ballistic transport) is given by the Tsu-Esaki formula:

$$J = \frac{q}{W_y}\int_0^\infty \frac{1}{h} dE \int \frac{dk_Z}{\pi} |T|^2 [f(E) - F(E + qV_{SD})] \qquad (16)$$

where q is the electronic charge, W_y is the thickness of the channel (in the y-direction), V_{SD} is the source-to-drain bias voltage and $f(\eta)$ is the electron
occupation probability at energy η in the contacts. Since the contacts are at local thermodynamic equilibrium, these probabilities are given by the Fermi-Dirac factor.
In the linear response regime when $V_{SD} \to 0$, the above expression reduces to

$$J = \frac{q^2 V_{SD}}{W_y}\int_0^\infty \frac{1}{h} dE \int \frac{dk_Z}{\pi} |T|^2 \left[-\frac{\partial f(E)}{\partial E}\right] \qquad (17)$$

This yields that the channel conductance G is

$$G = \frac{I_{SD}}{V_{SD}} = \frac{q^2 W_z}{\pi h}\int_0^\infty dE \int dk_Z |T|^2 \left[-\frac{\partial f(E)}{\partial E}\right] (18)$$

we finally get that the channel conductance is

$$G \approx G_0 + \frac{q^2 W_z}{2\pi h}\int_0^\infty dE \int dk_Z \left[1 - \frac{\hbar^2 k_z^2}{2m^*E}\right] cos(\Theta L)\left[-\frac{\partial f(E)}{\partial E}\right] \qquad (19)$$

4. Conclusion

In this work we have studied the transport of two-dimensional spin-polarized, we have established a relation giving the expression of the source-drain current as a function of the parameters of the semiconductor used, and the electric field across the control grid and polarization of injected spins, then we have calculated the associated transconductance G. This model is based on semiclassical consédérations with the holders of spin injected with ballistic trajectories inside the conduction channel.

References

[1] P.M. Tedrow and R. Meservey, Phys. Rev. Lett. 26, 192 (1971).
[2] M. Julliere, Phys. Lett. A 54, 225 (1975).
[3] M.I. Dyakonov and V.I. Perel, JETP 33, 1053 (1971).
[4] J. E. Hirsch, Phys. Rev. Lett. 83, 1834 (1999).
[5] S. Zhang, Phys. Rev. Lett. 85, 393 (2000).
[6] S. Murakami, N. Nagaosa, and S.C. Zhang, Science 301,1348 (2003).
[7] J. Sinova et al., Phys. Rev. Lett. 92, 126603 (2004).
[8] Y.K. Kato et al., Science 306, 1910 (2004).
[9] J. Wunderlich, B. Kaestner, J. Sinova, T. Jungwirth, Phys. Rev. Lett. 94, 047204 (2005).
[10] Landau L.D., and Lifshitz, E.M.: 'Quantum Mechanics' (Butterworth-Heinemann, Oxford, 1997)
[11] Condon, E.U., and Shortley, G.H.: 'The Theory of Atomic Spectra' (Cambridge University Press, Cambridge, 1953)
[12]Dresselhaus, G.: 'Spin-orbit coupling effects in zinc blende structures', Phys.Rev., 1955, 100, pp. 580-586
[13] Bychkov, Yu., and Rashba, E.I.: 'Oscillatory effects and the magnetic susceptibility of carriers in inversion layers', J. Phys. C, 1984, 17, pp. 6039-6045
[14] Gantmakher, V.F., Levinson, Y.B.: 'Carrier scattering in metals and semiconductors' in 'Modern Problems in Condensed Matter Science' v. 19. Series editors Agranovich, V.M., Maradudin, A. A. (North-Holland, New York 1987)

Journal of New Technology and Materials
JNTM
Vol. 01, N°00 (2011)66-68

OEB Univ. Publish. Co.

Toy Model Of Spinfet Transistor

A. Boudine[a], K. Benhizia[b] and N. Djebbari[a]
[a]Université Larbi ben M'Hidi, 04000-Oum El Bouaghi, Algérie
[b]Université Mentouri, Route Ain El Bey, Constantine 25017, Algérie
Received: 23 May 2011, accepted: 30 September 2011

Abstract

The study of spin polarized transport in semiconductors is achieved by the transmission of current in semiconductor devices, our study focuses on spintronics or spin electronics in these devices.

We chose the spinFET transistor or the transistor at `spin rotation' as a better implementation because it is a type of HEMT transistor in which we replace the source and drain by ferromagnetic contacts. The source contact acts as a spin polarizer for electrons injected into the conduction channel of the transistor and the drain contact is a spin analyzer to those (spins) have reached the end of the canal. The drain current varies with orientations of the spin of electrons at the end of the canal and the magnetization of the drain contact. However, it is possible to control the current through the grid voltage.

We have presented a simple toy model in the 1D channel formed in $In_{0,53}Ga_{0,47}As$ a spin FET transistor.

Keywords: Spin polarized transport, spintronic, spinfet, Semiconducteur

1. Introduction

The electrons are not only characterized by their electrical charge, but also by their spin magnetic moment. Up to the late 90's, the electronics had virtually ignored the electron spin (except pauli's law that two electrons can not be in the same energy state with equal spin orientation ..). Since then, spin electronics, or magneto-electronics Prinz [1], grows increasingly and rapidly.In this section we will see how it is possible to introduce the concepts of magneto-electronic components in a semi-conductor.

2. Spintronic

The spin electronics, or "spintronics" Prinz [2], is a new research theme has been booming since the late 80s. The first structures studied in this area are made of ferromagnetic metal multilayers, separated by insulators or "tunnel" or by non-magnetic metal films. Their operating principles are related to a property of ferromagnetic metals on the spin of electrons: they inject or collect preferentially carriers whose spin is polarized along the direction of their magnetic moment. Such devices are already used industrially as magnetic field sensors for read heads of hard disks, or are expected to be soon in the case of magnetic random access memory. During the past four years, groups working in the field of semiconductor components were also interested in properties related to the spin of the electron Bournel,[3]. Indeed, recent studies have shown that it is possible to act on the spin of charge carriers and use this quantity to modify the electrical and optical structures in semiconductors.

3. Spintronics in semiconductors (spin FET)

In semiconductors, the control of the spin of the carriers, in addition to their charges, may give rise to a new generation of electronic devices Wolf et al [4]. This idea was born of a new concept device that can benefit from the manipulation of spin to create a new feature. Is the case of Datta and Das transistor wich we will briefly describe the principle [5]. This concept was proposed in 1990 and named Spin FET "rotation spin transistor". This device looks at first sight to the classical field effect transistor, as illustrated in Figure (I) and has a current source, a drain and a channel with a conductance controllable via a gate voltage, Vg, however, comparison stops there. The spin transistor is based on spin selective contacts, that is to say capable of injecting or collecting a given spin orientation. The injection and the collection of spin-polarized current is carried by ferromagnetic electrodes (Fe, for example). To modulate the drain current, Datta and Das proposed to control the rotation of the "bundle" of spin in the channelusing the spin-orbit Rashba coupling to be a function of voltage applied to the gate [6], The drain current reaches a maximum value when the spin orientation is parallel to the magnetization of the electrodes and injection manifold.

It reaches a minimum value when they are opposed. This concept also implies a transistor coherent transmission, i.g without loss of spin between the injector (source) and collector (drain). Under this proposal, the channel where the propagation of spin takes place must be a gas of electrons in two dimensions (2 DEG) to take advantage of high mobility allowing a coherent propagation. This 2-DEG channel can be obtained in a transistor structure with modulation doping (MODFET) type InGaAs / InAlAs Das et. al. [7].

4. Model and Results

4.1. Drain current variations

The expression of the drain current in a spin-FET in our model is given by the following equation:

$$I_D = q\frac{E_y}{V_C}\mu(E_y)E_x\frac{1+P_0\cos(E_yL/V_R)}{1+P_0} \qquad (1)$$

Where the parameter V_C, equal to $q/(2\varepsilon_0 \varepsilon_{SC} W)$, is uniform to the voltage. It may be noted that the term E_y / V_C in this expression represents the density in the grid controlled by accumulated electrons in the channel. The parameter μ denotes the electron mobility and thus μE_x represents the speed of electrons. The mobility μ varies with the intensity of confinement in the channel, it means with the field E_y the ratio $(1+P_0 \cos(E_y L/V_R))/(1+P_0)$ reflects the analysis of spin at the drain. This ratio varies periodically, with period $E_{y0} = 2\pi V_R / L$. Its amplitude depends on the spin polarization P_0.We initially consider the mobility constant and we study the derivative g of I_D / μ function of E_y.

$$g(u) = \frac{qE_X}{V_C} \frac{1+P_0(\cos(u) - u\sin(u))}{1+P_0} \qquad (2)$$

Where u is a dimensionless parameter equal to $E_y L/V_R$, except in V_C, the function $g(u)$ does not depend on parameters characterizing the quantum wire transistor. The variations of g give the information on the transconductance of the spin-FET

Figure I-Schematic diagram of the transistor with

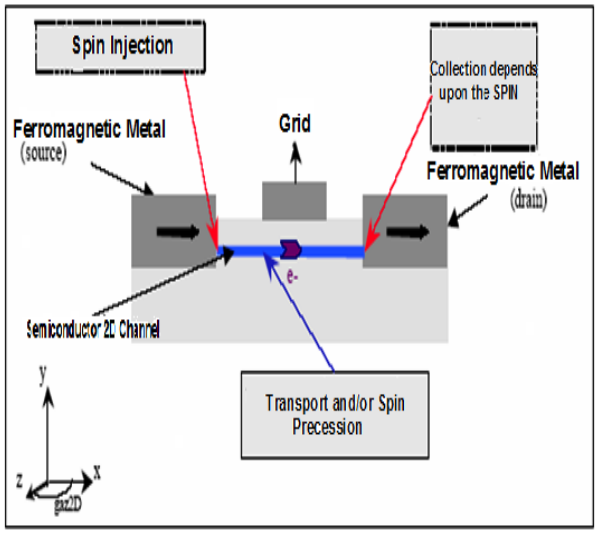

spin precession *(spin- FET)*

In Figure 2 we have represented the variations of the transconductance with the dimensionless parameter $E_y L/V_R$ for P_0 = 80, the spin precession leads to relatively large important electrical effects.

We observe both an important effect of negative transconductance for $E_y L/V_R$ ranging: 400° to 520° the transconductance becomes negative in this area for P_0 equal to 100% in the other hand the transconductance becomes back positive for $E_y L/V_R$ ranging between 540% and 720%. These nonlinear variations of transconductance is related to strong current oscillations.

For values of P_0 = 10%, these effects are never observed in the considered interval for $E_y L/V_R$: the transconductance remains positive. In this case, the amplitude of current oscillations due to modulation of the spin polarization in the perpendicular field is very low.

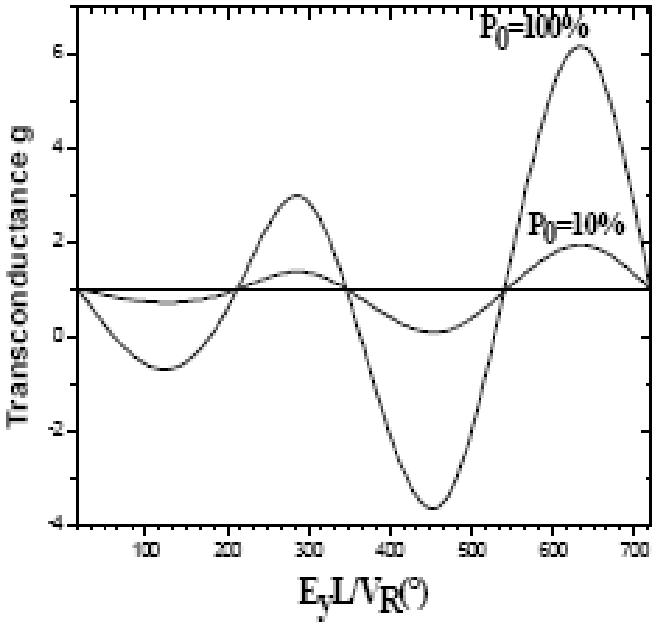

Figure 2 Transconductance g function of dimensionless parameter $E_y L/V_R$ in a spin-FET quantum wire $In_{0.53}Ga_{0.47}As$. For P_0 = 100% and 10%.

5. Conclusion:

In this work we have established a relation giving the expression of the current source-drain as a function of the parameters of the used semiconductor, the potential across the control grid and the polarization of injected spins, then we have calculated the associated transconductance. This model is based on semiclassical consédérations with carriers of spin injected and collected that have ballistic trajectories inside the conduction channel. We have presented here the dependence of the transconductance as a function of spin polarization for a qualitative assessment of the model. we note that the spin-FET offers an interest as a component if the spin polarization P_0 imposed by the ferromagnetic contacts is equal to 100%.

6. References

[1] G. A Prinz, Magnetoelectronics applications, *J. Magn. Magn. Mater.*, Vol. 200, n°1-3, 1999, p. 57-68.

[2] G.A Prinz,, Spin-polarized transport, Phys. Today 48, 58 (1995).

[3] A Bournel, Magnéto électronique dans des dispositifs à semi-conducteurs, *Ann. Phys. Fr*, Vol. 25, n°1, 2000, p. 1-176.

[4] S. A Wolf et al., Spintronics : A Spin-Based Electronics Vision for the future, Science 294, 1488 (2001)

[5] B, D Das. C. and Miller, S. Datta, Evidence for spin splitting in InxGa1-xAs/In0.52Al0.48As heterostructures as B®0, Phys. Rev. B 39 (2), 1411(1989)
[6] E.I. Rashba, Properties of semiconductors with an extremum loop, I/ Cyclotron and combinational resonance in a magnetic field perpendicular to the plane of the loop, Sov. Phys. Solid State 2, 1109 (1960)
[7], S. Datta and B. Das, Electronic analog of the electro - optic modulator, Appl. Phys. Lett, Vol. 56 (7), 665 (199

Journal of New Technology and Materials
JNTM
Vol. 01, N°00 (2011)69-73

OEB Univ. Publish. Co.

Study of the performance of ballistic carbone nanotube FETs

D. Rechem, S. Benkara, K. Lamamra
Sciences and technology department, Sciences and the technologies faculty, Larbi Ben M'hidi University, Oum El Bouaghi, Algeria, E-mail: Rechem_dj@yahoo.fr
Received: 23 May 2011, accepted: 30 September 2011

Abstract
Using a two-dimensional (2-D) simulation, we study the impact of varying the nanotube diameter and gate oxide thickness on the performance of a ballistic nanoscale carbon nanotube field effect transistor (CNTFET). Our results show that the nanotube diameter influences the I_{ON}/I_{OFF} current ratio; the drain induced barrier lowering (DIBL), the subthreshold slop as well as transconductance and drain conductance. We also show that these device characteristics are affected by the gate oxide thickness. Thus, nanotube diameter and gate oxide thickness must be carefully taken into account when designing robust logic circuits based on CNTFETs with potentially high parameter variability.
Keywords: *Carbon nanotube; Field- effect transistor; Ballistic; Carbon nanotube diameter; Gate oxide thickness.*

1. Introduction

Since the first reports of single-walled carbon nanotubes (CNTs) in 1993 [1, 2], they have been the subject of intense interest for basic and applied research. In particular, single-walled carbon nanotube (SWCNT) field-effect transistor (CNTFET) is considered as one of the most promising candidates for enhancing functionality of silicon based complementary metal-oxide-semiconductor (CMOS) circuits and extending Moore's Law [3-6].
Due to the small diameter, thin high-k gate insulator, and a good S/D metal contact, the CNTFET demonstrates the best performance to date. Recently, CNTFETs have been fabricated successfully [7–9]. It has been reported that they have shown better performance than present silicon transistors with the equivalent sizes. They are particularly attractive for high-speed applications due to their quasi-ballistic properties and high Fermi velocity (10^6 m/s) [10-11]. Rapid progress in the field has recently made it possible to fabricate digital and analogue CNTFET-bases circuits, such as logic gate, static memory cells and ring oscillators [12, 13].
In this paper, we will discuss the role of nanotube diameter and gate dielectric thickness on the performance of CNTFETs over wide range by reference to I_{ON}/I_{OFF} current ratio, subthreshold slope, the drain induced barrier lowering (DIBL) as well as transconductance and drain conductance using a two-dimensional (2-D) simulation. Because to explore the role of CNTFETs in future integrated circuits, it is important to evaluate their performance and the nanotube diameter and gate dielectric thickness have direct relevance for the electrostatic control in a CNTFET.

2. Simulated device

The modeled device, a coaxially gate, n-type CNTFET is schematically shown in figures 1(a) and 1(b). The nanotube length is 50 nm, consisting of ~1.2×10^4 carbon atoms. The intrinsic channel length is 20 nm, and the doped source/drain length is 15 nm.
To simulate the behavior of a CNTFET, the following model is used at different nanotube diameters and gate oxide thicknesses. The chiralities of the CNTs used are (13,0), (16,0), (19,0), (23,0), (25,0). In addition the gate oxide thicknesses (tox) used are 1.5 nm, 3 nm, 4.5 nm, 6 nm and 7 nm. The high-k gate dielectric is fixed at k=16, correspond to the dielectric constant reported for HfO_2.
For our simulations, we assume that the metal-nanotube contact resistance, R_c = 0, and carrier transport through nanotube is ballistic (no scattering). No gate-to-source or gate-to-drain overlap is assumed. The applied drain (V_{DS}) and gate (V_{GS}) biases vary from 0 V to 1. All calculations have been done at room temperature (T = 300 K).

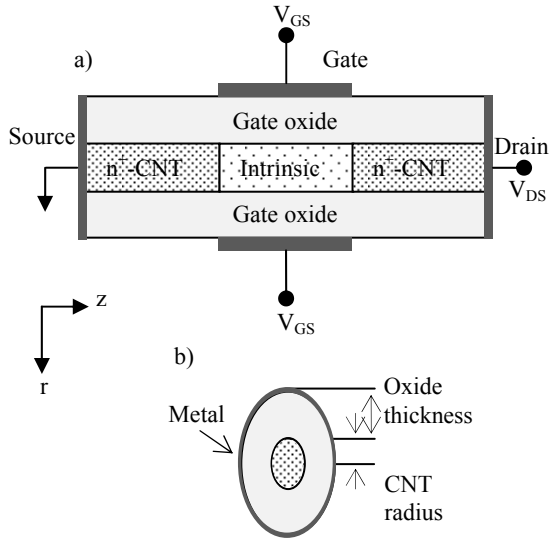

Figure 1. Schematic diagrams of the modeled, coaxially CNTFET.

3. Model:

Many models have been proposed for simulating the characteristics of CNFETs [14,15]. The specific model chosen for this study is based on capacitance model [15], as shown in Fig. 2.
The circuit diagram in Fig. 2 shows the simple model that represents the potential at the top of the barrier when taking into account the effect of the three terminals (source, drain, and gate).

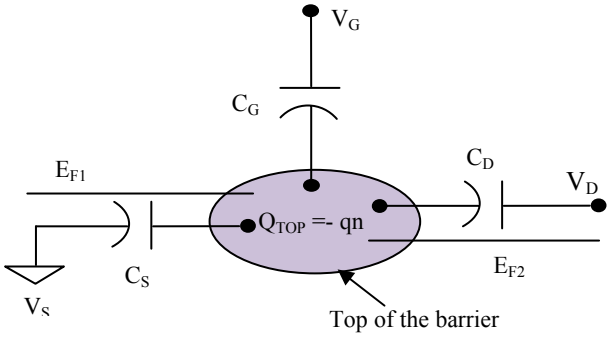

Figure 2. Two dimensional circuit model for ballistic transistors.

The mobile charge is represented by the shaded region in Fig. 2 and is determined by the combination of the local density of states at the top of the barrier, the location of the source and drain Fermi levels, E_{F1} and E_{F2}, and by the self-consistent potential at the top of the barrier, Uscf.

When the terminal biases are zero, the equilibrium electron density at the top of the barrier is:

$$n_0 = \int_{-\infty}^{+\infty} D(E) f(E - E_F)\, dE \qquad (1)$$

Where D(E) is the local density of states at the top of the barrier, and f(E-E_F) is the equilibrium Fermi function. When a bias is applied to the gate and drain terminals the self-consistent potential at the top of the barrier becomes Uscf, and the states at the top of the barrier are now populated by two different Fermi levels. The positive velocity states are filled by the source, according to:

$$n_{1=} \frac{1}{2} \int_{-\infty}^{+\infty} D\big(E - U_{scf}\big) f(E - E_{F1})\, dE \qquad (2a)$$

and the negative velocity states are filled by the drain according to:

$$n_{2=} \frac{1}{2} \int_{-\infty}^{+\infty} D\big(E - U_{scf}\big) f(E - E_{F2}) dE \qquad (2b)$$

Where, $E_{F1} = E_F$, and $E_{F2} = E_F - qV_{DS}$ [2]. A change of variables can be used to re-express these equations as:

$$n_{1=} \frac{1}{2} \int_{-\infty}^{+\infty} D(E) f_1(E) dE \qquad (3a)$$

$$n_2 = \frac{1}{2} \int_{-\infty}^{+\infty} D(E) f_2(E) dE \qquad (3b)$$

Where

$$f_1(E) \equiv f\big(E + U_{scf} - E_{F1}\big) \qquad (4a)$$

and

$$f_2(E) \equiv f\big(E + U_{scf} - E_{F2}\big) \qquad (4b)$$

With eq. (3), the total electron density at the top of the barrier is $n = n_1 + n_2$, and can be determined if the arbitrary density of states, *D(E)*, the source and drain Fermi levels, and the self-consistent potential, Uscf, are known.
The self-consistent potential is determined by solving the two-dimensional Poisson equation as represented by the 2D model in Fig. 2 with the common terminal evaluated at the bias induced charge, $\Delta n = (n_1 + n_2) - n_0$. Ignoring mobile charge in the channel, the Laplace potential at the top of the barrier is then:

$$U_L = -q(\alpha_G V_G + \alpha_D V_D + \alpha_S V_S) \qquad (5)$$

In this equation (5), the three α's describe how the gate, drain, and source control the Laplace solution [2] and are given by:

$$\alpha_G = \frac{C_G}{C_T} \quad \alpha_D = \frac{C_D}{C_T} \quad \alpha_S = \frac{C_S}{C_T} \qquad (6)$$

Where C_T is defined as the parallel combination of the three capacitors in Fig. 2.
For an optimally constructed MOSFET, the gate controls the potential in the channel which means that $\alpha_G \approx 1$ and, α_S, $\alpha_D \approx 0$. The model is completed by taking into account the effect on the potential at the top of the barrier due to mobile charge with:

$$U_P = \frac{q^2}{C_T} \Delta n \qquad (7)$$

Therefore, U_{scf} is equal to:

$$U_{scf} = U_L + U_P = -q(\alpha_G V_G + \alpha_D V_D + \alpha_S V_S) + \frac{q^2}{C_T} \Delta n \qquad (8)$$

Equations (2) and (8) represent two coupled nonlinear equations for the two unknowns n and U_{scf}. These equations can be solved iteratively to find the carrier density and self-consistent potential at the top of the barrier. Finally, the drain current is evaluated from:

$$I_D = \int_{-\infty}^{+\infty} J\big(E - U_{scf}\big)[f(E - E_{F1}) - f(E - E_{F2})] dE \qquad (9a)$$

Where J(E-Uscf) is the "current-density-of-states", which is expressed as:

$$J\big(E - U_{scf}\big) = \frac{1}{2} q \left(\frac{2}{\pi} \sqrt{\frac{2(E - U_{scf})}{m^*}} \right) D\big(E - U_{scf}\big) \qquad (9b)$$

4. Results and discussion:

4.1. Investigation of effect of nanotube diameter:

In this section, the gate oxide thickness is fixed at 1.5nm and high-k gate dielectric is fixed at k=16, while the nanotube diameter (d) is varied. Figure 3 presents the I_{ON}/I_{OFF}

current ratio as a function of the nanotube diameter. I_{ON} is obtained at V_{GS} = 1 V and V_{DS} = 1 V, I_{OFF} is defined as the current obtained for V_{GS} = 0 V and V_{DS} = 1 V. It can be observed that I_{ON}/I_{OFF} ratio is improved with increase in the nanotube diameter. This comes from the correlation of the band-structure with the CNT diameter. Using a larger diameter reduces the bandgap, therefore both the ON-current and the leakage current I_{OFF} increase, and I_{ON} increases rapidly. Thus a significant increase of the I_{ON}/I_{OFF} ration is observed when the nanaotube diameter is increases. So this point must be carefully taken into account to obtain the best electrical characteristics in perspective to build reliable logic circuits based on CNTFETs.

For short channel devices, application of a high drain-to-source bias can shorten the threshold voltage and increase the off-currents. This is known as drain induced barrier lowering (DIBL). In CNTFETs, the DIBL effect is still a primitive problem and open for further study [16].

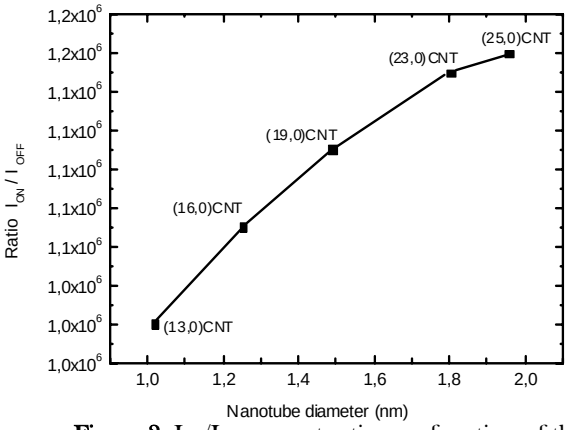

Figure 3. I_{ON}/I_{OFF} current ratio as a function of the nanotube diameter

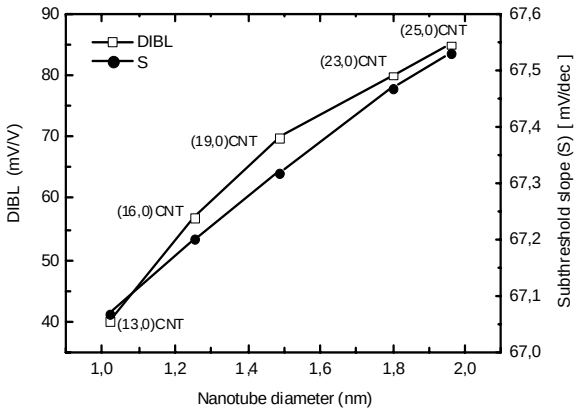

Figure 4. Drain induced barrier lowering (DIBL) and subthreshold slop versus nanotube diameter.

Figure 4 shows the effect of varying the nanotube diameter on the DIBL. The DIBL is accessed using the classical expression [17].

$$\mathrm{DIBL} = \frac{V_{TH}(\mathrm{Low}\ V_{DS}) - V_{TH}(\mathrm{High}\ V_{DS})}{\mathrm{High}\ V_{DS} - \mathrm{Low}\ V_{DS}} \qquad (10)$$

From the simulation results, it can be drawn that the DIBL is considerably improved with decreasing d; therefore, the control of gate on the channel becomes stronger. One notes a reduction around 53% of DIBL when CNT chiralities varying from (13, 0) CNT to (25, 0) CNT.

Another important parameter characterizing the short channel performance is the subthreshold slope (S). A small subthreshold slope is desired for low threshold voltage and low-power operation for FETs scaled down to small sizen. Figure 4 represents the evolution of subthreshold slope as a function of the nanotube diameter (d) for V_{DS} = 1 V. It can be observed that when the nanotube diameter decreases, S decreases slightly (practically remains constant around 67 mV/decade).

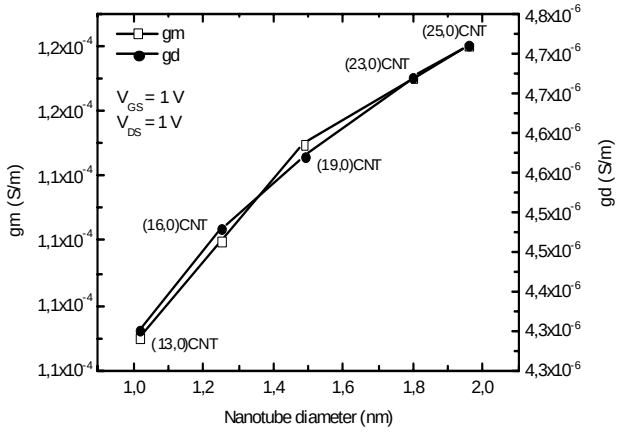

Figure 5. Variation of g_m and g_d at V_{DS}=1 V and V_{GS}=1 V as a function of nanotube diameter.

The transconductance, an important device parameter, is defined as measure of device gain and is directly related to the circuit speed. The transconductance gm curve is obtained by differentiating the drain current I_{DS} with respect to the gate voltage V_{GS} at a given drain bias $g_m=\partial I_{DS}/\partial V_{GS}$ [18]. As can be seen from Fig. 5, when the nanotube diameter increases the transconductance gm, increases. The drain conductance defined by $g_d=\partial I_{DS}/\partial V_{DS}$. Figure 5 also shows the variation of drain conductance gd, in saturation, for different values of d in a CNTFET. It is observed that gd is higher for larger d. One notes a voltage gain gm/gd around ~25 whatever the value of nanotube diameter d is.

4.2 Investigation of effect of gate dielectric thickness:

The I_{ON}/I_{OFF} current ratio of the CNTFETs with gate oxide thickness (t_{ox}) varying from 1,5 nm to 7nm are compared in Figure 6. I_{ON} is measured at V_{DS}= 1V and V_{GS}=1V, I_{OFF} defined as the current obtained for V_{DS} =1V and V_{GS}=0V.

It can be seen from the figure that with decreasing of t_{ox}, the I_{ON}/I_{OFF} ratio increases and lead to a high on- state current. This is associated with superior control of the gate voltage over the channel, which helps in reducing the off- state current.

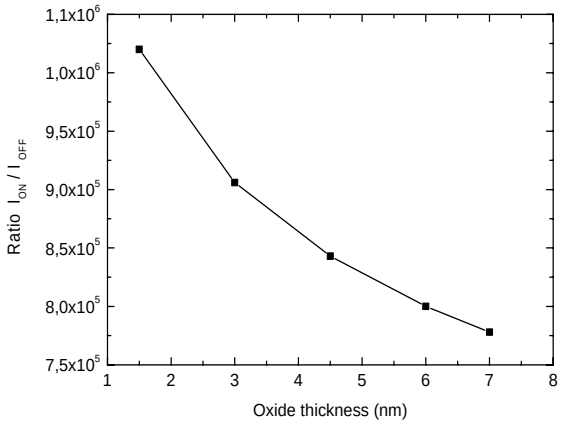

Figure 6. I_{ON}/I_{OFF} current ratio as a function of the oxide thickness

As can be seen from Figure 7 when t_{ox} decreases, the DIBL decreases. It is evident that the DIBL of device improves with decrease in t_{ox}. There for the control of gate on the channel becomes stronger.
Subthreshold slope is an important factor that increases the standby power dissipation in CMOS circuits.

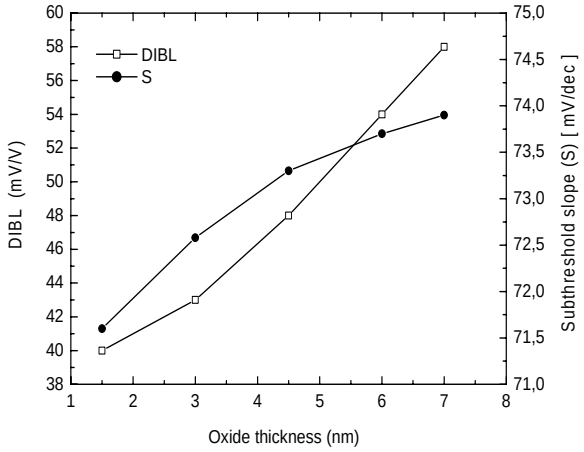

Figure 7. Drain induced barrier lowering (DIBL) and subthreshold slop versus oxide thickness.

A small subthreshold slope (S) is also desired for low threshold voltage for FETs scaled down to small size [19]. The lowest theoretical limit for S is: $S= (K_BT/q)\ln(10) \cong 60$ mV/decade at room temperature.

Figure 7 shows that the subthreshold swing decreases with decreasing (t_{ox}).

As shown in Figure 8, it is seen that as gate dielectric thickness (t_{ox}) increases the drain conductance, gd, and transconductance gm, continues to decrease.

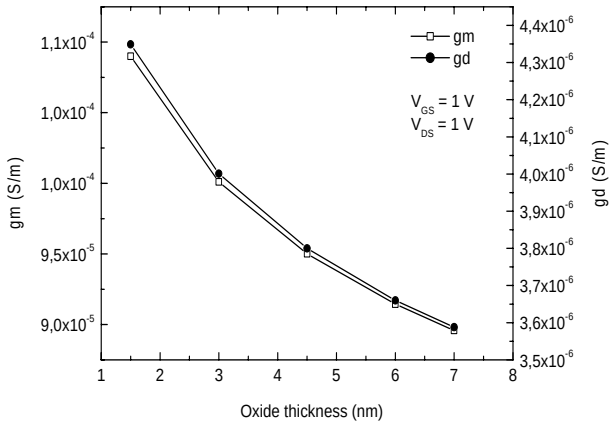

Figure 8. Variation of g_m and g_d at V_{DS}=1 V and V_{GS}=1 V as a function of oxide thickness

5. Conclusion

We implement a two- dimensional model to explore the behavior of a CNTFET at different nanotube diameters and gate oxide thickness.
Based on the I_{ON}/I_{OFF} current ratio, drain –induced barrier lowering (DIBL), subthreshold slope, transconductance and out conductance variation with different carbon nanotube (CNT) diameters and gate oxide thickness, the CNTFET behavior is evaluated.
We concluded that using large CNT diameter and thinner gate oxide are caused by the enhancement in on-state current, transconductance and out conductance. In addition, off-state current, DIBL and subthreshold slope improve in CNTFETs with thinner gate oxide, but they become worse in CNTFETs with large nanotube diameter.

References:

[1] S. Iijima, T. Ichihashi, "Single-shell carbon nanotubes of 1-nm diameter", Nature., 363 (1993) 603-605.
[2] D. S. Bethune, C. H. Kiang, M. S. Devries, G.Gorman, R. Savoy, J. Vazquez, R. Beyers, "Cobalt-catalyzed growth of carbon nanotubes with single-atomic-layer walls" Nature., 363 (1993) 605-607.
[3] International Technology Roadmap for Semiconductors (2007 Edition), http://public.itrs.net/.
[4] S. Tans, A. Verschueren, C. Dekker, Nature., 393 (1998) 49.
[5] H. J. Dai, A. Javey, E. Pop, D. Mann, Y. Lu, NANO., 1 (2006) 1.
[6] Ph. Avouris, Phys. World., 20 (2007) 40.
[7] J. Guo, A. Javey, H. Dai, M. Lundstrom, "Performance analysis and design optimization of near ballistic carbon nanotube field-effect transistors", IEEE Trans Electron Dev (2004) 703–706.
[8] H. Ohnaka, Y. Kojima, S. Kishimoto, Y. Ohno, T. Mizutani , "Fabrication of carbon nanotube field effect transistors using plasma-enhanced chemical vapor

deposition grown nanotubes", Jpn J Appl Phys., 45 (2006) 5485–5489.
[9] J. Li, Q. Zhang, Y. Yan, S. Li, L. Chen, "Fabrication of carbon nanotube field-effect transistors by fluidic alignment technique", IEEE Trans Nanotechnol., 6 (2007) 481–484.
[10] S. J. Wind, J. Appenzeller, P. Avouris, "Lateral scaling in carbon nanotube field-effect transistors", Phys. Rev. Lett., 91 (2003) 058–301.
[11] Y. Park, S. Rosenblatt, Y. Yaish, V. Sazonova, H. Ustunel, S. Brag, T. A. Arias, P.W. Brouwer, P. L. McEuen, "Electron–phonon scattering in metallic single-walled carbon nanotubes", Nano Lett., 4 (2004) 517–520.
[12] W. Liang, M. Bockrath, D. Bozovic, J. H. Hafner, M. Tinkham, H. Park, F. Perot, "Interference in a nanotube electron waveguide" Nature., 411 (2001) 665–669.
[13] V. Derycke, R. Martel, J. Appenzeller, Ph Avouris, "Carbon nanotube inter-and intramolecular logic gates", Nano Lett., 9 (2001) 453–456.
[14] A. Bachtold, P. Hadley, T. Nakanishi, C. Dekker, "Logic circuits with carbon nanotube transistors", Science., 294 (2001) 1317–1320.
[15] K. Natori, "Ballistic metal-oxide-semiconductor field effect transistors", J App Phys., 76 (1994) 4879-4890.
[16] A. Rahman, J. Guo, S. Datta, IEEE Trans. Electron Devices., 50 (2003) 1853.
[17] M.A. Pavanello, J.A. Martino, E. Simoen, C. Claeys, "Analysis of temperature-induced saturation threshold voltage degradation in deep-submicrometer ultrathin SOI MOSFETs," IEEE Trans. Electron Devices 52 (2005) 2236–2242.
[18] R.S. Muller, T.I. Kamins, "Device Electronics for Integrated Circuits", Wiley, New York (1986).
[19] S.M. Sze, "Physics of Semiconductor Devices", Wiley, New York (1981).

Journal of New Technology and Materials
JNTM
Vol. 01, N°00 (2011)74-78

OEB Univ. Publish. Co.

Optical and structural study of plastic deformation of single crystals CdTe and CdZnTe

S. Harouni* k. Guergouri L. Arabe and S. Hamdellou
Laboratoire Physique-Chimie des Semiconducteurs (LPCS), Département de Physique, Université Mentouri, Universite mentouri, 25000 constantine, Algerie.
**E-mail Sof.harouni@gmail.com*
Received: 23 May 2011, accepted: 30 September 2011

Abstract
CdTe pure and alloyed with some isoelectronic impurities was found in front of more than twenty years as very promising in optoelectronics. The effectiveness of components based on these materials is strictly related to their quality. It is in this context that our work. The objective in this study is to see the effect of plastic deformation of crystals of CdTe and CdZnTe on crystallographic and optical properties. The investigation methods are X-rays as a means of crystallographic characterization, measurements of UV-Visible spectrophotometry, as means of optical characterization. The main results show that: the best crystal (CdZnTe) before deformation, which shows the highest dislocation density after deformation and increased optical gap, which decreases for CdTe. The effect of dislocations on the optical properties is characterized by a shift of the absorption edge relative to the undeformed state, due to the creation of acceptor centers, which are the neutral hole CdTe and Cd decreased concentration of Zn atoms substituting Cd atoms

Keywords: *single crystals, CdTe, CdZnTe, plastic deformation, dislocations, optical gap, UV-visible.*

1. Introduction :

II-VI semiconductors are materials composed of elements from columns II and VI of the periodic table. In this family, CdTe is the most recommended [1], because of its properties enabling it to detect X and γ [5], and in the field of infra-red, and its use in medical imaging [2,3] and also serves as a substrate for epitaxial infrared detector CdHgTe [4]. CdTe is a direct gap semiconductor, its band structure [6], enables vertical radiative transitions between the valence band and the conduction band. It has a wide band gap of about 1.51eV at room temperature, which is optimal for junction solar efficiency [7]. The cadmium telluride are used to conduct basic physical studies using two characteristics that make them more susceptible to external shocks:

(i) the binding energy of the exciton oscillator strength and are large, allowing thin optical studies.

(ii) we can insert elements in the matrix without inducing electrical change, such as Zn, Mn and Hg

Despite efforts to improve the crystalline quality of CdTe, this one still has a density of defects, from physical or chemical considerable. This has prompted researchers to turn to the CdZnTe alloy that provides better crystal quality. An examination of the peculiarities of the electrical behavior, related to the presence of a field of microstrain by dislocations is essential in improving the properties of semiconductors.

All properties of crystals depend in one way or another, the type and density of dislocations, their electronic states and their interactions with other types of defects. In some cases, the influence of dislocations of different types can even be contradictory. It happens to not be able to specify which of the dislocation affects the spectrum of electronic states. To resolve this problem, attention has focused in recent years, using samples with a controlled distribution of dislocations monotypes, study local variations of physical properties of the crystal under the action of individual dislocations. In semiconductors under the influence of dislocations, the mobility of current carriers can vary considerably, and their concentration, causing changes in electrical and optical properties of these materials.

These changes are manifested by the appearance of energy levels quite new and even areas or by varying the width of the band gap, caused by the dislocation strain field.

2. Experementale

2.1 Difraction X-ray (XRD)

The X-ray diffraction (XRD) allows qualitative and quantitative analysis of the material to the condensed state.

The shape of the diffraction peaks can be related to the crystalline microstructure. Knowledge of the positions of diffraction peaks and intensities of diffracted beams allow the identification of phases present, the measurement of residual stresses, the lattice parameter, grain size and the study of textures. Analyses of X-ray diffraction were performed using a Siemens D5000 diffractometer. The source used is a copper anticathode operating under a power of 1200 W (30 kV and 40 mA).

2.2 Optical spectroscopy ultraviolet-visible

In this section we will define the coefficient of optical transmittance and give its physical meaning, as we will describe the method of determining the optical gap Eg of the material [8].

2.2.1 The transmittance spectra

The transmission coefficient, or transmittance T, is defined as the ratio of the transmitted light intensity to the intensity of incident light [9].

For the transmittance curves, our samples of CdTe were deposited on glass substrates. These are essential, because it does not absorb light in the spectral range studied. A substrate blank in the reference beam spectrophotometer was used. For plotting the spectra, a computer connected to this unit reproduces the spectra representing the transmittance function of the wavelength of the incident beam.

2.2.2 Absorption Spectra

To determine the absorption coefficient (α), we used the relation of Bouguer-Lambert-Beer or often simply called, Beer's law [10]:

$$T = e^{-\alpha.d} \quad (1)$$

If one expresses the transmittance T (%), the absorption coefficient is given by:

$$\alpha = \frac{1}{d}\ln\left(\frac{100}{T(\%)}\right) \quad (2)$$

Knowing the thickness of the layer, d, so we can determine the absorption coefficient for each transmittance value which corresponds to an energy. By scanning the entire field of energy, we plotted the variation of absorption coefficient as a function of incident photon energy (hν), an example is shown in Fig.1.

2.2.3 Determination of the width of band tail

We carried on a semi-logarithmic variation of absorption coefficient as a function of photon energy. In this region, called the Urbach region, the absorption coefficient can be expressed by the following equation[11].

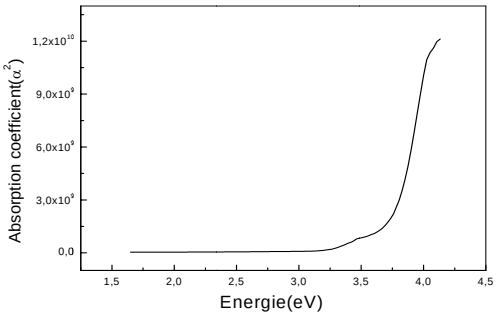

Fig.1 Variation of absorption coefficient

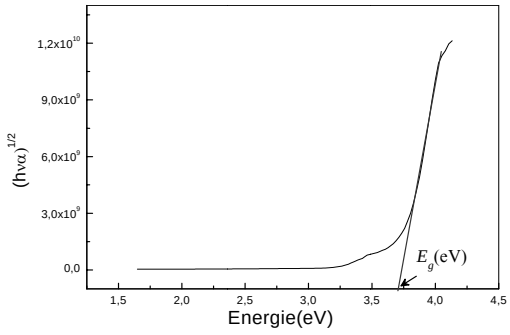

Fig.2 Determination of the energy gap by the extrapolation method from the variation of (αhν) 1/2 as a function of hν.

$$\alpha = \alpha_0.\exp\left(h\nu / E_{00}\right) \quad (3)$$

By calculating logarithmic slope, $1/E_{00}$ in this region, we were able to evaluate the disorder of the film E_{00}, using the inverse of the slope.

2.2.4 Determination of the optical absorption threshold

In the area of high absorption (α> 104cm^{-1}), the relationship between the absorption coefficient α to the photon energy is:

$$(\alpha.h\nu)^{1/2} = B(h\nu - E_g) \quad (4)$$

Where B is a constant and Eg defines the threshold for optical absorption [11,12]. The graphical representation of $(\alpha.h\nu)^{1/2}$ a function of energy (Fig. 2) represents a linear part, whose intersection with the axis of energy gives the optical gap Eg.

2.2.5 Working Principle

The optical absorption measurements were conducted at the University of Constantine. We use a tungsten filament lamp (50W) as a white source, that is to say that emit light in a wide range of wavelengths covering the entire spectrum, visible. This light is first filtered by two specially diaphragms, then made parallel by placing the source at the focus of a converging lens. The light transmitted through the sample is spectrally dispersed by the network, then passes through a monochromator and is then detected by a photomultiplier. Measurements are performed at room temperature.

3. Result and discuss

3. 1. Determination of slip systems

3. 1. 1. Identification of slip system

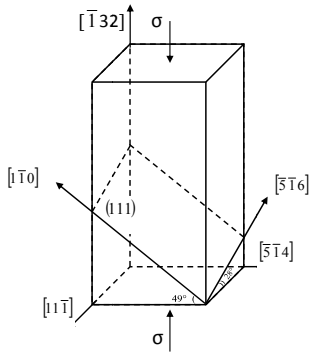

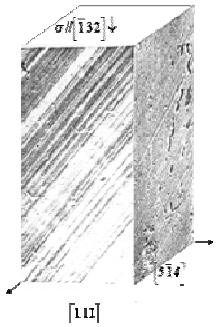

Fig.3 (left): Crystallographic orientations
Fig.4 (right): Images obtained by light microscopy of slip system generated

The specimens for plastic deformation are oriented in such a way as to enable an easy slip system, that is to say having the largest Schmid factor (Fig. 3.a).

For the system with a diamond structure (zinc blende in our case) the slip system in question is the primary system [$\bar{1}$ 10] (111), single system activated under the stress of the stress σ//($\bar{1}$ 32).

For this slip system Schmid factor is 0.47, Figure 3(a and b) shows the crystallographic orientations and the images obtained by light microscopy of slip system generated.

3. 1. 2 determining the Burgers vector

The slip plane in the case of cubic diamond (111), it is generated by perfect dislocations with the Burgers vectors $\frac{a}{2}[110]$. [13]

The system [$\bar{1}$ 10] (111) is generated from corners dislocation characterized by Burgers vector absolute value of the surrounding 4.56Å (Tab.1).

Tab.1: Some parameters of studied samples

Sample	a (Å)	$\|\vec{b}\|$ (Å)
CdTe Deformed	6,459	4,567
CdZnTe Deformed	6,465	4,571

3. 1. 3 Calculation of dislocation density

3.1. 3. 1 width at half maximum of the diffraction peaks and defect density

Much work has been devoted to the study of work-hardened metals. It is possible to link the characteristics of the reflection profile, line width, asymmetry, peak position, size of diffracting domains, density, nature, the width of stacking faults etc. It is a difficult study because the observed effects arise in general from several sources: the line broadening, for example, is due both to the effect size (average size of diffracting domains) and the distorting within areas (presence of stacking faults, etc. ...) [14].

An interesting attempt to link the density of dislocations in the line width was made by P. Gay, P. B. Hirsch and A. Kelly [15]: they interpret the mosaic structure, considering it consists of sub-grains separated by walls of edge dislocations. The angle between two adjacent sub-grains depends on the number of dislocations in the wall and its sign depends on that of dislocations. P. Gay et al assume that the distribution of blocks around a mean position is a Gaussian distribution and consider that the width at half maximum β of reflection profile of this crystal mosaic is equal to the angular width at half height of distribution curve of the small blocks.

From these assumptions, they connect to the β dislocation density

$$\eta_D = \frac{\beta^2}{9b^2} \qquad (5)$$

Where b is the Burgers vector of dislocations. Width β can be deduced from reflection profile recorded using the X-ray diffraction mounting.

Although the quantitative point of view (that is to say the exact determination of the density of dislocations) XRD is not as effective as the method that uses chemical attack bites it remains essential to give a first ruling on the crystalline quality of the crystal to be analyzed.

3. 1. 3. 2 Comparison with experiment

The densities of dislocations before deformation densities are in fact calculated by etching on samples not deformed, where we notice some difference between the three types of samples (Tab.2). We note in particular that the CdTe sample with 4% Zn has a dislocation density less than that observed in pure CdTe.

Tab. 2: Dislocation densities before and after deformation

Sample	$\eta_D (cm^{-2})$ Before def	$\eta_D (cm^{-2})$ After def	$\Delta\eta_D (cm^{-2})$
CdTe	5.10^5	$1,71.10^8$	$1,71.10^8$
CdZnTe	8.10^4	$3,57.10^8$	$3,57.10^8$

3.1.4 Effect of impurity (Zn)

3.1.4.1 Effect on the lattice parameter

The introduction of impurities in the CdTe matrix leads to the variation of lattice parameter, which follows Vegard's law for the whole area of concentration in regard to the Zn impurity (Fig.5)

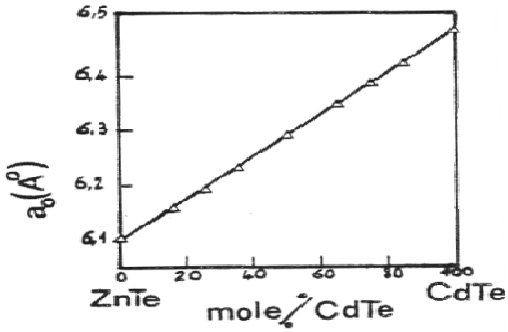

Fig.5 [16]

Tab. 3: XRD results

Sample	2θ(°)	(h k l)	a (Å)	Δa (Å)
C4 not def	23.90	(111)	6,443	0.016
C4 def	23.84	(111)	6,459	
C6 not def	23.98	(111)	6,422	0.043
C6 def	23.82	(111)	6,465	

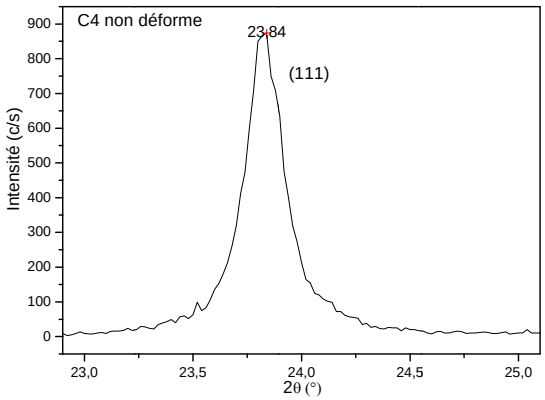

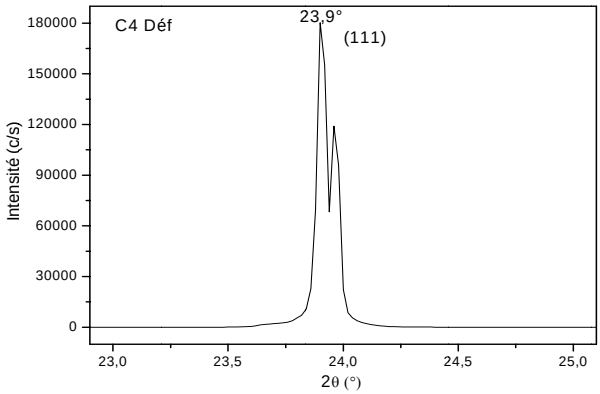

Fig. 6.a XRD spectra of C4 (pure CdTe)

Our work focused on a starting concentration of 4% and the lattice parameter was deduced from XRD spectra (Fig.6.a, b). We notice that after comparison is a small difference probably due to two things:

• The concentration after growth is not the start.
• Growing conditions have allowed us to obtain the empirical variation (tab.4), are not the same used to obtain these materials.

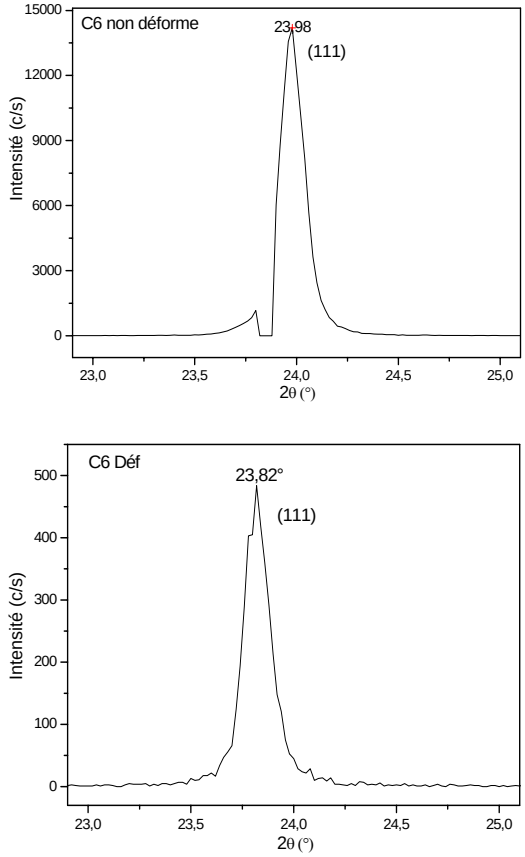

Fig. 6.b XRD spectra of C6 (CdTe with 4% Zn)

Tab.4:

Sample	a_{exp} (Å)	a_{the} (Å)	Δa (Å)
C4 *CdTe*	6.443	6.481	0.038
C6 *CdZnTe*	6.422	6.456	0.034

3. 1. 4. 2 Effect on the density of dislocations:

The explanation of previous results was provided by K. Guergour and colleagues [17], they assign this reduction to cure provided by the introduction of Zn anchor who makes a line break between two atoms of Zn and subsequently prevents the multiplication of these, other hand experience plastic deformation allowed us to give a quantitative estimate of the density of dislocations caused by the deformation.
Table III.2 shows indeed a density of some 108 cm^{-2} for all samples.
Once it is all very interesting to note that the sample as little dislocated, had the case C6 is one that generates a dislocation density larger, about 10 times that seen on C4.
At the moment there is no plausible explanation for this phenomenon, other more specific studies are needed.
But we note nevertheless that the density of dislocations generated in the samples alloyed with Zn is greater than that of pure material.

3.2 Measurement by UV-Visible

The measurement results are illustrated by (Fig.7,8), these measures helped to track the movement of the absorption edge after deformation.

Tab. 5: Energy gap

Sample	E_g(ev)		ΔE_g(ev)
	Not deformed	Deformed	
CdTe	1.476eV	1.448eV	*0.028*
CdZnTe	1.486eV	1.435eV	*0.038*

One interesting observation that can be deducted on the comparison of samples not deformed them, where one can see:
- The displacement of the absorption edge towards higher energies for CdTe alloyed with Zn, which means an increase in energy of the width of the band gap. This is confirmed otherwise [17].

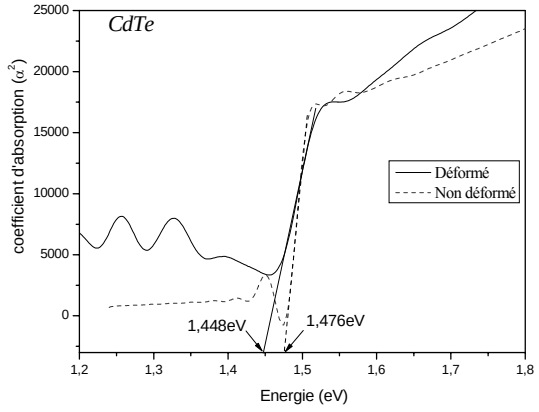

Fig.7 UV-Visible spectra for pure CdTe

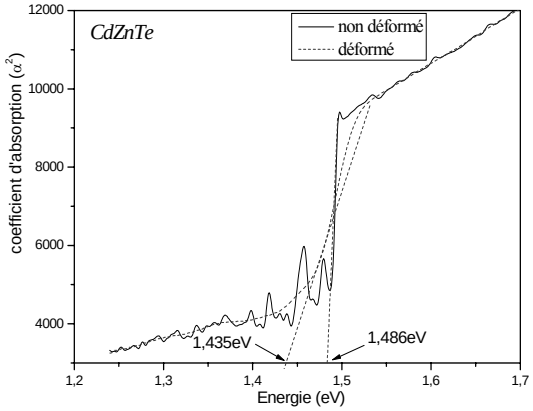

Fig.8 UV-visible spectrum for CdZnTe

- On the deformed state, we notice a decrease in the absorption edge Eg compared to the undeformed state, up to 38 meV.
These results lead us to emphasize that: in general, there was a decrease in energy, given by the absorption edge, due to the creation of level above the top of the valence band, c that is to say that the plastic deformation causes the creation of acceptor centers with their energy close to Ev. In other words the absorption is below the energy-related acceptor center created by plastic deformation.
The narrowing of Eg, as regards CdTe is due by K. Guergour et al [17] to the creation of gaps of Cd neutral after work

photoluminescence on samples deformed by Vickers microindontation.
The same authors attribute the decrease of Eg in the case of CdZnTe, decrease the concentration of Zn atoms attracted to the dislocations created by plastic deformation.

4. Conclusion

CdTe pure and alloyed with some isoelectronic impurities was found in front of more than twenty years as very promising in optoelectronics.
The effectiveness of components based on these materials is strictly related to their quality. It is in this context that our work.
The objective in this study is to see the effect of plastic deformation of crystals of CdTe and CdZnTe, the crystallographic and optical properties.
The investigation methods are X-ray diffraction (XRD) as a means of structural characterization and measurements of UV-Visible spectrophotometry, as a means of optical characterization.
The main results show that:
The best crystal (CdZnTe) before deformation, is the one with the highest dislocation density after deformation and higher optical gap.
The effect of dislocations on the optical properties is characterized by a shift of the absorption edge relative to the undeformed state, due to the creation of acceptor centers, which are the gaps neutral CdTe and Cd decreased concentration of Zn atoms substituting Cd atoms

Reference

[1] R. Triboulet, A. Tromson-Carli, D. Lorans, T. Nguyen Du, J. Electron. Mater. 22 (1993) 827.

[2] C. Braun, H.W. Helberg and A. George, Phil. Mag. (1986)A53

[3] R. Sudharsanan, K.B. Parnham and N.H. Karam, Laser Focus World, 32, N°6 (1996)199.

[4] K. Guergouri, M.S. Ferah., R. Triboulet and Y. Marfaing, Jour. Crystal. Growth, (1994)139.

[5] J.S. Paul, Nucl Instrum Meth Phys Res A. 2003;513:332–9.

[6] K. Zanio, semiconductors and semimetals, R. K. Willqrdson and C. Beer, Academic Press New York (1978).

[7] H. Matsumoto, K. Kuribayashi, Y. Komatsu, A. Nakano, H. Uda, S. Ikegami Jpn J Appl Phys 1983; 22:891.

[8] A. Lachter ; Thèse de Doctorat d'état, Université de Bordeaux I (1980).

[9] T. Güngor, Journal of Research in physics Vol. 27, (1998)9 – 14

[10] T. Gungor and H. Tolunay, Turk. J. Phys, (2002)269-275

[11] S. Abed, thèse de magister, Univ. ... (2005).

[12] S. S. Kim and B. T. Lee, Thin Solid Films 446, (2004)307

[13] J. P. Hirth, J. Lothe, Theory of dislocations, second edition New York (1982).

[14] A. Authier, Colloque rayons X et matière, Monaco, (1973)31

[15] P. Gay, P. B. Hirsch et A. Kelly, Acta Met. 1, (1953)315

[16] J. C. Woolley and B. Ray, J. Phys. Chem. Sol., Pàergamon Press, Vol. 13, (1960)151-153

[17] K. Guergouri, R. Triboulet, A. Tromson-Carli and Y. J.Cryst Growth 86, (1988)61

Journal of New Technology and Materials
JNTM
Vol. 01, N°00 (2011)79-81

OEB Univ. Publish. Co.

Treatment of commercial aluminum by Nd:YAG laser

L. Baziz[a] and A. Nouiri[b]
[a]Department of physics, Univ. of Khenchela (Algeria)
[b]Department of material sciences, Univ. of Oum El-Bouaghi (Algeria)
Emails: leila1_b@yahoo.fr & nouiri.kader@gmail.com
Received: 23 May 2011, accepted: 30 September 2011

Abstract
In this work, two types of commercial aluminum alloys (industrial and recovered aluminum) are studied. The surface is irradiated by Nd: Yag laser (λ = 532 nm, with a pulse duration of 15 ns and an energy of 50 mJ). The experimental results show that the hardness profile can be divided into three regions. The melted area is the hardest region, Then, the hardness decreases sharply in the interface region between the melted area and the heat-affected zone.
Keywords: *Laser treatment, aluminum alloys, Hardness,*

1. Introduction

Even though over 30% of the aluminum produced worldwide now comes from secondary sources (recycled material), the collecting, sorting, and separating of scrap aluminum as well as the processing and upgrading equipment used to convert scrap aluminum and its alloys into new aluminum products and mixtures are studied[1]. The recycled aluminum alloys provides a benchmark in assessing a sustainable vision for positive economic and environmental progress, and it can serve as great reference for educating the next generation of engineers on the demands of sustainable development and the application of life-cycle assessment by industry [2].The Nd:Yag laser radiation is used to improve several material surface hardness, like aluminum, titanium, nickel, cooper and kind of steel (21CrMoV57 and 40C130) targets [3], CdZnTe crystal[4]. The same radiation source is also used to treat some biomaterials[5,6].

In this paper, two comercial aluminum alloys (industrial and recuperated aluminum) are studied. Each alloy contains several chemical elements and it is composed of more than six elements[7]. Although it is a complex material, but we can studied the effect of laser radiation on the surface hardness.

2. Experimental

The samples studied are two materials, industrial and recuperated aluminum alloys. They were polished mechanically and cleaned. The chemical composition of each type is obtained by X-ray analysis[4]. The chemical composition of recycled aluminum alloy is Al(72.02 wt %), Si(13.05 wt %), Zn(6.34 wt %), O(4.28 wt %), Mg(2.08 wt %), Cu(1.75 wt %), and Ni(0.48 wt %). The chemical composition of industrial aluminum alloy is Al(83.10 wt %), Cu(5.47 wt %), Fe(4.12 wt %), O(2.71 wt %), Mn(1.74 wt %), Si(1.66 wt %), and Mg(1.20 wt %)[7]. A nanosecond pulsed laser (Nd:Yag) is used to irradiate an aluminum alloy sample (figure 1). The instrument used in this experiment is the Spectrum laser system. The laser used is a Q-Switch Nd: YAG Brilliant (Quantel). The Bar is pumped by flash lamps, and delivers 300 mJ per pulse at λ = 1064 μ m. The dubbing is often made with a crystal KDP output of the laser, and allows for 160 mJ per pulse at λ = 532 nm. A diachronic mirror, positioned behind the crystal doubler, cannot recover the beam at λ = 532 nm.

The measures of the micro-hardness were taken by a semi-automatic micro-durometer, type ZWICK with Vickers penetration
, under a load of. 100 g and connected to a micro-computer that allows the automatic footprint through an appropriate software.

The properties of material studied are reported in the table 1.

Table1: Main properties of the two alloys studied (compared with pure Aluminum)

	recuperated aluminum	industrial aluminum	pure Aluminum
Density (Kg.m^3)	2816	2614	2700
Microhardness (kg F/mm^2)	118	125	2.75
Thermal conductivity (W/m.K)	128	160	237

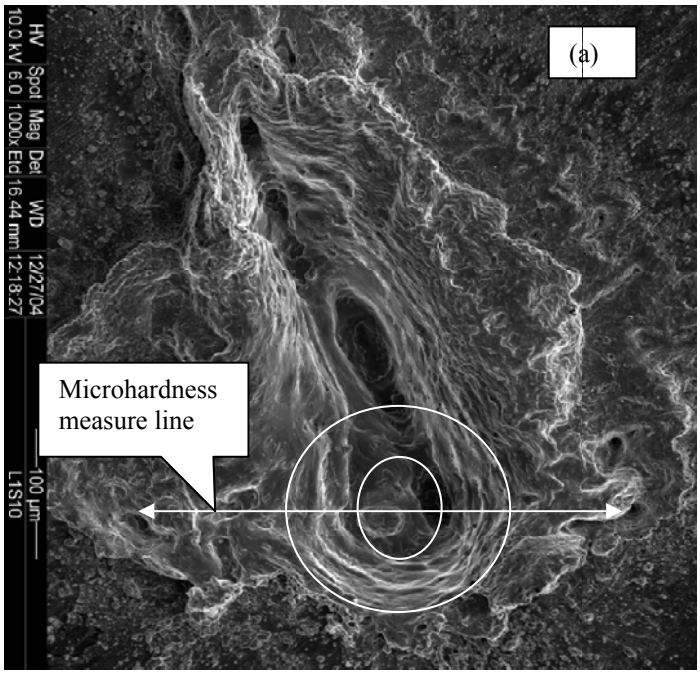

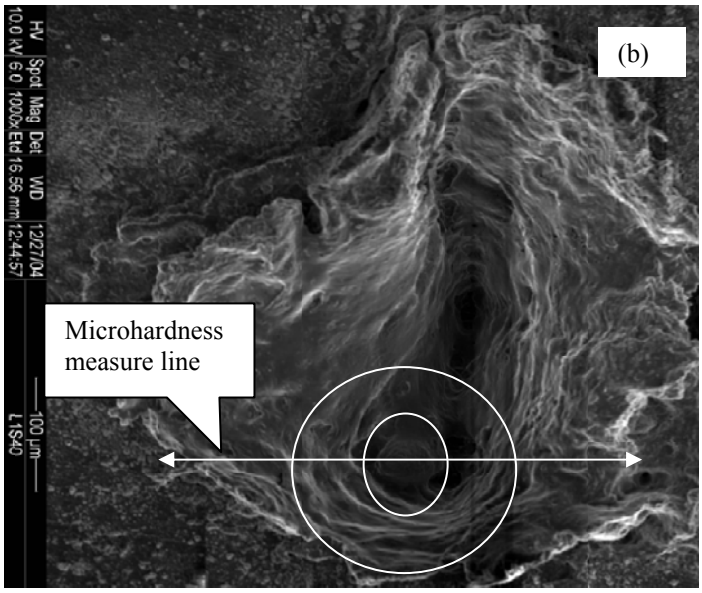

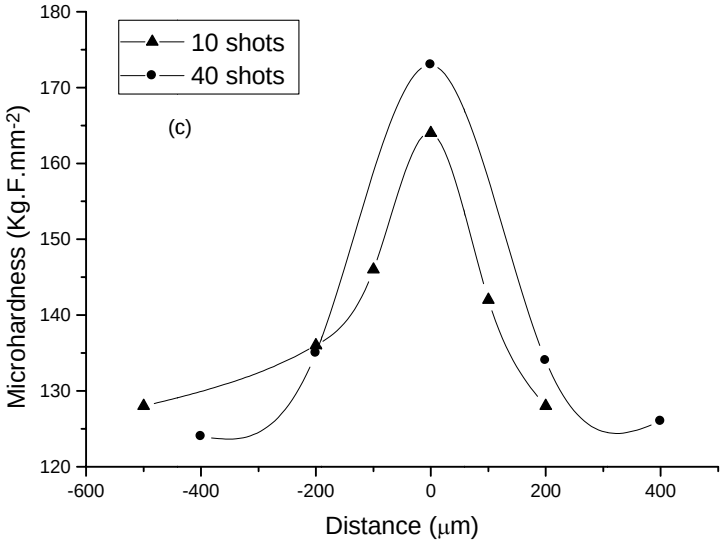

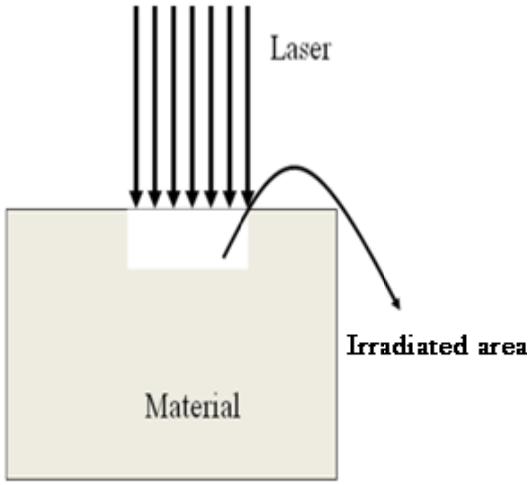

Figure1: Schematic representation of material surface irradiation process.

Figure2 : Dependence of the microhardness on the distance from the center to the boundaries of laser spot.

(a) SEM images of irradiated area with 10 shots of pulsed laser
(b) SEM images of irradiated area with 40 shots of pulsed laser
(c) Curves of the microhardnes as a function of distance for both 10 and 40 shots cases according to the two previous images(a and b)

3. Results and discussion

Figure 2 (a and b) shows a Scanning Electron Microscope images of irradiated area, the line indicates the track of the hardness measures, whereas the circles show the three zones. Figure 2(c) represents the hardness curves depending on the distance along the irradiated zone for both 10 and 40 shots of laser pulses. The hardness profile can be divided into three regions:

1. The melted area is the hardest region because the hardness can reach 164 Kg.F.mm^{-2} (for 10 shots) and 173 Kg.F.mm^{-2} (for 40 shots)
2. Then, the hardness decreases sharply in the interface region between the melted area and the heat-affected zone.
3. The hardness gradually decreases from 152 to 130 Kg F/mm2 in the heat-affected-zone

The hardness remains unchanged in the area unaffected, the value of 125 Kg F.mm^{-2} is the same of that of untreated aluminum (see table 1).

On the other hand, the figure 2(c) shows that the microhardness increases with increasing of number of shots; the curve for 40 shots is above that for 10 shots. These results confirm that obtained by other researchers [3].

4. Conclusion

According to this brief study, the microhardness of aluminum alloys (including the commercial aluminum) depends on the spatial distribution of laser energy whatever the form of laser spot. The microhardness takes a maximum value at the center, and then decreases when one goes to the boundaries.

Acknowledgements

This work is included in project " CNEPRU" under contract number D03020090014, supported by the Algerian High Level Teaching and Scientific Research Ministry MESRS and Oum El-Bouaghi University. The author would like to acknowledge the assistance of Pr Yaser Ahmed Youcef, Chemistry Dpt., Yarmouk University Irbid (Jordan), for his help in laser radiation and Pr Tahar Kerdja, CDTA Algiers, for his help in microhardness measurements and SEM images.

References

[1] Mark E. Schlesinger, O. J. Ilegbusi, Manabu Iguchi, Walter Wahnsiedler, Aluminum recycling, Ed. CRC/Taylor & Francis, 2000

[2] John A. S. Green, Aluminum recycling and processing for energy conservation and sustainability, Ed. ASM International, 2007

[3] C. Oros, J. Optoelectronics and Advanced Materials, 6, 1, (2004) 325 - 328

[4] A. Medvid, A. Mychko, E. Dauksta, Y. Naseka, J. Crocco, E. Dieguez, doi:10.1088/1748-0221/6/11/C11010, Journal of instrumentation(Jinst), (2011)

[5] B. S. Lee , C. P. Lin , F. H. Lin , U. M. Li , W. H. Lan , J Clin Laser Med Surg. 21(1), (2003)41

[6] J. Tavakoli, M. E. Khosroshahi and M. Mahmoodi, IJE Transactions B: Applications, 20, 1, (2007)1-11

[7] L. Baziz, A. Nouiri, and Y. A. Youcef, J. Laser Physics, 16, 12, (2006)1643.